Study of optical and magneto-optical processes in cesium, rubidium and potassium micro- and nano-metric thin atomic layers

Ara Tonoyan

UNIVERSITÉ BOURGOGNE FRANCHE - COMTÉ
Laboratoire Interdisciplinaire Carnot de Bourgogne (ICB) UMR CNRS 6303

NATIONAL ACADEMY OF SCIENCES OF ARMENIA
Institute for Physical Research (IPR)

STUDY OF OPTICAL AND MAGNETO-OPTICAL PROCESSES IN CESIUM, RUBIDIUM AND POTASSIUM MICRO- AND NANO-METRIC THIN ATOMIC LAYERS

by
Ara TONOYAN

A Thesis in Physics
Submitted for the Degree of
Doctor of Philosophy

Date of defense: October 11 2016

Jury

Mr David SARKISYAN	Professor IPR, National Academy of Sciences, Ashtarak, Armenia	*Supervisor*
Mr Claude LEROY	Professor ICB, Université de Bourgogne, Dijon, France	*Supervisor*
Mr Dmitry BUDKER	Professor Johannes Gutenberg University of Mainz, Germany and University of California, Berkeley, USA	*Referee*
Mr Marcis AUZINSH	Professor University of Latvia, Riga, Latvia	*Referee*
Mrs Anahit GOGYAN	Dr. of Physics IPR, National Academy of Sciences, Ashtarak, Armenia	*Examiner*
Mr Hans-Rudolf JAUSLIN	Professor ICB, Université de Bourgogne, Dijon, France	*Examiner*

LABORATOIRE INTERDISCIPLINAIRE CARNOT DE BOURGOGNE-UMR CNRS 6303
UNIVERSITÉ BOURGOGNE FRANCHE - COMTÉ, 9 AVENUE A. SAVARY - 21078 DIJON - FRANCE

INSTITUTE FOR PHYSICAL RESEARCH, NATIONAL ACADEMY OF SCIENCES OF ARMENIA ASHTARAK-2, 0203 ARMENIA

Acknowledgments

I would like to express my sincere gratitude to my supervisors Profs. David Sarkisyan and Claude Leroy for their support and patience during my PhD studies. I acknowledge the support of the French Embassy in Armenia for the grant as Boursier du Gouvernement Français. This grant allowed me to discover the French traditions and to begin the French language learning.

I would also like to thank all the co-workers and the staff of the Institute for Physical Research of National Academy of Sciences of Armenia and the Laboratoire Interdisciplinaire Carnot de Bourgogne of University Bourgogne Franche-Comté for kind and warmhearted attitude, especially to Prof. Aram Papoyan.

I would like to mention particularly Grant Hakhumyan, Rafayel Mirzoyan, Armen Sargsyan, Arevik Amiryan, Mariam Gevorgyan, Maud Louviot, Leo van Damme, David Dzsotjan. Special appreciations to Hovnatan Karapetyan, Anahit Gogyan and Gagik Karapetyan.

Remerciements

J'aimerais exprimer ma sincère gratitude à mes deux directeurs de thèse, les Professeurs David Sarkisyan et Claude Leroy pour leur aide et leur patience pendant mes études de Doctorat. Je remercie l'aide de l'Ambassade de France en Arménie pour mon financement en tant que Boursier du Gouvernement Français. Cette bourse m'a permis de découvrir les traditions françaises et de débuter l'apprentissage de la langue française.

Je voudrais aussi remercier tous mes collègues et toute l'équipe de l'Institute for Physical Research de l'Académie National des Sciences d'Arménie et du Laboratoire Interdisciplinaire Carnot de Bourgogne de l'Université de Bourgogne pour leur attitude chaleureuse et bienveillante, tout particulièrement le Professeur Aram Papoyan. J'aimerais mentionner particulièrement Grant Hakhumyan, Rafayel Mirzoyan, Armen Sargsyan, Arevik Amiryan, Mariam Gevorgyan, Maud Louviot, Leo van Damme, David Dzsotjan. Mes appréciations particulières à Hovnatan Karapetyan, Anahit Gogyan et Gagik Karapetyan.

Research conducted in the scope of the International Associated Laboratory IRMAS (CNRS-France and SCS-Armenia). Part of the results have been received funding from the European Union FP7 IPERA grant N295025, ANSEF Opt-3700 grant.

Contents

Introduction

The relevance of the subject

During the last decades the considerable progress in the development of continuous narrow-band smoothly tunable diode lasers (NBDL) with a spectral width $\gamma_L \sim 1$ MHz reinforced the rapid growth of research in the field of high-resolution spectroscopy in atomic medium. The presence of NBDL in the near infrared region (700 nm - 900 nm) led to the investigations of rubidium (Rb), cesium (Cs) and potassium (K) alkali metals, which have strong atomic transitions in the near infrared region. Narrow-band laser light interaction with atomic vapors of Rb, Cs or K allows investigation of large number of optical and magneto-optical processes, which are widely used in laser technology, high frequency resolution metrology, in the creation of high sensitive magnetometers, quantum communication, optical information recording etc. [14-24]. Therefore, interest in these studies remains very high. It is well known that so-called micro-cells (MC) filled with atomic vapor of alkali metals (with the column thickness $L = 20 - 900$ μm) are common tools for the laser spectroscopy [25-39]. But, recently, it has been demonstrated that with the use of nano-cell (NC - developed at the Institute for Physical Research of the National Academy of Sciences of Armenia) filled with atomic vapor (with the column thickness of $L \sim 20$ nm -3000 nm) it is possible the formation of sub-Doppler resonances in optical domain with a spectral width of $15 - 70$ MHz using NBDL lasers [40-64]. Basically, this is due to the following two processes: 1) formation of narrow, velocity selective optical pumping (VSOP) resonances in the transmission spectra ($D_{1,2}$ lines) of NC, when it is filled with Rb, Cs or K atoms having vapor column thickness $L = \lambda$ (λ-resonant radiation wavelength in the range of

700 to 900 nm). VSOP resonances are located right on the atomic transitions and have spectral width of $15-20$ MHz; 2) formation of narrow absorption lines in the transmission spectra of NC with atomic vapor column thickness of $L=\lambda/2$ (thickness range of $350-450$ nm). The spectral width of these absorption lines is in the range of $60-100$ MHz.

It is also demonstrated that the use of NCs filled with Rb and Cs are very convenient tools to study atom-surface interaction (i.e. van der Waals interaction) [65-76]. The use of VSOP resonances and narrow-band absorption lines allows the high resolution study of the atomic transitions behavior of the hyperfine structures of Rb, Cs and K atoms in moderate external magnetic fields [77-87] and strong magnetic fields (up to 10000 G), including the hyperfine Paschen-Back regime (HPB) [88-96].

Study of the atomic energy levels and transitions behavior in external magnetic fields has been under consideration for a while, as it allows better understanding of the atomic structure and it finds a wide variety of applications. The use of NC and the new techniques of formation of narrow resonances allow further exploration of the atomic transitions of Rb, Cs and K in a much wider range of magnetic field values, than was performed previously, using a compact laboratory device. Similar results can be reached only by means of much more complex techniques of atomic beams if NC is not used. The results of the thesis have wide range of applications.

The aim of the work is experimental and theoretical study of the behavior of individual atomic hyperfine transitions of atoms of Rb, Cs and K (D_1 and D_2 lines) between the Zeeman sublevels in a wide range of external magnetic fields $5-7000$ G using a narrowband continuous laser and NC, as well as the study of the possibility of practical application of the results.

*The **main objectives** of the thesis:*

1. Further refinement of a permanent magnet based device. It is developed to form controllable strong magnetic fields (up to 9 kG). The device has a room for NC and gives a possibility to register transmitted laser radiation.

2. To study the frequency and intensity (i.e. transition probability) behavior of the individual atomic transitions between Zeeman sublevels (optical domain) in external magnetic fields by using NC filled with Rb, Cs or K. Atomic vapor column thicknesses are $L=\lambda$ or $L=\lambda/2$, where λ is the laser wavelength, which is in resonance with the corresponding atomic transition.

3. To develop a numerical software to calculate the frequency and probability of atomic transitions between Zeeman sublevels in strong magnetic fields. Particularly, for D_1 and D_2 lines of ^{39}K, ^{40}K and ^{41}K isotopes.

The ***Scientific novelty***

1. For the first time is experimentally demonstrated that at certain values of the external magnetic fields ($300-2000$ G), there is a huge increase in the probabilities of atomic transitions $F_g = 3 \rightarrow F_e = 5$ of D_2 line for Cs atoms. The probabilities of these transitions (which are forbidden in zero magnetic field) in external magnetic fields increase sharply and exceed the probabilities of allowed atomic transitions.

2. In the cases of circular (σ^+) and linear (π) polarization of laser radiation the D_1 line transitions of ^{39}K atoms have been investigated in external magnetic fields using NC. For the first time it is demonstrated the decoupling of total angular momentum of electrons J and nuclear momentum I (complete hyperfine Paschen-Back regime) in external magnetic field. For ^{39}K the decoupling takes place at $B \gg 165$ G. In the case of linear polarization of laser it is shown that for $B > 400$ G the transmission spectrum consists of 2 groups of transitions and each group contains one so-called "Guiding atomic transition" (GT). The GT indicates the asymptotic value of the probabilities of all transitions in the group and the value of derivatives of frequency shifts (frequency slopes) in magnetic field.

3. Two groups of transitions are detected in the case of circular (σ^+) as well as linear (π) radiation field in the transmission spectrum of Rb (used NC) at $B > 4$ kG. Each group contains 6 ^{85}Rb and 4 ^{87}Rb transitions (thus, total number of transitions 20). The probabilities and frequency slopes in each group tend to certain asymptotic value. This is the expression of the hyperfine Paschen-Back regime.

4. For the first time, it is demonstrated the absence of cross-over resonances in the spectrum of saturated absorption. Micro-cell filled with Rb has been used. The thickness of atomic vapor column was $30-40$ micrometers. The use of micro-cell has allowed the investigation of individual atomic transitions in strong external magnetic fields ($30-6000$ G) utilizing saturated absorption technique.

5. Numerical program based on theoretical model has been developed. The theoretical

curves for ^{39}K are in good agreement with the experimental results.

Practical Importance

1. Giant increase of probabilities of atomic transitions $F_g = 3 \rightarrow F_e = 5$ in external magnetic fields allows registration of absorption and fluorescence lines at new wavelengths of 7 additional atomic transitions.

2. The D_1 lines of all alkali metals contain GTs, which show the asymptotic values of the probabilities and frequency slopes of atomic transitions. Detection of GTs by diagram of atomic transitions is demonstrated.

3. The shift in frequency by $2 - 14$ GHz (relevant to original levels at $B = 0$) of atomic transitions of Rb, Cs and K in strong magnetic fields can be used as a frequency reference. These narrow atomic transitions also may be used to stabilize the laser frequency at the shifted frequencies.

4. The absence of cross-over resonances in saturated absorption spectrum in micro-cells ($30 - 40$ μm) allows the study of Rb, Cs, K, Na and Li atomic transitions in external magnetic fields ($30 - 9000$ G), using saturation absorption.

5. Numerical program based on theoretical model has been developed. The theoretical curves for ^{39}K are in good agreement with the experimental results.

The main statements of the thesis

1. In external magnetic fields ($300 - 3200$ G), there is a huge increase in the probabilities of seven atomic transitions $F_g = 3 \rightarrow F_e = 5$, D_2 line of Cs atoms, which are forbidden by the selection rules in zero magnetic field. The probabilities of two transitions (out of seven) surpass all other transitions' probabilities which initially were allowed.

2. The results of studies of ^{39}K D_1 line transitions in the case of $\sigma+$ and π polarizations in external magnetic fields using nano-cell. At magnetic fields $B \gg 165$ G occurs the complete decoupling of total electronic angular momentum J and nuclear spin I. In the case of linear (π) polarization of laser at $B > 400$ G transmission spectrum consists of two groups of transitions and each group contains guiding atomic transition. The GT of each group shows the asymptotic value of all transitions' probabilities in its group and the frequency slopes in magnetic field.

3. In the case of σ as well as π polarization laser radiations at magnetic fields $B > 4$ kG the

transmission spectrum of Rb D_2 line has two groups of atomic transitions. Each group consists of 6 transitions of ^{85}Rb and 4 transitions of ^{87}Rb. In each group the transition probabilities and frequency slopes tend to a certain asymptotic value.

4. In the saturation absorption spectrum of Rb micro-cell ($30-40$ micrometer) cross-over resonances are absent. This is why it is possible to use micro-cells in the investigations of individual atomic transitions in magnetic fields using saturation absorption technique.

5. Calculated theoretical curves of dependence of individual atomic transitions probabilities and frequency shifts in external magnetic fields. In the range of $0-10000$ G magnetic fields, D_1 and D_2 lines of ^{39}K, ^{40}K and ^{41}K have been examined theoretically.

Approbation of the Thesis Statements

The statements of the thesis were presented and discussed several times at the seminars of the Institute for Physical Research of Armenian NAS in 2014, 2015, 2016; at the Laboratoire Interdisciplinaire Carnot de Bourgogne at the Université Bourgogne Franche-Comté, as well as reported 3 times at the conferences "European Group on Atomic Physics" (EGAS 46, Lille, France, 2014 and EGAS 47, Riga, Latvia, 2015), "Journées de l'école Doctorale Carnot-Pasteur (JED)" (Besançon, France, 2014), "SPECMO" (Dijon, France, 2014), "High Resolution Molecular Spectroscopy (HRMS)", (Dijon, France, 2015), 3 presentations at the "QuantArm" (Yerevan-Tsaghkadzor, Armenia, 2014), twice at the "Laser Physics" (Ashtarak, Armenia, 2013 and Ashtarak, Armenia, 2015), and at the annual seminars for the PhD students in 2014, 2015 and 2016.

The main results of this dissertation have been published as articles in 6 peer reviewed journals and 7 abstracts in the conference Book of Abstracts [1-13].

La pertinence du sujet de thèse - Français

Lors de ces dernières décennies, le progrès considérable dans le développement des diodes laser à bandes étroites continûment accordables (NBDL) avec une largeur spectrale γ_L de l'ordre du MHz a suscité une rapide expansion de la recherche dans le domaine de la spectroscopie à haute résolution dans les milieux atomiques. La possibilité d'utiliser ces diodes dans le

proche infrarouge (700 nm - 900 nm) a permis l'étude des métaux alcalins tels que le rubidium (Rb), le césium (Cs) et le potassium (K), qui ont de fortes transitions atomiques dans le proche infrarouge. L'interaction d'un laser à bande étroite avec des vapeurs atomiques de Rb, Cs et K a permis l'étude d'un grand nombre de processus optiques et magnéto-optiques, qui sont largement utilisés en technologie laser, métrologie de résolution à haute fréquence, dans la création de magnétomètres ultra sensibles, en communication quantique, enregistrement optique d'informations, etc. Par conséquent, l'intérêt de ces études reste fondamental. Il est bien connu que les microcellules (MC) remplies avec de la vapeur atomique de métaux alcalins (d'épaisseur L comprise entre 20 et 900 μm) sont des outils usuels de la spectroscopie laser. Mais récemment, il a été prouvé que l'utilisation d'une nano-cellule (NC - exclusivement fabriquée à l'Institute for Physical Research de l'Académie des Sciences d'Arménie), remplie de vapeur atomique (d'épaisseur $L \sim 20$ nm - 3000 nm) permettait la formation de résonances sub-Doppler dans le domaine optique avec une largeur spectrale de 15 - 70 MHz avec des lasers NBDL. Principalement, ceci est dû à cause des deux processus suivants : 1) formation de résonances étroites appelées "velocity selective optical pumping (VSOP) resonances" dans le spectre de transmission (transitions $D_{1,2}$) de NC, quand elle est remplie avec des vapeurs atomiques de Rb, Cs ou K d'épaisseur $L = \lambda$ (λ est la longueur d'onde de la radiation résonante comprise entre 700 et 900 nm). Les résonances VSOP sont localisées sur les transitions atomiques et ont une largeur spectrale d'environ 15 - 20 MHz ; 2) formation de raies d'absorption étroites dans le spectre de transmission de NC avec une épaisseur de vapeur atomique $L = \lambda/2$ (épaisseur comprise entre 350 et 450 nm). La largeur spectrale de ces raies d'absorption est comprise entre 60 et 100 MHz.

Il a aussi été montré que l'utilisation de NCs, remplies de Rb ou de Cs, sont des outils particulièrement adaptés à l'étude de l'interaction atome-surface (i.e. interaction de van der Waals). L'utilisation de résonances VSOP et de raies d'absorption à bandes étroites permet l'étude à haute résolution du comportement des transitions atomiques des structures hyperfines des atomes de Rb, Cs et K dans des champs magnétiques externes modérés mais aussi dans de forts champs magnétiques (jusqu'à 10000 G), incluant le régime Paschen-Back hyperfin (HPB).

L'étude des niveaux d'énergie atomique et de l'évolution des transitions dans des champs

magnétiques externes a permis une meilleure compréhension de la structure atomique et trouve une large gamme d'applications. L'utilisation de NC et les nouvelles techniques de formation de résonances étroites ont permis une exploration plus approfondie des transitions atomiques du Rb, Cs et K pour une plus large gamme de valeurs du champ magnétique que précédemment grâce à un appareillage de laboratoire plus compact. Sans l'utilisation de NC, ces mêmes résultats sont obtenus seulement si on utilise des techniques beaucoup plus complexes de faisceaux atomiques. Les résultats de la thèse ont une large gamme d'applications.

Le but de ce travail est l'étude expérimentale et théorique du comportement des transitions atomiques hyperfines individuelles des atomes de Rb, Cs et K (raies D_1 et D_2) entre sous niveaux Zeeman pour une large gamme de champs magnétiques externes de 5 à 7000 G en utilisant un laser continu à bande étroite et une NC ainsi que l'étude de la possibilité d'une application pratique des résultats. Les objectifs principaux de la thèse :

1. Amélioration supplémentaire d'un dispositif basé sur un aimant permanent. Ce dispositif est développé afin de générer des champs magnétiques contrôlables (jusqu'à 9 kG). Le dispositif est équipé d'une chambre pour la NC et offre la possibilité d'enregistrer la radiation laser transmise.

2. Etudier la fréquence et l'évolution de l'intensité (i.e. la transition de probabilité) des transitions atomiques individuelles entre sous-niveaux Zeeman (dans le domaine optique) dans des champs magnétiques externes en utilisant une NC remplie de Rb, Cs ou K. L'épaisseur de la vapeur atomique est $L = \lambda$ ou $L = \lambda/2$, où λ est la longueur d'onde laser en résonance avec la transition atomique.

3. Développer un code numérique afin de calculer la fréquence et la probabilité des transitions atomiques entre sous niveaux Zeeman dans des forts champs magnétiques, particulièrement pour les raies D_1 et D_2 des isotopes ^{39}K, ^{40}K et ^{41}K.

La nouveauté scientifique:

1. Pour la première fois, il est montré expérimentalement que pour certaines valeurs du champ magnétique externe (300 - 2000 G), il y a un accroissement important des probabilités des transitions atomiques $F_g = 3 \rightarrow F_e = 5$ de la raie D_2 des atomes de césium. Les probabilités de ces transitions (qui sont interdites en champ magnétique nul) dans un champ magnétique

externe augmentent considérablement et dépassent les probabilités des transitions atomiques autorisées.

2. Les transitions de la raie D_1 des atomes de ^{39}K ont été étudiées en présence de champs magnétiques externes à l'aide d'une NC dans les cas de polarisation circulaire (σ^+) et linéaire (π) de la radiation laser. Pour la première fois, nous avons montré le découplage du moment angulaire électronique total J et du moment nucléaire I (régime Paschen-Back hyperfin complet) en champ magnétique externe. Pour ^{39}K le découplage se produit pour un champ $B \gg 165$ G. Dans le cas d'une polarisation linéaire du laser, on montre que pour un champ $B > 400$ G, le spectre de transmission consiste en 2 groupes de transitions et chaque groupe contient une "Guiding atomic Transition" (GT) ou transition atomique guide. La GT donne la valeur asymptotique des probabilités de toutes les transitions dans le groupe et la valeur des dérivées des décalages en fréquences (pentes des fréquences) en champ magnétique.

3. Deux groupes de transitions sont détectés dans le cas de radiation circulaire (σ^+) ainsi que linéaire (π) dans le spectre de transmission de Rb (à l'aide de NC) pour $B > 4$ kG. Chaque groupe contient 6 transitions ^{85}Rb et 4 transitions ^{87}Rb (donc au total un nombre de 20 transitions). Les probabilités et les pentes des fréquences dans chaque groupe tendent vers une valeur asymptotique. Ceci est l'expression du régime Paschen-Back hyperfin.

4. Pour la première fois, nous avons montré l'absence de résonances cross-over dans le spectre d'absorption saturée. Une microcellule remplie de Rb a été utilisée. L'épaisseur de la vapeur atomique était de $30 - 40$ μm. L'utilisation d'une microcellule a permis l'étude des transitions atomiques individuelles en champ magnétique externe (30 - 6000 G) via la technique d'absorption saturée.

5. Des codes numériques basés sur le modèle théorique ont été développés. Les courbes théoriques pour ^{39}K sont en bon accord avec les résultats expérimentaux.

Importance pratique:

1. L'accroissement gigantesque des probabilités des transitions atomiques $F_g = 3 \rightarrow F_e = 5$ sous champs magnétiques externes a permis l'enregistrement des raies d'absorption et de fluorescence pour de nouvelles longueurs d'onde de 7 transitions atomiques additionnelles.

2. Les raies D_1 de tous les métaux alcalins contiennent des GTs, qui montrent les valeurs

asymptotiques des probabilités et des pentes de fréquences des transitions atomiques. La détection des GTs par un diagramme des transitions atomiques a été démontrée.

3. Le décalage en fréquence de 2 - 14 GHz (par rapport aux niveaux d'origine à $B = 0$ G) des transitions atomiques de Rb, Cs et K en champs magnétiques intenses peut être utilisé comme une fréquence de référence. Ces transitions atomiques étroites peuvent aussi être utilisées pour stabiliser en fréquence le laser aux valeurs des fréquences décalées.

4. L'absence de résonances cross-over dans le spectre d'absorption saturée en microcellules ($30 - 40$ μm) permet l'étude des transitions atomiques de Rb, Cs, K, Na et Li sous champs magnétiques externes (30 - 9000 G).

5. Des codes numériques basés sur le modèle théorique ont été développés. Les courbes théoriques pour ^{39}K sont en bon accord avec les résultats expérimentaux.

Les éléments principaux de la thèse:

1. Sous champs magnétiques extérieurs (300 - 3200 G), on observe un accroissement considérable des probabilités des 7 transitions atomiques $F_g = 3 \rightarrow F_e = 5$, raie D_2 des atomes de césium, qui sont interdites par les règles de sélection sous champ magnétique nul. Les probabilités de deux transitions (sur un total de 7) dépassent toutes les autres probabilités de transitions qui étaient initialement autorisées.

2. Les résultats des études des transitions de la raie D_1 du ^{39}K dans le cas des polarisations σ^+ et π sous champs magnétiques externes en utilisant une nano-cellule. Le découplage complet du moment angulaire électronique total J et du spin nucléaire I apparaît pour des champs magnétiques $B \gg 165$ G. Dans le cas d'une polarisation linéaire (π) du laser, pour $B > 400$ G le spectre de transmission consiste en deux groupes de transitions et chaque groupe contient une GT. La GT de chaque groupe indique la valeur asymptotique de toutes les probabilités de transition dans ce groupe et les pentes en fréquences dans un champ magnétique.

3. Pour des polarisations σ^+ et π de la radiation laser sous champs magnétiques $B > 4$ kG, le spectre de transmission de la raie D_2 du Rb présente deux groupes de transitions atomiques. Chaque groupe consiste en 6 transitions du ^{85}Rb et 4 transitions ^{87}Rb. Dans chaque groupe les probabilités de transition et les pentes en fréquences tendent vers une valeur asymptotique.

4. Les résonances cross-over sont absentes dans le spectre d'absorption saturée du Rb en

microcellule (30 - 40 μm). Il est donc possible d'utiliser des microcellules pour l'étude des transitions atomiques individuelles sous champs magnétiques par la technique d'absorption saturée.

5. Les courbes théoriques calculées de la dépendance avec le champ magnétique des probabilités de transitions atomiques individuelles et des décalages en fréquence. Pour des valeurs de 0 à 10000 G des champs magnétiques appliqués, les transitions D_1 et D_2 du ^{39}K, ^{40}K et ^{41}K ont été observées.

Chapter 1

TECHNICAL DETAILS AND LITERATURE OVERVIEW

1.1 Experimental techniques used in the thesis

1.1.1 Faraday isolator

As diode lasers have large coefficients of light amplification, they are very sensitive to reflections, that produce light directed back into them. In particular, strong reflections appear, when the beam direction is perpendicular to optical surfaces for instance when the beam is perpendicular to the windows of a NC filled with atomic vapour. In the case the NC's sapphire window the reflection is $\sim 7.6\%$, while in the case of NC's garnet window it is $\sim 8.5\%$. The back-reflected beam (feedback) can be the reason of a non-stable operation regime of the diode laser. The utilization of the Faraday Isolator (FI) prevents laser's non-stable operation regime. FI's working principles are: by passing through the first Glan-Taylor polarizer the laser beam becomes linearly polarized. Then, linear laser beam travels through the magneto-active element, which is placed inside a strong permanent magnet. The magnitude of the magnetic field is adjusted so, that after passing through the magneto-active element the plane of polarization is rotated by 45 angular degrees. Afterwards, laser beam passes through the second Glan-Taylor polarizer, which is rotated by 45 angular degrees with respect to the first polarizer, without losses. After the double pass through the magneto-active element, the reflected beam's polarization

plane rotates by 90 angular degrees with respect to the first Glan-Taylor polarizer. As the perpendicularly (with respect to the initial polarization) polarized light can't pass through the first polarizer, there is no light directed back into to the laser and there is no feedback. Thus, the non-stability in laser's operating regime caused by feedback is canceled.

1.1.2 Registration of the signal with the help of photo-detectors

Photo-detector with big aperture and high sensitivity is needed for the registration of the absorption, transmission, fluorescence and saturated absorption signals, which can be relatively weak (few nW) as well as strong (few mW). In our experiments photo-detectors based on FD-24K photodiodes have been utilized. The aperture of the photo-detector is about 1 cm^2 and the sensitivity is in the range of $500 - 1100$ nm. Amplifier based on operational amplifier KR140UD8 has been used. By using digital storage oscilloscope experimental data have been saved. These devices made possible to register relatively weak (~ 10 nW) and relatively strong (~ 2 mW) signals.

1.1.3 Cell temperature measurement

The density of the atomic vapor in the cell is related to the temperature T_{CSA} of the cell's side-arm (CSA). In order to prevent the condensation on the cell's windows, the temperature T_W of the windows must be higher than the temperature T_{CSA} by $15 - 20$ °C. To measure and adjust the temperature of the windows and side-arm of the cell in magnetic fields, a low-sensitive to the magnetic field thermocouple is needed. The use of Chromel-Alumel thermocouples (due to their weak magnetic properties) allowed us to measure and manipulate the temperature without destructing the observation, while studying the magnetic, magneto-optical effects in our experiments. The use of Chromel-Alumel thermocouples provides accurate measurements of the temperatures of up to 1000 °C. Measurement of the voltage on the thermocouples by regular milli-Voltmeter permits to calculate the corresponding temperature. As an example: the signal of 1 mV corresponds to the $T = 24$ °C.

For convenience, all other technical details of the experiment that have been used are described directly in Chapter III and Chapter IV.

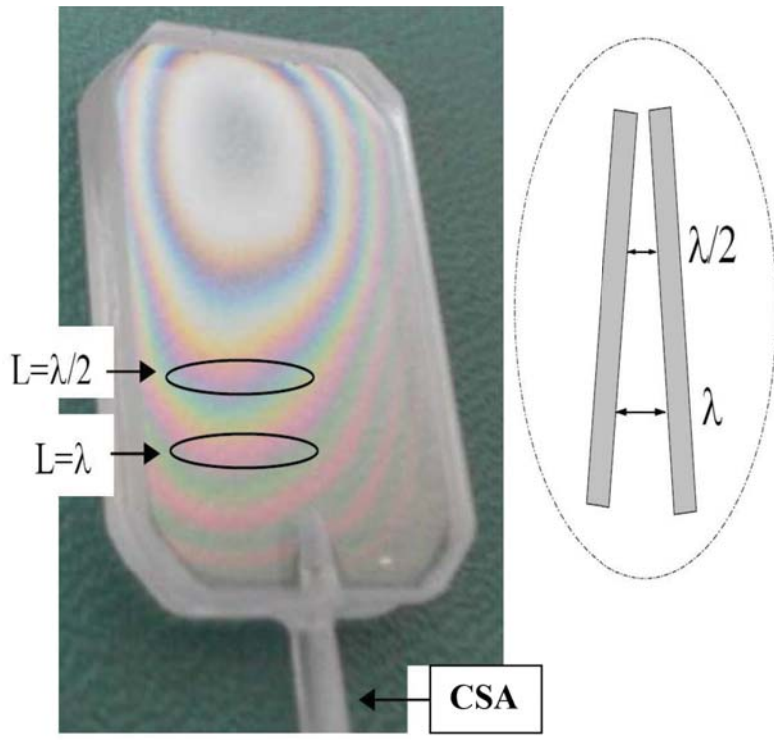

Figure 1.1: Photograph of the nano-cell filled with the Cs metal. The thickness of the wedge-shaped gap is 50 nm $< L <$ 1500 nm. One can see the interference fringes formed owing to reflection of light from the inner surfaces of the cell windows. The regions $L = \lambda/2 = 426$ nm and $L = \lambda = 852$ nm are marked by ovals. The wedge-shaped gap between the inner surfaces of the windows is shown schematically on the right.

1.2 Nano-cells containing atomic vapors of alkali metals

A photograph of nano-cell filled with Cs atomic vapor with a tapered gap of the thickness L ranging from 50 to 1500 nm is shown in Fig. (1.3). The 20 mm $\times$ 30 mm and 2.3 mm-thick windows of the nano-cell were fabricated of well-polished crystalline sapphire (Al_2O_3).The choice of the crystalline sapphire is caused by the fact that this material is very stable to the chemically aggressive hot vapors of alkali metals. Crystalline sapphire is resistant to the temperature of hot vapor of alkali metals up to 1000 °C, while a usual glass or fused-silica is resistant to hot vapors of alkali metals up to 120 °C temperatures.

To minimize natural birefringence of the crystalline sapphire, the c-axis is prepared in a way that it is perpendicular to the surface of the window. The regions with the thickness of $L = \lambda/2 = 426$ nm and $L = \lambda = 852$ nm are marked by ovals in Fig. (1.3). A thin sapphire side-arm filled with metallic Cs is seen at the bottom of Fig. (1.3). In the experiment, the nano-cell is heated to 100 °C, which provides the density of atoms $N \simeq 1.5 \times 10^{12}/\text{cm}^3$ (the

details of the cell design can be found in [40, 72]). Photograph of the nano-cell filled with the Potassium metal is presented in Chapter III.

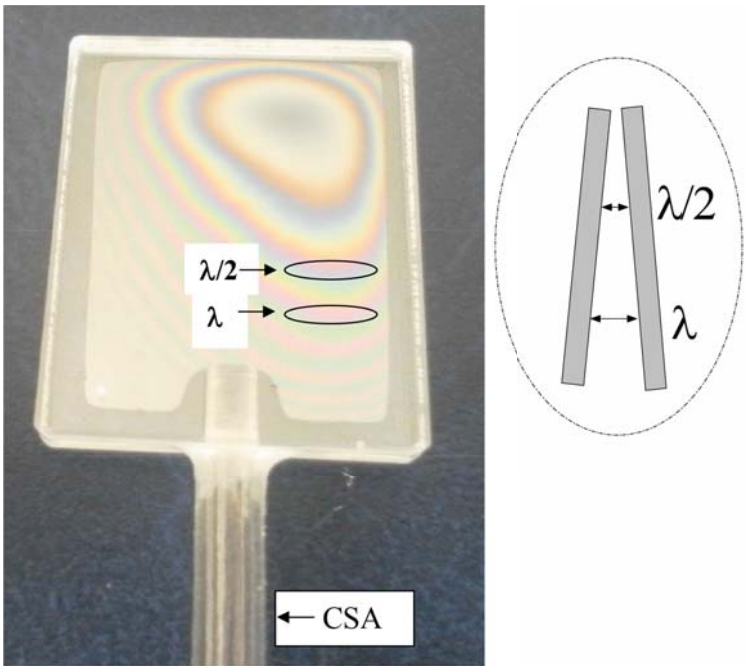

Figure 1.2: Photograph of the nano-cell filled with Rb vapour. The thickness of the wedge-shaped gap is 50 nm $< L <$ 2000 nm. One can see the interference fringes formed owing to reflection of light from the inner surfaces of the cell windows. The regions $L = \lambda/2 = 390$ nm and $L = \lambda = 780$ nm are marked by ovals. The wedge-shaped gap between the inner surfaces of the windows is shown schematically at right.

The cells filled with K, Cs or Rb atomic vapor can operate up to the temperatures of 450 °C and, consequently, provide a density of up to $10^{18}/\text{cm}^3$. Scheme of the nano-cell construction is presented in Fig. (1.5). A hole of 2.5 mm in diameter is drilled previously in the lower part of the sapphire windows of the nano-cell, into which a sapphire tube of the same diameter and 50 mm long, made of commercial sapphire, is inserted. Then, the entire construction was assembled and glued in a vacuum furnace. After the gluing, a glass extension of a few centimeter-long was soldered to the sapphire tube. This glass extension is needed to attach the nano-cell construction to an ordinary glass - vacuum - system. Further, the nano-cell is filled with an alkali metal (Rb, Cs, K, Na, etc.) in a usual way. The amount of the alkali metal is chosen so that the sapphire tube with the inner diameter of about 1 mm is almost completely filled. Since the alkali metal vapor pressure is determined by the upper edge of the alkali metal column in the sapphire tube, the following limiting temperature regime can be implemented if necessary by varying the heater construction: $\sim$ 450 °C at the upper edge,

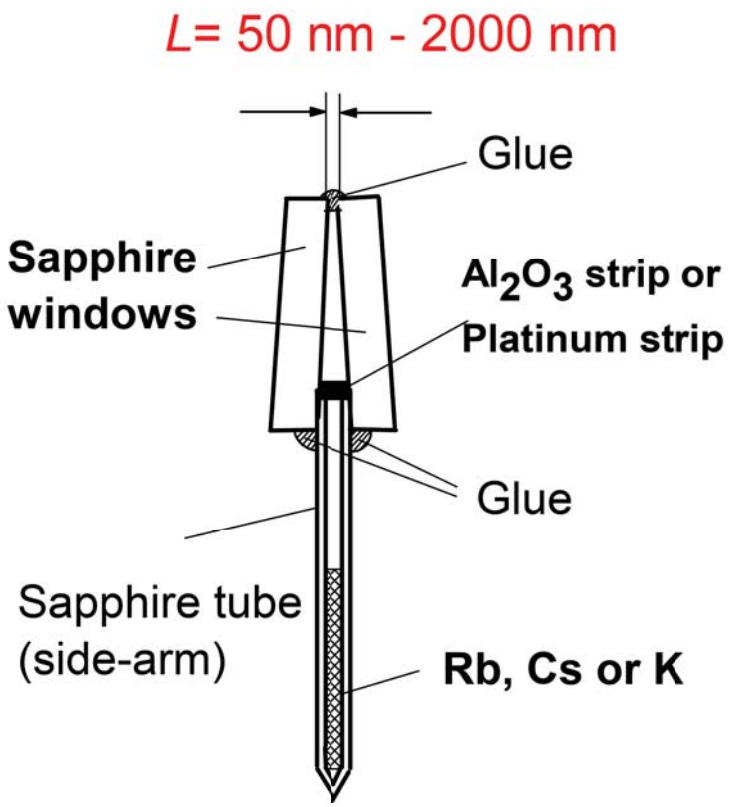

Figure 1.3: The nano-cell construction, the 20×30 mm and 2.3 mm-thick windows of the nano-cell are fabricated of crystalline sapphire. A hole (of 2.5 mm in diameter) is drilled previously in the lower part of windows, into which a sapphire tube of the same diameter and 50 mm long, is inserted. The amount of the alkali metal is chosen so that the sapphire tube is almost completely filled. The alkali metal vapor pressure is determined by the upper edge of the alkali metal column in the sapphire tube.

while the temperature is only ~ 80 °C at the glass extension, because it is off the heater. After the sealing off, the glass tube is about $5 - 6$ mm in length.

The nano-cell furnace is made of nonmagnetic materials and has three holes, two of which are designed to transmit the laser radiation and a side hole is meant for recording fluorescence. The furnace consists of two heaters, the first of which heats the window, and the second one is made to heat the sapphire side-arm containing the alkali metal.

In order to measure the transmission spectra at different nano-cell's thicknesses, the oven with the nano-cell inside is smoothly moved vertically. It is important to note that although it is technically easier to move only the nano-cell, however, in that case the temperature of the nano-cell will be changed during the motion, meanwhile, when the oven with the nano-cell inside is smoothly moved vertically, the temperature remains the same.

1.3 Micro-cells containing atomic vapors of alkali metals

Figure (1.6) shows a photograph of the micro-cell filled with the Rb vapor, with a gap width of $L = 40$ μm between the inner windows of the micro-cell. The gap width is determined by the thin platinum trips placed between the windows before the gluing. The micro-cell has been used in the experiments on saturation absorption presented in Chapter IV. The construction of the micro-cell is similar to that presented for the nano-cells and the difference is that for the gap formation thicker platinum trips are used. A coin of the 2 Euros provides the scale.

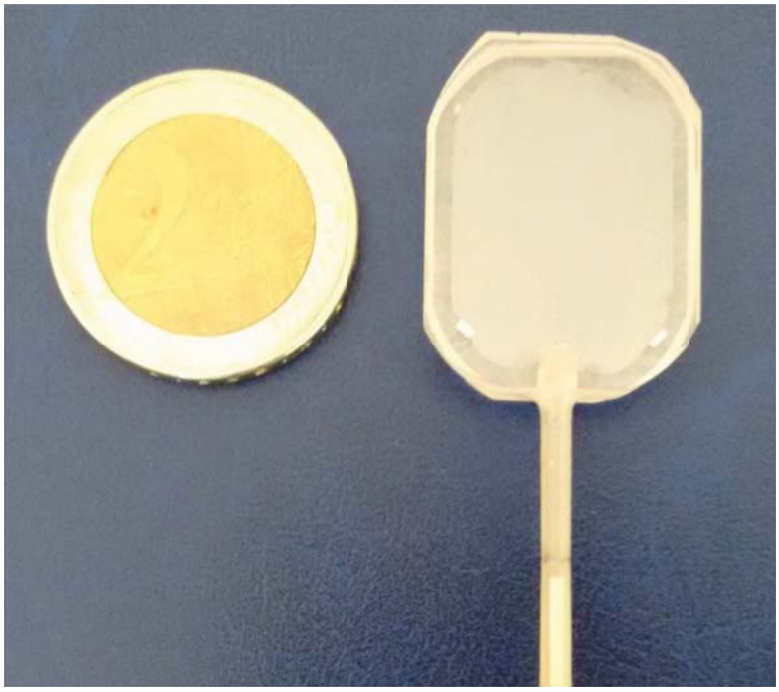

Figure 1.4: Photograph of the micro-cell. For the gap formation thicker platinum trips are used. 2 Euros provides the scale.

1.4 Vapor column thickness identification in a nano-cell

To determine the thickness of the atomic vapor column in a nano-cell, method, based on the interfering property of the light, has been implemented. Perpendicular (to the cells' window) incident light reflects from the wedge form windows. There are three (R_1, R_2 and R_3) reflected beams as seen in Fig. (1.7). R_1 is the reflection from the external surface of the first window. R_2 is the interference of 2 beams, reflected from the internal surfaces of both windows, consequently it carries the information about the thickness of the gap, that is the thickness of the atomic

column. R_3 is the reflection from the external surface of the second window. In the case of ~ 0.1 mm diameter laser beam the windows' internal surfaces are almost perfectly parallel (the deviation is 0.1 mrad). That is why the nano-cell can be examine as a low-finesse Fabry-Perot system [43]. Therefore, the measurement of the ratio of the powers P_{R_2}/P_{R_1} for a certain λ gives a possibility to estimate the value of the thickness L. The relation for the power ratio is

$$\frac{P_{R_2}}{P_{R_1}} = \frac{(1-R)^2}{R} \frac{F \sin^2(\phi/2)}{1 + F \sin^2(\phi/2)}, \tag{1.1}$$

where R is the cell windows reflection coefficient $F = 4R/(1-R)^2$ is the coefficient of finesse and $\phi = 2\pi\delta/\lambda = 2\pi 2L\cos\alpha/\lambda = 4\pi L/\lambda$ (α is practically ~ 0) is the incident angle. As it is seen from relation (1.1) the maximum of the reflection achieved at $\phi/2 = (2k+1)\pi/2$, that is for $L = (2k+1)\lambda/4$ values and the minimum of the reflection (i.e. $P_{R_2}/P_{R_1} = 0$) is at $\phi/2 = \pi k/2$, namely for $L = k\lambda/2$ values, where k is an integer. In case of sapphire windows, with the refraction index of $n(\text{sapphire}) = 1.76$ (for $\lambda = 780$ nm), $R = [(n-1)/(n+1)]^2 = 0.076$ (i.e. 7.6%).

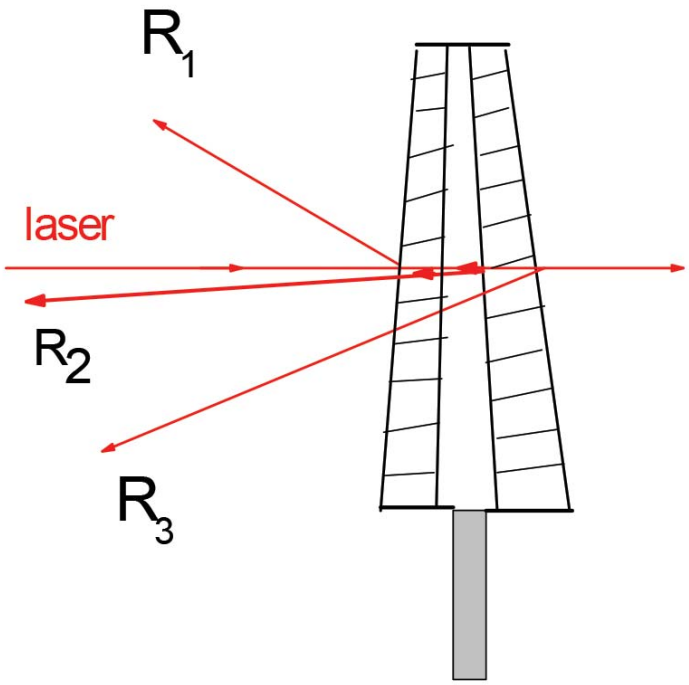

Figure 1.5: The technique based on the use of a laser radiation for the nano-cell thickness measurement. Measuring the ratio P_{R_2}/P_{R_1} and using curves presented in Fig. (1.8) and Fig. (1.9) the nano-cell thickness can be measured.

In Fig. (1.8) the ratio P_{R_2}/P_{R_1} is plotted using formula (1.1) for the laser wavelength $\lambda = 770$ nm. As it is seen the $P_{R_2}/P_{R_1} = 0$ is achieved for $L = \lambda/2 = 385$ nm and $L = \lambda = 770$ nm. Generally the minima of the ratio P_{R_2}/P_{R_1} are at the thicknesses $L = k\lambda/2$, while the maxima of the ratio P_{R_2}/P_{R_1} are at the thicknesses $L = (2k+1)\lambda/4$.

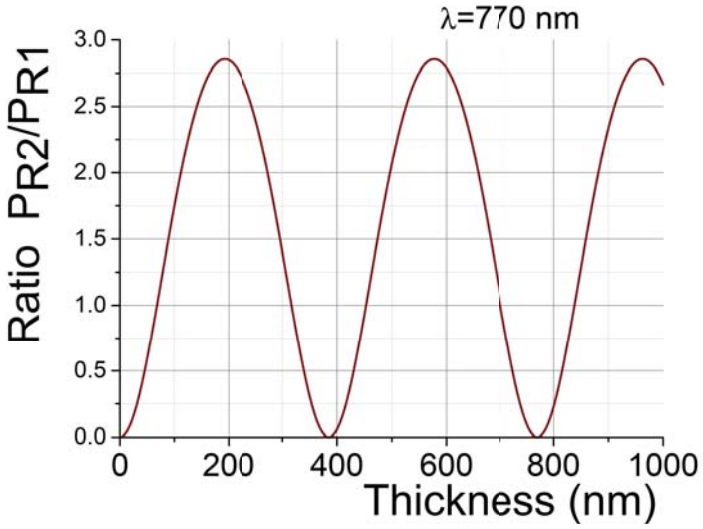

Figure 1.6: The ratio P_{R_2}/P_{R_1} plotted using formula (1.1) for the laser wavelength $\lambda = 770$ nm.

In Fig. (1.9) the ratio of P_{R_2}/P_{R_1} is plotted for the laser wavelength $\lambda = 780$ nm. As it is seen the ratio $P_{R_2}/P_{R_1} = 0$ achieved at $L = \lambda/2 = 390$ nm and $L = \lambda = 780$ nm. For the Cs D_2 line the ratio $P_{R_2}/P_{R_1} = 0$ will be obtained at $L = \lambda/2 = 426$ nm and $L = \lambda = 852$ nm.

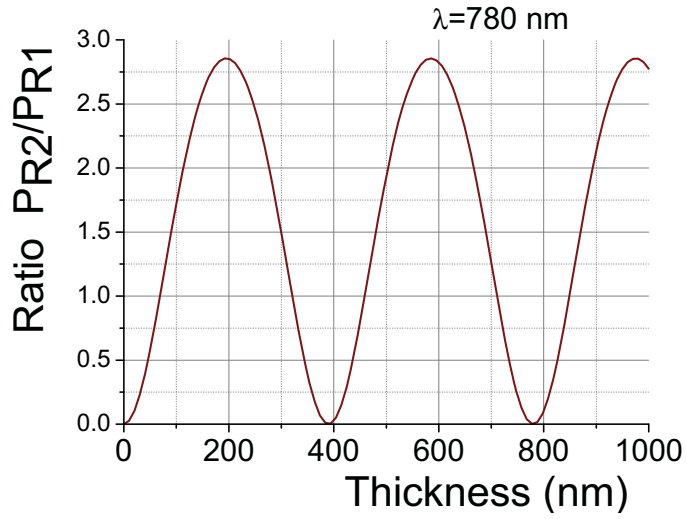

Figure 1.7: The ratio P_{R_2}/P_{R_1} plotted using formula (1.1) for the laser wavelength $\lambda = 780$ nm.

Since the curves presented in Figures (1.8) and (1.9) demonstrate oscillating behavior of the reflection, it is impossible to distinguish between $L = \lambda/2$, $L = \lambda$, $L = 3\lambda/2$, etc. In order to

resolve this problem, we did the following: the nano-cell has been constructed such as that it contains the thickness $L < 100$ nm. Such type of small thicknesses are easy to observe. The reflection from this region vanishes and visually this region has a transparent-white colour. In the case of an "optical contact" (zero thickness) no reflection appears. Hence, by slight motion of the incident light position from the $L < 100$ nm region to the thicker regions, at some point the reflection will be detected. Since for the different wavelengths the maxima and the minima of the reflections are obtained at the different thicknesses, in experimental conditions it is more convenient to make a measurement of the nano-cell thickness directly using diode-laser radiation.

1.5 Methods of forming sub-Doppler optical resonances: review

In an ordinary cell with the thickness in the range of 0.1 mm $-$100 mm, which contains atomic vapours of metals, particularly vapours of alkali metals, it is impossible to resolve individual atomic transitions in absorption (transmission) and fluorescence spectra due to the Doppler-broadening. The explanation is as follows: the width of an individual Doppler broadened atomic transition, having a Gaussian profile, at room temperature ($T = 20$ °C) for different alkali atoms is in the range of $400 - 1000$ MHz. Whereas the frequency interval between the atomic states of the hyperfine structure is of order several tens of MHz - much smaller than the linewidth of the Doppler profile. That's why these atomic transitions are hidden under the overall Doppler broadened profile. In Fig. (1.10) the diagram of the hyperfine structure of D_2 line of ^{85}Rb atoms energy states is presented. As it is seen from the diagram, the frequency distance between the excited atomic states of the hyperfine structure (121 MHz, 63 MHz and 29 MHz) is of order of several tens of MHz, meanwhile the Doppler broadening at room temperature is $\sim$ 500 MHz. Obviously, this leads to the overlapping of the individual transition's profiles in absorption and fluorescence spectra.

At the present time, there are several methods, which allow one to resolve atomic transitions between states of the hyperfine structure. The most used methods are: saturated absorption,

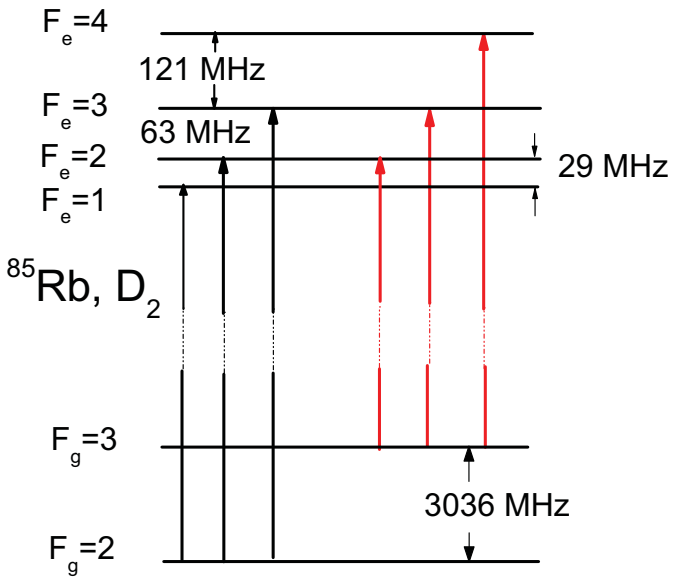

Figure 1.8: The hyperfine energy levels diagram of the D_2 line of the ^{85}Rb. According to the selection rules $\Delta F = 0, \pm 1$ there are two groups of transitions: $F_g = 2 \rightarrow F_e = 1, 2, 3$ and $F_g = 3 \rightarrow F_e = 2, 3, 4$. Only the levels which have been used in the experiments are shown.

selective reflection from the interface of the cell's windows-atomic vapor; the technique of atomic beams; method of electromagnetically induced transparency etc.

• **Method of saturated absorption spectroscopy**

This technique is presented in detail in Chapter IV and here we describe it briefly. For the saturated absorption (SA) technique, the laser beam is split into a weak probe field and a strong pump field, which are sent to the interaction cell as counter-propagating overlapping beams [96-110]. Because of the opposite Doppler shifts, only the atoms moving perpendicularly to the radiation propagation direction resonantly interact with both laser beams. For these atoms, the pump beam saturates the transition (it means that the optical pumping process takes place [111-114]), and the absorption spectrum of the probe shows a Doppler-free dip, the so-called velocity selective optical pumping/saturation (VSOP) resonance located at the line center (see the lower curves in Figures (1.13) and (1.14)). With properly chosen pump and probe beam intensities, careful adjustment of the geometry, and the elimination of stray magnetic fields, the line width of the VSOP resonances may be as narrow as the natural width of the transition. However, as it is mentioned below the disadvantage of the SA technique is the presence of so-called crossover (CO) resonances which can have a large amplitude and make SA spectrum very complicated (see the lower curves in Figures (1.13) and (1.14)).

• **Selective Reflection spectroscopy**

Selective reflection (SR) is a common spectroscopic tool [115-125]. SR can exhibit sub-Doppler features when the reflection of the light is monitored at nearly normal incidence at the interface between a dielectric window and a low-density vapor. Let us note that in order to estimate the value of the reflection coefficient R for SR, the well-known Fresnel formula can be used $R = [(n_W - n_A)/(n_W + n_A)]^2$, where n_W is the refraction index of cell's window (as a rule, a sapphire or a garnet window is used, for which $n_W = 1.76$ (garnet) and 1.82 (sapphire) in case of wavelength 780 nm) and n_A is the refraction index of atoms (Rb, Cs, K, etc.) nearby atomic transition. The value of n_A depends on the density of atomic vapors of a metal, when the frequency of the laser is less than the resonance frequency of the atomic transition $n_A > 1$, and when the frequency of the laser is larger than the resonance frequency of transition $n_A < 1$ [113]. Although with the help of SR it is possible to form narrow resonances of $20 - 30$ MHz line-width, the disadvantages of the SR method is a dispersion-like profile of the SR spectrum and wide spectral wings of the line profile, which are spread over several hundreds of MHz (the reason is that the value of n_A goes down to 1 slowly while the laser frequency detuned far from the resonance [113]). Additionally, a disadvantage of the SR method is the frequency shift of its peaks (by $10 - 15$ MHz) with respect to the frequency of the atomic transition. Also, technically it is not so easy to realize SR technique, because the temperature of the cell must be $120 - 140$ °C, the thermo-resistant material is needed, thus the glass cells are not preferable. Due to the mentioned disadvantages, SR method is rarely used.

• **Technique of electromagnetically induced transparency**

Electromagnetically Induced Transparency (EIT) resonances can occur in a Λ-system with two long-lived ground states and one excited state coupled by two laser fields [14, 15, 20, 21]. The radiations from two independent narrow-band laser beams (the coupling laser with a fixed frequency ν_C and the probe laser with a tunable frequency ν_P) are used to form the EIT-resonance. The difference of frequencies of the two shoulder transitions of the Λ-system should be equal to the difference of frequencies $\nu_P - \nu_C$, which itself equals to the difference of ground states' hyperfine splitting frequencies Δ (for the ^{87}Rb atoms $\Delta = 6835$ MHz). Transition between the ground states is assumed to be forbidden in the first approximation. The frequency

of the coupling beam ν_C is in exact resonance with the corresponding transition and is fixed while the frequency ν_P of the probe radiation is scanned. When the difference of the frequencies $\nu_P - \nu_C$ coincides with the frequency of the hyperfine splitting of the ground states Δ, the transmission spectrum of the probe radiation exhibits a "peak" of increased transmission, also called Dark Resonance (DR) with a spectral line-width that can be less than the natural width (5−6 MHz). Diagram presented in Fig. (1.11) shows three Λ-systems which are formed for ^{87}Rb D_1 line when an external magnetic field is applied. The coupling laser with a fixed frequency ν_C is in resonance with $F_g = 2 \rightarrow F_e = 1$ (excited states $1'$, $2'$ are labeled with primes), while the probe radiation ν_P is scanning thorough $F_g = 1 \rightarrow F_e = 1, 2$ transitions.

The absorption spectrum of the probe radiation, which contains three dark resonances, is shown in Fig. (1.12). The linewidth of the DR is about 3.5 MHz (sub-natural). The frequency interval between the DR is $\Delta_1 = 1.4$ MHz/G $\times$ 40 G = 56 MHz. Thus, with the help of the EIT technique it is possible to form narrow sub-Doppler resonances. A disadvantage of the EIT technique is that two laser radiations with different frequencies are necessary.

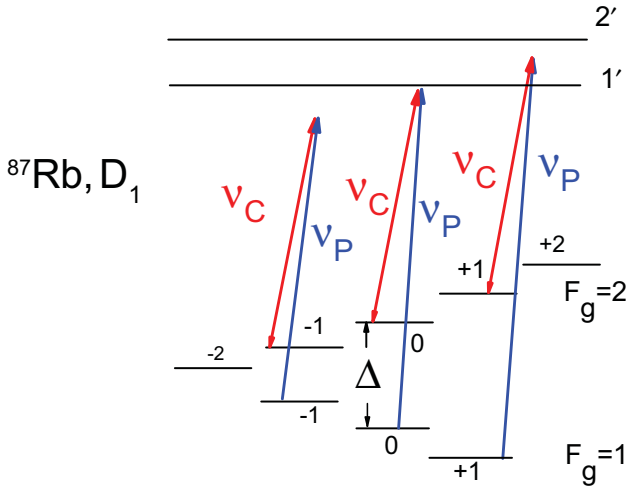

Figure 1.9: Diagram shows three Λ-systems which are formed for ^{87}Rb D_1 line when an external longitudinal magnetic field is applied.

- **Sub-Doppler resonance formation with the nano-cells**

Recently it was demonstrated that using a nano-cell with the thickness $L = \lambda/2$ (where λ is the resonant wavelength of alkali atom transition) it is possible to observe a strong narrowing of the atomic transition which is called Dicke-type narrowing (this occurs at $L = (2n+1)\lambda/2$),

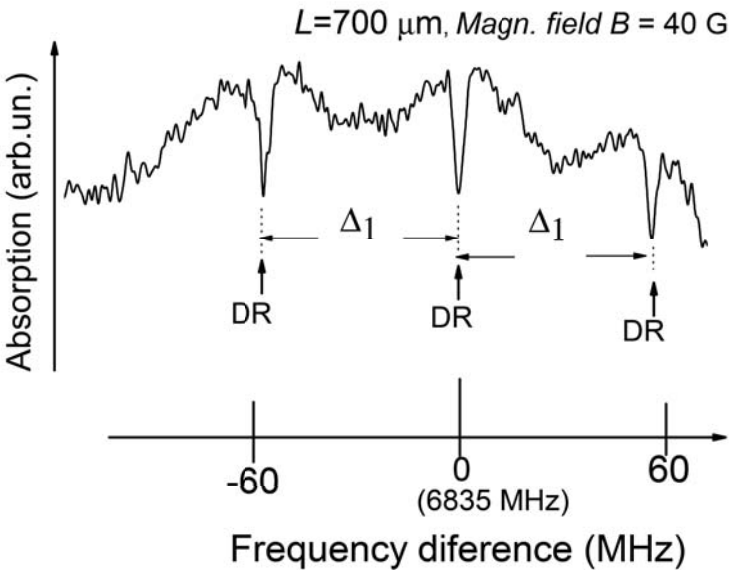

Figure 1.10: Absorption spectrum of the probe radiation which contains three dark resonances. The cell thickness is 0.7 mm, the temperature is $80°C$, the coupling and probe laser powers are 0.5 mW and 0.5 mW, respectively. Magnetic field is $B = 40$ G.

where $n = 0, 1, 2, 3, ...$) [43, 44, 64]. Meanwhile, for the thickness $L = \lambda$ there is broadening of the atomic transition, nearly, up to Doppler line-width which is called collapse of Dicke-type narrowing (this occurs at $L = (2n)\lambda/2$) [43, 44, 64]. Figure (1.13) shows the transmission spectrum of the nano-cell with the thickness of $L = \lambda/2 = 390$ nm (the upper curve) for the ^{85}Rb, D_2 line, atomic transitions $F_g = 3 \rightarrow F_e = 2, 3, 4$ (see Fig. (1.10)). Laser power is 3 μW. As it is seen due to the sub-Doppler narrowing all three atomic transitions are well resolved. The middle curve shows transmission spectrum of the nano-cell with the thickness $L = \lambda$. As it is seen there is broadening of the atomic transitions (that's why they are not resolved). The lower curve shows the SA spectrum, which is used as a reference spectrum.

Figure (1.14) shows the transmission spectrum of the nano-cell with the thickness $L =$ 390 nm (the upper curve) for the ^{85}Rb, D_2 line, transitions $Fg = 3 \rightarrow F_e = 2, 3, 4$. Laser power is 2 mW. As it is seen there is power broadening of the transition's line-width. The middle curve shows transmission spectrum of the nano-cell with the thickness $L = \lambda$. As it is seen there are VSOP resonances that are located at the atomic transitions. The lower curve shows the SA spectrum.

With properly chosen laser intensity, careful adjustment of the geometry (the incident laser radiation must be perpendicular to the nano-cell windows), the linewidth of the VSOP reso-

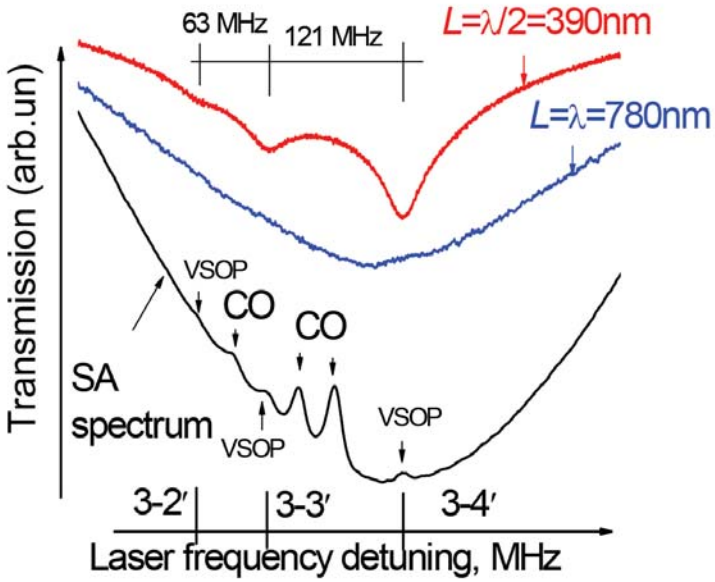

Figure 1.11: The upper curve is the transmission spectrum of the nano-cell with $L = \lambda/2 = 390$ nm for ^{85}Rb, D_2 line, $F_g = 3 \to F_e = 2, 3, 4$. Laser power is 3 μW. With properly chosen laser intensity, careful adjustment of the geometry (the incident laser radiation must be perpendicular to the nano-cell windows), the line-width of the atomic transition could be (at full width at half maximum (FWHM)) of about $100 - 120$ MHz. The middle curve shows transmission spectrum of the nano-cell with the thickness $L = \lambda$. The lower curve is the SA spectrum.

nances could be of about $10 - 15$ MHz.

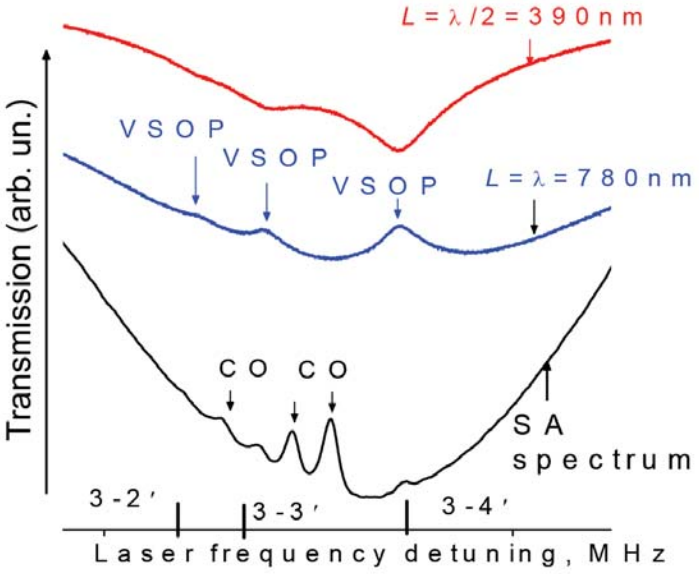

Figure 1.12: The upper curve is the transmission spectrum of the nano-cell with $L = 390$ nm for ^{85}Rb, D_2 line, $F_g = 3 \to F_e = 2, 3, 4$. Laser power is 2 mW. The middle curve is the transmission spectrum of the nano-cell with the thickness $L = \lambda$, which contains VSOP resonances. The lower curve is the SA spectrum.

These remarkable properties of the nano-cell with the thickness of $L = \lambda/2$ (the narrowing of the atomic transition's linewidths) and with thickness $L = \lambda$ (narrow VSOPs resonance) have

been used in Chapter III to study separately a large number of atomic transitions which occur when a strong magnetic field is applied. Some additional details concerning the spectroscopy with the nano-cell is presented in Chapter III as well.

1.6 Study of alkali atoms in strong magnetic fields: review

The splitting of atomic levels in weak magnetic fields is described by the total angular momentum $F = J + I$ of the atom and its projection m_F, where $J = L + S$ is the total angular momentum of electrons and I is the nuclear spin.

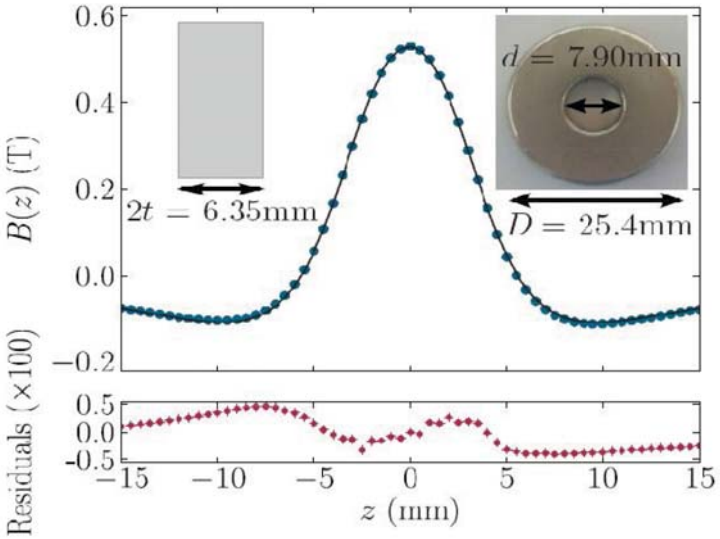

Figure 1.13: Dimensions of a permanent neodymium magnet and axial variation of the z-component of magnetic field. The z-axis offset, z_0, length, $2t$, inner diameter, d, and outer diameter, D, describe the dimensions of the magnet, and the remanence, Br, characterizes the strength of the material. The measured solid (blue) circles are achieved by use of a Hall probe along the z-axis, and the black line is theory. Below the main graph is a plot of the residuals (solid red circles), that show excellent agreement between theory and experiment.

In the case of alkali atomic vapors, a sub-Doppler resolution is needed to study separately each individual atomic transition between hyperfine Zeeman sublevels of the ground and excited states (in the case of a natural mixture of ^{85}Rb and ^{87}Rb the number of closely located atomic transitions can reach several tens). To eliminate the Doppler broadening, the Saturation Absorption spectroscopy in the weak/intermediate magnetic fields (up to < 100 G) was implemented in studies of atomic transitions [126, 128]. However, the obtained spectra were

rather complicated, primarily due to the presence of strong cross-over resonances, which also split into many components. Thus, SA spectroscopy in ordinary vapor cells is practical only for $B < 100$ G. In order to demonstrate a destructive influence of the cross-over resonance in the saturation absorption spectrum in external magnetic field, see the spectra shown in Fig. 4.5 that have been used for calibration of the magnetic field [128].

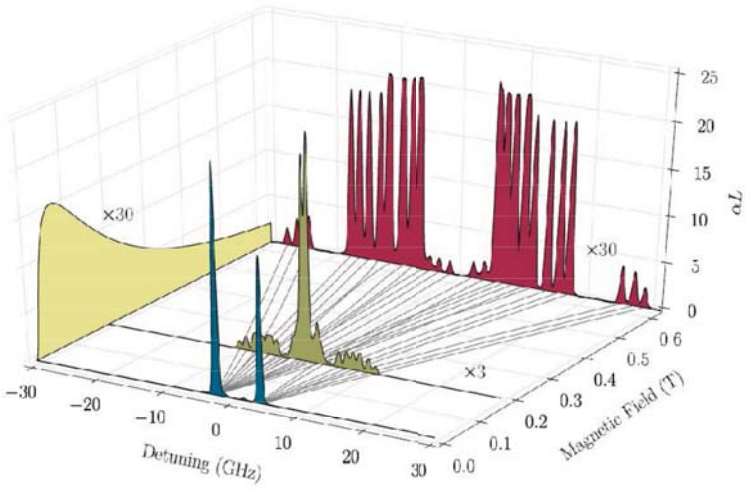

Figure 1.14: Experimentally measured absolute optical depths for the ^{87}Rb D_2 line, through a 1 mm-long cell, at three different magnetic field values. The solid (blue) measured spectrum was taken in the absence of magnetic field. The solid (olive) measured spectrum was taken at a field of 0.180 T in the intermediate regime. The solid (red) measured spectrum was taken at a field of 0.618 T in the hyperfine Paschen-Back regime. The solid (grey) theoretical lines show the transition frequencies as a function of magnetic field. Also plotted is the solid (yellow) theoretical transition strength of the outermost weak transitions as a function of magnetic field. The normalization factors ($\times 3$ and $\times 30$) compensate for a decrease in the transition strengths. See Fig. (4) in [130].

We would like to present and discuss a few papers recently published by researchers from Durham University (UK) [129 - 135]. In their experiment they use a compact 1 mm^3 micro-fabricated vapor cell that makes easy to maintain a uniform and large magnetic field with a small and inexpensive permanent magnet. They have used 1 mm-long glass cell filled with isotopically pure ^{87}Rb vapour. Small size of the 1 mm-long glass cell allows them to insert the cell into the hole of the strong permanent magnet. This place is labeled by the symbol $\leftrightarrow$ in the right upper corner of Fig. (1.15) [130]. The longitudinal magnetic field inside the 1 mm-long glass cell is homogeneous and reaches 6 kG. The cell was heated up to 116 °C. The transmission spectra are presented in Fig. (1.16) and were measured using a single calibrated photodiode. Linear polarized laser radiation has been used. In the longitudinal magnetic field the linear

polarization could be considered as circular- (left hand) σ^+ and σ^- (right hand) polarized radiations. The spectrum of the σ^+ polarized radiations is presented in the high frequency region and consists of eight large absorption peaks and a few small peaks of the ^{87}Rb, D_2 line. In Chapter III in Fig. (3.29) the absorption spectrum of Rb nano-cell with $L = \lambda/2$ for magnetic field $B = 6850$ G and σ^+ laser excitation is presented. For such a strong magnetic field, J and I momenta become decoupled and the splitting of the atomic levels is described by the projections m_J and m_I (see Fig. (3.27)) and the hyperfine Paschen-Back regime is realized (for details see Chapter III). Since the spectra are obtained nearly under the same experimental conditions let's compare them. First of all the absorption linewidth of the atomic transition is Doppler-broadened and achieves ~ 600 MHz (Fig. (1.16)), while the absorption linewidth of the atomic transition in our case is < 200 MHz (with a proper adjustment it could be of ~ 120 MHz). Since in our case the nano-cell was filled with the natural Rb (72% ^{85}Rb and 28% ^{87}Rb), in Fig. (3.29) twenty (twelve atomic transitions belong to the ^{85}Rb and eight atomic transitions belongs to the ^{87}Rb) well resolved atomic transitions are presented. As the average frequency interval between the atomic transitions of ^{85}Rb and ^{87}Rb $B \sim 6$ kG is less than 500 MHz, in the work [130] they are obliged to use only isotopically pure ^{87}Rb vapour. Note, that even if the authors of the work [130] use only isotopically pure ^{85}Rb vapour they still can't succeed to get frequency resolved twelve atomic transitions of the ^{85}Rb atoms. Also, as it is shown in Fig. (3.31) and Fig. (3.32) the eight atomic transitions of ^{87}Rb presented in Fig. (1.16) are contained in two separate groups (four atomic transitions in each group). These two groups have different frequency slopes and amplitudes. As it is demonstrated in Fig. (3.32), the amplitudes of four transitions on the high frequency wing shown in Fig. (1.16) are more than 2 times smaller than the amplitudes of the four neighboring transitions. Thus, the Fig. (1.16) represents not the real amplitudes of the ^{87}Rb transitions, while in the Fig. (3.29) the absorption spectrum of Rb nano-cell ($L = \lambda/2$) precisely represents the real amplitudes of the ^{87}Rb transitions.

To conclude, the most preferable method (of course depending on the application) to study the behavior of the atomic states in an external magnetic fields is the technique based on a nano-cell (see Chapter III).

1.7 Summary

1. We have indicated the experimental technique used in the experimental setup and described the block-scheme, construction and technical characteristics of the continuous wave smoothly tunable external cavity diode laser. In our experiments ECDLs operate at wavelengths $\lambda = 770$ nm, 780 nm, 794 nm and 852 nm. Also, the other used equipment is described.

2. The construction of the nano-cells containing vapours of alkali metals with the thicknesses of L varying in range 50 nm -2000 nm is described.

3. The construction of a micro-cell containing vapour of an alkali metal with the thickness of $L \sim 30 - 40$ μm is described.

4. A technique based on the use of a laser radiation is presented for the nano-cell thickness measurement.

5. A critical review of different techniques of the sub-Doppler spectroscopy: a) Saturated absorption; b) Selective reflection; c) Technique of electromagnetically induced transparency is given. We analyzed the advantages and the disadvantages of these techniques in comparison with the one based on the nano-cell use. We demonstrated the advantages of the sub-Doppler spectroscopy based on the usage of a nano-cell.

6. A critical review of different techniques that have been implemented to study the behavior of alkali atoms in strong magnetic fields is presented. It is demonstrated that at the present time the most preferable method to study an atomic behavior in strong magnetic field is the method based on the nano-cell use (see also Chapter III).

Chapter 2

THEORETICAL BACKGROUND FOR THE CALCULATION OF ALKALI SPECTRA IN THE PRESENCE OF STRONG MAGNETIC FIELDS

To verify and predict the experimental data we have applied and adapted the theory and numerically calculated the transition shifts, intensities and spectra of the alkali atoms in the presence of external magnetic field. The developed model is valid for the wide range of magnetic field intensities.

2.1 Theoretical background

In the absence of external magnetic field the atomic level hyperfine structure is split into $2F+1$ sublevels, where the angular momentum $\vec{F}$ is defined as

$$\vec{F} = \vec{J} + \vec{I}, \tag{2.1}$$

where $\vec{J} = \vec{L} + \vec{S}$ is the total angular momentum, $\vec{L}$ is the orbital angular momentum, $\vec{S}$ is the electronic spin momentum and $\vec{I}$ is the nuclear spin momentum. The external magnetic field removes the degeneracy and shifts the energy levels. The mixing of atomic states appear, resulting in atomic transition frequency and probability changes. These effects should be taken into account while considering the absorption profiles of atomic lines for different laser polarizations. Here we present the theoretical background and numerically calculated results and in the next chapters we show the experimental studies performed for external magnetic fields reaching up to 10000 Gauss, when alkali vapour is confined in sub-micron thin vapour cell.

The Hamiltonian of an atom in an external static magnetic field B can be expressed as a sum of unperturbed H_0 and interaction H_B Hamiltonians

$$H = H_0 + H_B. \tag{2.2}$$

If the magnetic field B is directed along the quantization axis z, then H_B can be represented as

$$H_B = -\frac{\mu_B B}{\hbar}(g_L L + g_S S + g_I I) = -\frac{\mu_B B_z}{\hbar}(g_L L_z + g_S S_z + g_I I_z), \tag{2.3}$$

where μ_B is the Bohr magneton ($\mu_B = 1.399624$ MHz/G), g_L is the orbital Landé factor, g_S is the spin Landé factor and g_I is the nuclear Landé factor [141, 142].

The value of g_S is obtained experimentally and according to precise measurements its value is 2.0023193043622(15). The value for g_L is given by

$$g_L = 1 - \frac{m_e}{m_{nuc}}, \tag{2.4}$$

where m_e is the electron mass and m_{nuc} is the nuclear mass [141, 142], taking into account that $\frac{m_e}{m_{nuc}} \ll 1$, we can approximate $g_L \sim 1$. In order to obtain the theoretical value of g_I one has to take into account the complex structure of nucleus. Up to date g_I's value is only measured experimentally, no theoretical calculation is available [14].

Applied external magnetic field not only shifts the atomic levels and removes the degeneracy, but also modifies the transition oscillation strength. The transition intensity is proportional

to the square of latter. Atomic states mixing leads to strong nonlinear dependence of the transition intensities on external magnetic field which is observed experimentally and calculated numerically. For the calculation we have used the formulas presented in [24, 136 - 142].

When the sub-level energy shift caused by the magnetic field is smaller than the hyperfine splitting, F is a good quantum number. In this case H_B can be rewritten as

$$H_B = -\frac{\mu_B B_z}{\hbar} g_F F_z, \tag{2.5}$$

where the hyperfine Landé g_F-factor is given by

$$\begin{aligned} g_F = g_J \frac{F(F+1) - I(I+1) + J(J+1)}{2F(F+1)} + g_I \frac{F(F+1) + I(I+1) - J(J+1)}{2F(F+1)} \\ \simeq g_J \frac{F(F+1) - I(I+1) + J(J+1)}{2F(F+1)}. \end{aligned} \tag{2.6}$$

In this approximate expression the nuclear term is neglected as $g_I \ll g_J$.

For **weak magnetic** fields interaction Hamiltonian H_B perturbs the zero-field eigenstates of hyperfine Hamiltonian ($B \ll A_{hfs}/\mu_B$). To the lowest order, the levels split linearly [141, 142].

$$\Delta E_{|F,m_F\rangle} = \mu_B g_F m_F B_z. \tag{2.7}$$

Splitting in this regime is called anomalous Zeeman effect.

When the sub-level energy shift caused by the magnetic field is smaller than the fine splitting and larger than the hyperfine splitting, J is a good quantum number. In this case H_B can be rewritten as

$$H_B = -\frac{\mu_B B_z}{\hbar} (g_J J_z + g_I I_z), \tag{2.8}$$

where the hyperfine Landé g_J-factor is given by

$$\begin{aligned} g_J = g_L \frac{J(J+1) - S(S+1) + L(L+1)}{2J(J+1)} + g_S \frac{J(J+1) + S(S+1) - L(L+1)}{2J(J+1)} \\ \simeq 1 + \frac{J(J+1) + S(S+1) - L(L+1)}{2J(J+1)}. \end{aligned} \tag{2.9}$$

The approximation is due to the use of approximate values for $g_L \simeq 1$ and $g_S \simeq 2$.

In contrast to the **weak magnetic** fields, for **strong magnetic** fields the interaction term is greater than the hyperfine Hamiltonian, therefore the hyperfine Hamiltonian perturbs $|Jm_J Im_I\rangle$ strong-field eigenstates. In this case the energies are given to the lowest order by

$$E_{|Jm_J Im_I\rangle} \simeq A_{hfs} m_J m_I + B_{hfs} \frac{9(m_I m_J)^2 - 3J(J+1)m_I^2 - 3I(I+1)m_J^2 + I(I+1)J(J+1)}{4J(2J-1)I(2I-1)} + \mu_B(g_J m_J + g_I m_I)B_z \tag{2.10}$$

Splitting in this regime is called Paschen-Back effect.

In general, for **intermediate magnetic** fields it is necessary to diagonalize the Hamiltonian matrix numerically in order to obtain the energy shifts.

2.2 Model of interaction Hamiltonian for any magnetic field

If the external magnetic field B is along the quantization axis z, the interaction Hamiltonian is given by

$$H_B = -\frac{\mu_B B}{\hbar}(g_L L + g_S S + g_I I). \tag{2.11}$$

To evaluate the matrix elements of the Hamiltonian (2.11), we use the basis of the unperturbed atomic state vectors $|n, L, J, F, m_F\rangle \equiv |F, m_F\rangle$ and the $\Delta L = 0, \Delta J = 0, \Delta F = \pm 1, \Delta m_F = 0$ selection rules. In this representation the matrix elements can be written as

$$\begin{aligned}\left\langle F, m_F | H_B | \tilde{F}, m_{\tilde{F}} \right\rangle = \left\langle IJF, m_F | H_B | I\tilde{J}\tilde{F}, m_{\tilde{F}} \right\rangle = \\ (\mu_B B)\delta(J, \tilde{J})\delta(m_F, m_{\tilde{F}}) g_J (-1)^{I+J+m_{\tilde{F}}+1} \sqrt{J(J+1)} \times \\ \sqrt{(2J+1)}\sqrt{2F+1}\sqrt{2\tilde{F}+1} \begin{pmatrix} F & 1 & \tilde{F} \\ -m_F & 0 & m_{\tilde{F}} \end{pmatrix} \begin{Bmatrix} J & 1 & \tilde{J} \\ \tilde{F} & I & F \end{Bmatrix},\end{aligned} \tag{2.12}$$

where the parenthesis and curly brackets denote the $3j$ and $6j$-symbols, respectively.

To obtain the matrix elements of (2.12) numerical calculations are needed. To ease the

computational task we present the $3j$ and $6j$-symbols in a more convenient way. In this basis, the diagonal matrix elements are given by

$$\langle F, m_F|H_B|F, m_F\rangle = E_0(F) + \mu_B g_F m_F B, \tag{2.13}$$

where $E_0\,(F)$ is the initial energy of the sub-level $|F, m_F\rangle$ and g_F is the effective Landé factor [141, 142].

According to the $\Delta L = 0, \Delta J = 0, \Delta F = \pm 1, \Delta m_F = 0$ selection rules, the non-zero off-diagonal matrix elements are

$$\begin{aligned}\langle F-1, m_F|H|F, m_F\rangle = \langle F, m_F|H|F-1, m_F\rangle = -\frac{\mu_B B}{2}(g_J - g_I)\times \\ \left(\frac{[(J+I+1)^2 - F^2][F^2 - (J-I)^2]}{F}\right)^{1/2}\left(\frac{F^2 - m_F^2}{F(2F+1)(2F-1)}\right)^{1/2}.\end{aligned} \tag{2.14}$$

The Hamiltonian is a block diagonal matrix consisting of blocks corresponding to a given value of m_F. In terms of the unperturbed state vectors the new state vectors (eigenvectors) can be represented as

$$|\Psi(F_e, m_e)\rangle = \sum_{F'_e} \alpha^e_{F_e F'_e}(B, m_e)|F'_e, m_e\rangle \tag{2.15}$$

and

$$|\Psi(F_g, m_g)\rangle = \sum_{F'_g} \alpha^g_{F_g F'_g}(B, m_g)|F'_g, m_g\rangle. \tag{2.16}$$

As the perturbation induced by the magnetic field couples only the states which satisfy $\Delta m_F = 0$ selection rule, the summations are done only on state vectors having the same m_F. The state vectors $|F'_e, m_e\rangle$ and $\left|F'_g, m_g\right\rangle$ are the unperturbed state vectors of the excited and the ground states, respectively. The coefficients $\alpha^e_{F_e F'_e}(B, m_e)$ and $\alpha^g_{F_g F'_g}(B, m_g)$ are mixing coefficients of the excited and the ground states, respectively. These coefficients depend on the field strength and magnetic quantum numbers m_g or m_e. The diagonalization of the Hamiltonian of the considered system allows us to get the mixing coefficients.

In the case of low radiation intensities (smaller than saturation intensity) the transition intensity is proportional to the spontaneous emission rate of the associated transition A_{eg}, that

is to the square of the modified dipole momentum. Therefore, the intensity can be given by

$$W_{eg} \propto A_{eg} \propto \left(\left\langle \Psi(F_e, m_e)|r_q^1|\Psi(F_g, m_g)\right\rangle\right)^2, \tag{2.17}$$

where the $\left\langle \Psi(F_e, m_e)|r_q^1|\Psi(F_g, m_g)\right\rangle$ represents the matrix element that couples the two hyperfine sublevels $|\Psi(F_e, m_e)\rangle$ and $|\Psi(F_g, m_g)\rangle$ (e refers to the excited states and g refers to the ground states). Considering expressions (2.15) and (2.16) for the state vectors, dipole momentum (all α coefficients are real) can be evaluated by

$$\left\langle \Psi(F_e, m_e)|r_q^1|\Psi(F_g, m_g)\right\rangle = \sum_{F_e' F_g'} \alpha^e_{F_e F_e'}(B) \left\langle F_e', m_e|r_q^1|F_g', m_g\right\rangle \alpha^g_{F_g F_g'}(B), \tag{2.18}$$

where the primed quantum numbers refer to the unperturbed states and the unprimed quantum numbers refer to the new states. We can rewrite these matrix elements as a product of a Clebsch-Gordan coefficient and a reduced matrix element, using the Wigner-Eckart theorem. By implementing this theorem we can factor out the angular dependence of the matrix element

$$\left\langle F_e, m_e|r_q^1|F_g, m_g\right\rangle = \langle F_g\ m_g, 1\ q|F_e, m_e\rangle \left\langle F_e||r||F_g\right\rangle. \tag{2.19}$$

Here, q ($q = -1, 0, +1$) is an index labeling the component of r in the spherical basis. The doubled bars point out that the matrix element is reduced. We can also write (2.19) in terms of a Wigner $3j$ symbol as:

$$\left\langle F_e, m_e|r_q^1|F_g, m_g\right\rangle = (-1)^{F_g - m_e}\sqrt{(2F_e+1)} \begin{pmatrix} F_g & 1 & F_e \\ m_g & q & -m_e \end{pmatrix} \left\langle F_e||r||F_g\right\rangle. \tag{2.20}$$

The $3j$ symbol (or, equivalently, the Clebsch-Gordan coefficient) vanishes unless the sublevels satisfy $m_e = m_g + q$. The reduced matrix element of rhs of (2.20) can be further simplified by factoring out the F_e and F_g dependences into a Wigner $6j$ symbol, leaving a further reduced

matrix element that depends only on the L, S, and J quantum numbers

$$\begin{aligned}\langle F_e||r||F_g\rangle = \quad & \langle J_e\ I, F_e||r||J_g\ I, F_g\rangle = \\ & (-1)^{F_e+J_e+I+1}\sqrt{(2F_g+1)(2J_e+1)}\left\{\begin{array}{ccc} F_e & 1 & F_g \\ J_g & I & J_e \end{array}\right\}\langle J_e||r||J_g\rangle\,.\end{aligned} \tag{2.21}$$

As is shown above, the calculation of the transition intensity is equivalent to the calculation of the transfer coefficients

$$W_{eg} \propto A_{eg} \propto a^2\left[\Psi(F_e, m_e); \Psi(F_g, m_g); q\right], \tag{2.22}$$

where a is the transfer coefficients. The transfer coefficients are expressed as

$$a\left[\Psi(F_e, m_e); \Psi(F_g, m_g); q\right] = \sum_{F_e' F_g'} \alpha^e_{F_e F_e'}(B) a\left(\Psi(F_e, m_e); \Psi(F_g, m_g); q\right) \alpha^g_{F_g F_g'}(B), \tag{2.23}$$

where the unperturbed transfer coefficients are given by

$$\begin{aligned} & a\left(\Psi(F_e, m_e); \Psi(F_g, m_g); q\right) = (-1)^{1+I+J_e+F_e+F_g-m_e} \\ & \times\sqrt{2J_e+1}\sqrt{2F_e+1}\sqrt{2F_g+1}\left(\begin{array}{ccc} F_e & 1 & F_g \\ -m_e & q & m_g \end{array}\right)\left\{\begin{array}{ccc} F_e & 1 & F_g \\ J_g & I & J_e \end{array}\right\}, \end{aligned} \tag{2.24}$$

Formulas (2.1 − 2.24) have been used to calculate the frequency shifts and modification of intensities for the corresponding transitions.

Thus, using the above-mentioned equations, we can calculate spectra of alkali atoms for any magnetic field. Below we present the obtained results for different types of atoms.

2.3 Potassium: numerical data

Natural potassium consists of three isotopes ^{41}K, ^{40}K, ^{39}K. However, up to date there is no sufficient theoretical data on these isotopes, and no transition probabilities for ^{41}K and ^{40}K as they are of low densities in nature (6.3% and 0.01%, respectively). In this section we present for the first time theoretical studies of the ^{39}K and ^{41}K isotope D_1 and D_2 lines in the presence

of external magnetic field while interacting with σ^+, σ^- and π polarized laser fields.

As we have mentioned above, external magnetic field, while directed along the quantization axis, couples only with the states which satisfy the $\Delta L = 0, \Delta J = 0, \Delta F = \pm 1, \Delta m_F = 0$ selection rules. Therefore, not only mixed atomic states appear, but also there are certain states that are not mixed - they are so-called pure states. In an external magnetic field pure states experience only linear energy shifts, thus the transition intensity and slope (derivative of the transition shift) are constant exceptionally between these states. We have observed for the first time these transitions experimentally and explained theoretically. We name this transition guiding transition (GT). The name comes from the fact that in high magnetic fields (HPB regime) all transitions are regrouped and if in the group a GT exists, all other transitions intensities and slopes asymptotically tend to this GT intensity and slope. So, by knowing only the GT intensity and slope one can predict the behavior of the other transitions in the group in a very large range of magnetic fields (up to 200 kG). The upper limitation is due to the fine structure, since in high enough magnetic fields, decoupling of the quantum numbers L and S occurs meaning that quantum number J is no longer a good quantum number. The magnetic field strength, when this happens, is connected with the fine structure constant α and it is $\sim$ 200 kG for potassium vapours. This value depends on specific atoms and isotopes.

$m_F \rightarrow$	-2	-1	0	$+1$	$+2$
$S_{1/2}$ states					
$F = 2$	**P**	**M**	**M**	**M**	**P**
$F = 1$		**M**	**M**	**M**	
$P_{1/2}$ states					
$F = 2$	**P**	**M**	**M**	**M**	**P**
$F = 1$		**M**	**M**	**M**	

$m_F \rightarrow$	-3	-2	-1	0	$+1$	$+2$	$+3$
$P_{3/2}$ states							
$F = 3$	**P**	**M**	**M**	**M**	**M**	**M**	**P**
$F = 2$		**M**	**M**	**M**	**M**	**M**	
$F = 1$			**M**	**M**	**M**		
$F = 0$				**M**			

Table 1. Atomic states, P stands for pure states, M stands for mixed states.

For different polarizations of radiation and for different D lines GTs are different. For D_1 line and π polarized radiation GTs are: $F = 2, m_F = -2 \rightarrow F' = 2, m_{F'} = -2$ and $F = 2, m_F = +2 \rightarrow F' = 2, m_{F'} = +2$. For D_1 line and circularly polarized radiation as well as for D_2 line and π polarized radiation GT does not exist. In comparison to D_1 line, in case of D_2 line for σ^+ and for σ^- polarized radiations only one GT exists: $F = 2, m_F = +2 \rightarrow F' = 3, m_{F'} = +3$

and $F = 2, m_F = -2 \rightarrow F' = 3, m_{F'} = -3$, respectively.

2.3.1 Numerical data for ^{39}K

Below, in Figures 2.1 - 2.12 we present our numerical data for the ^{39}K isotopes in detail. We present the transition shifts dependence on magnetic field and corresponding transition intensities. Below each figure a table with corresponding notations of the labels and its transition diagram is presented. 3-dimensional spectra are presented as well. Though calculations are made for magnetic fields up to 10 kG, only up to 800 G data are shown, as after 800 G there are no peculiarities in them. The behaviour change appears around 200 kG (see above text).

We show data for ^{39}K isotope D_1, D_2 lines, σ^+, σ^-, π transitions.

2.3.2 Numerical data for ^{41}K

The data for ^{41}K are structured in the same way as for ^{39}K and are shown in Figures 2.13 - 2.24. As one can conclude, the difference between these two isotopes is only quantitative. The HPB regime starts at lower magnetic fields for ^{41}K due to the A_{hfs} constant.

In 3D graphs in both cases for ^{39}K and ^{41}K isotopes, components arising from the vanishing of the degeneracy of $F_g = 1$ and $F_g = 2$ states are in red and blue, respectively.

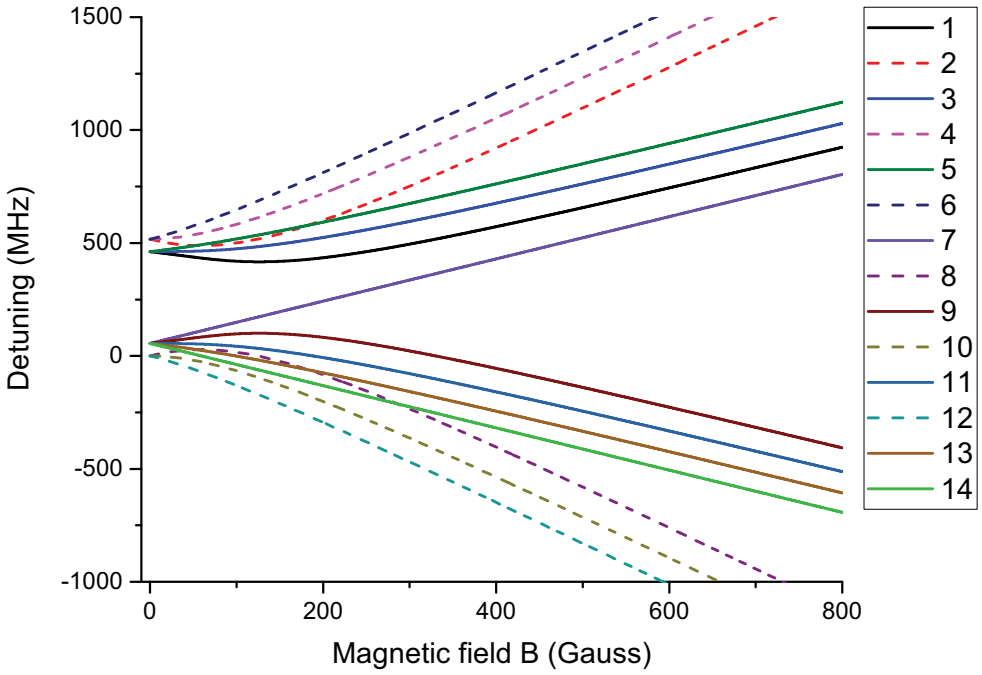

(a) Frequency shift dependence on magnetic field.

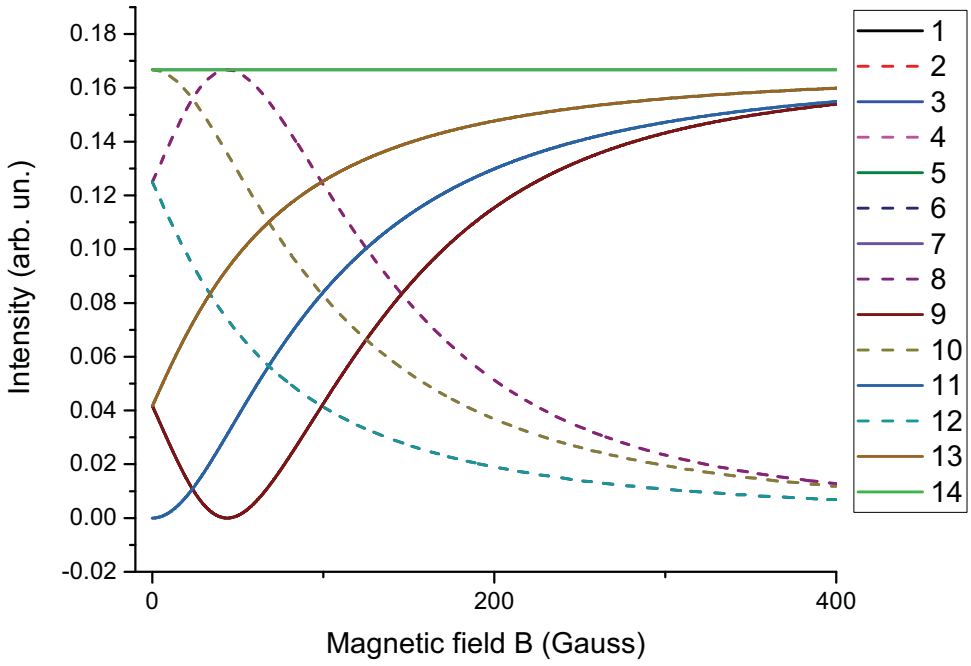

(b) The transitions intensity versus magnetic field.

Figure 2.1: The calculated frequency shift and intensity modification for ^{39}K transitions D_1 line for π polarized exciting radiation. The zero is $F_g = 2 \rightarrow F_e = 1$.

D1 line (|J=1/2> → |J'=1/2>), labels for π transitiors. |F=1, m_F> → |F', m_F'=m_F>

	m_F=-2	m_F=-1	m_F=0	m_F=1	m_F=2
F'=2		2	4	6	
F'=1		1	3	5	

D1 line (|J=1/2> → |J'=1/2>), labels for π transitiors. |F=2, m_F> → |F', m_F'=m_F>

	m_F=-2	m_F=-1	m_F=0	m_F=1	m_F=2
F'=2	7	9	11	13	14
F'=1		8	10	12	

(a) Table 2. The transitions labels in F m_F basis.

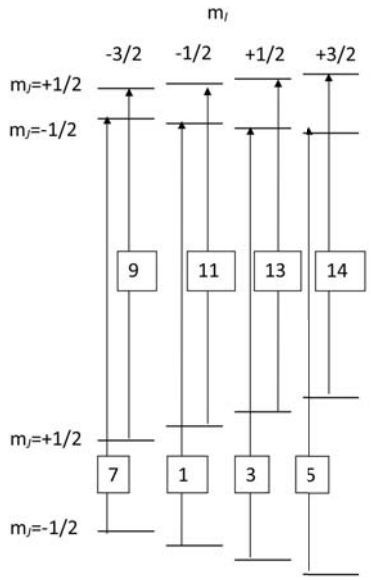

(b) Diagram 1. The transitions labels in m_I m_J basis.

The transitions labels for ^{39}K D_1 line for π polarized exciting radiation in different basis. The labels correspond to the labels on figure.

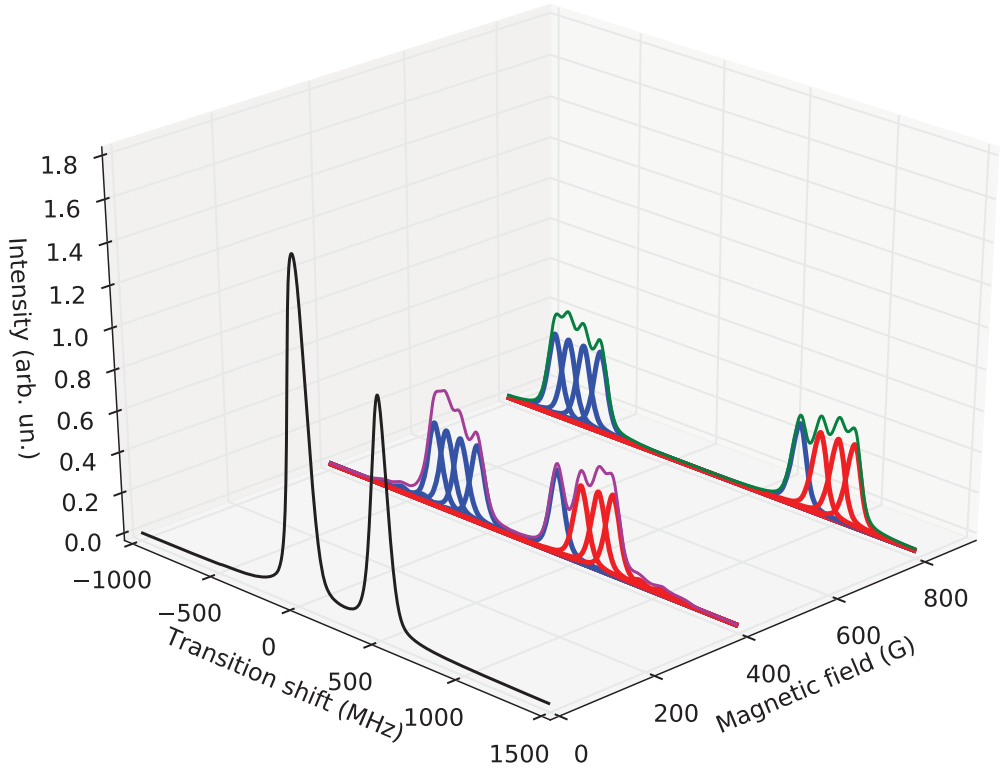

Figure 2.2: ^{39}K 3D spectra of D_1 line for π polarized exciting radiation at 0 G, 400 G and 800 G magnetic fields. The zero is $F_g = 2 \rightarrow F_e = 1$.

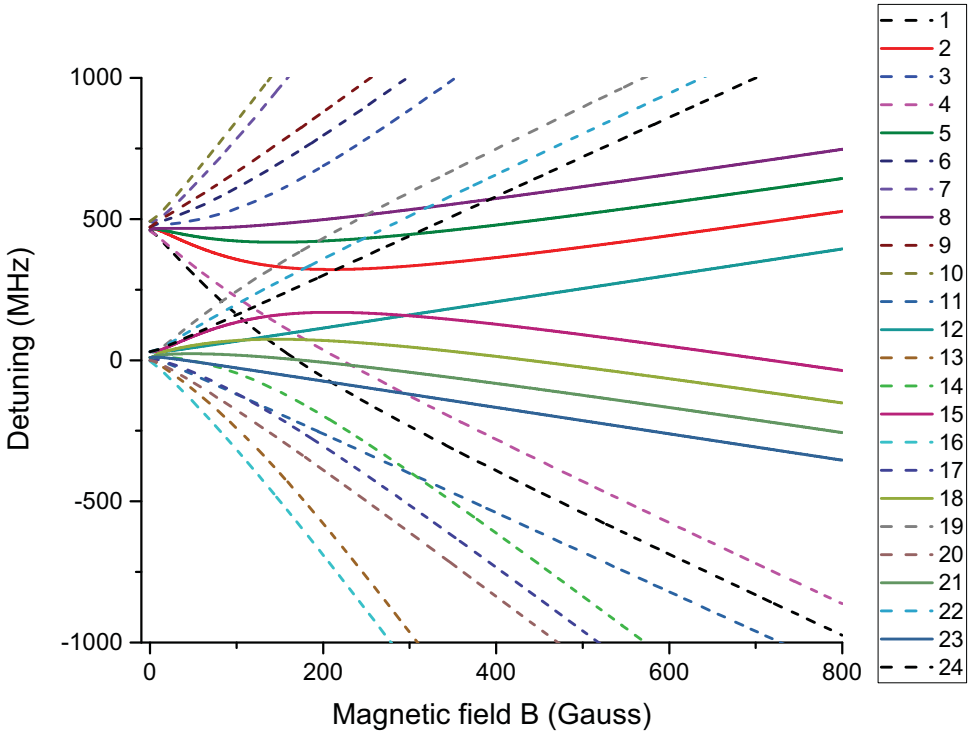

(a) Frequency shift dependence on magnetic field.

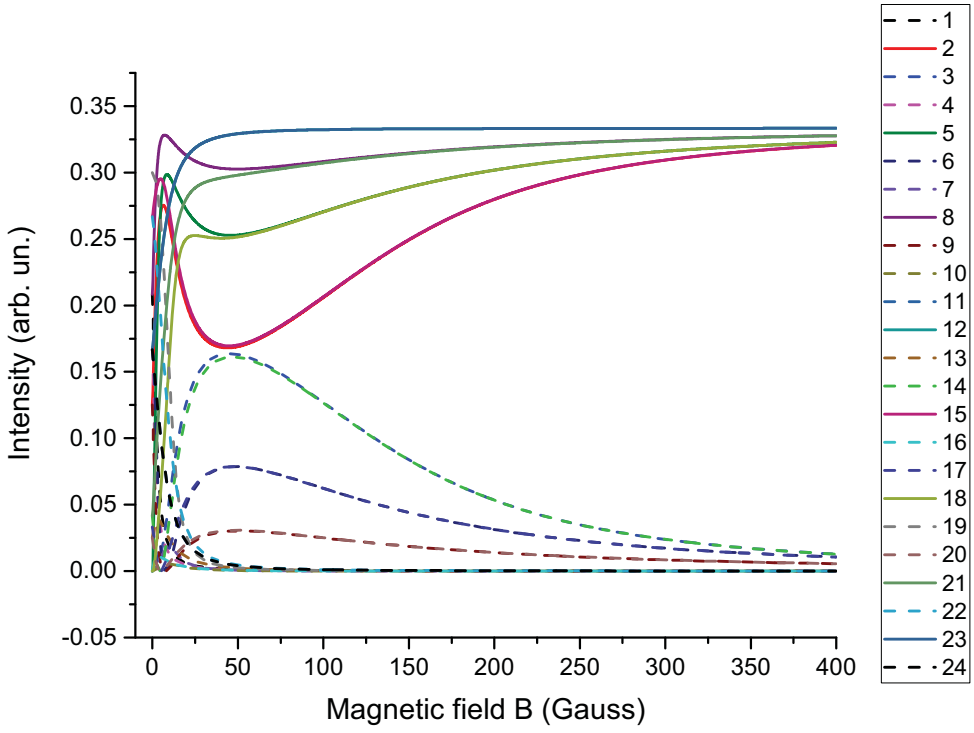

(b) The transitions intensity versus magnetic field.

Figure 2.3: The calculated frequency shift and intensity modification for ^{39}K transitions D_2 line for π polarized exciting radiation. The zero is $F_g = 2 \rightarrow F_e = 1$.

D2 line (|J=1/2> → |J'=3/2>), labels for π transitions. |F=1, m_F> → |F', m_F'=m_F>

	m_F=-3	m_F=-2	m_F=-1	m_F=0	m_F=1	m_F=2	m_F=3
F'=3			3	7	10		
F'=2			2	6	9		
F'=1			1	5	8		
F'=0				4			

D2 line (|J=1/2> → |J'=3/2>), labels for π transitions. |F=2, m_F> → |F', m_F'=m_F>

	m_F=-3	m_F=-2	m_F=-1	m_F=0	m_F=1	m_F=2	m_F=3
F'=3		12	15	19	22	24	
F'=2		11	14	18	21	23	
F'=1			13	17	20		
F'=0				16			

(a) Table 3. The transitions labels in F m_F basis.

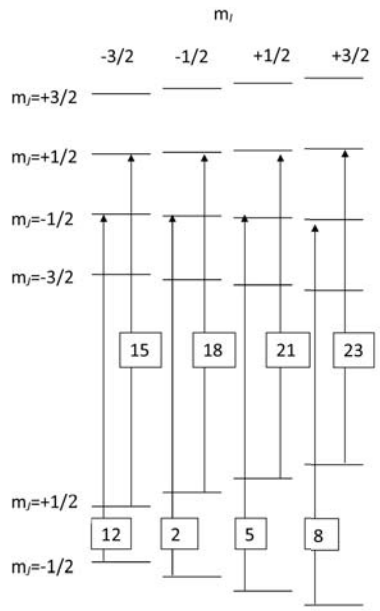

(b) Diagram 2. The transitions labels in m_I m_J basis.

The transitions labels for ^{39}K D_2 line for π polarized exciting radiation in different basis. The labels correspond to the labels on figure.

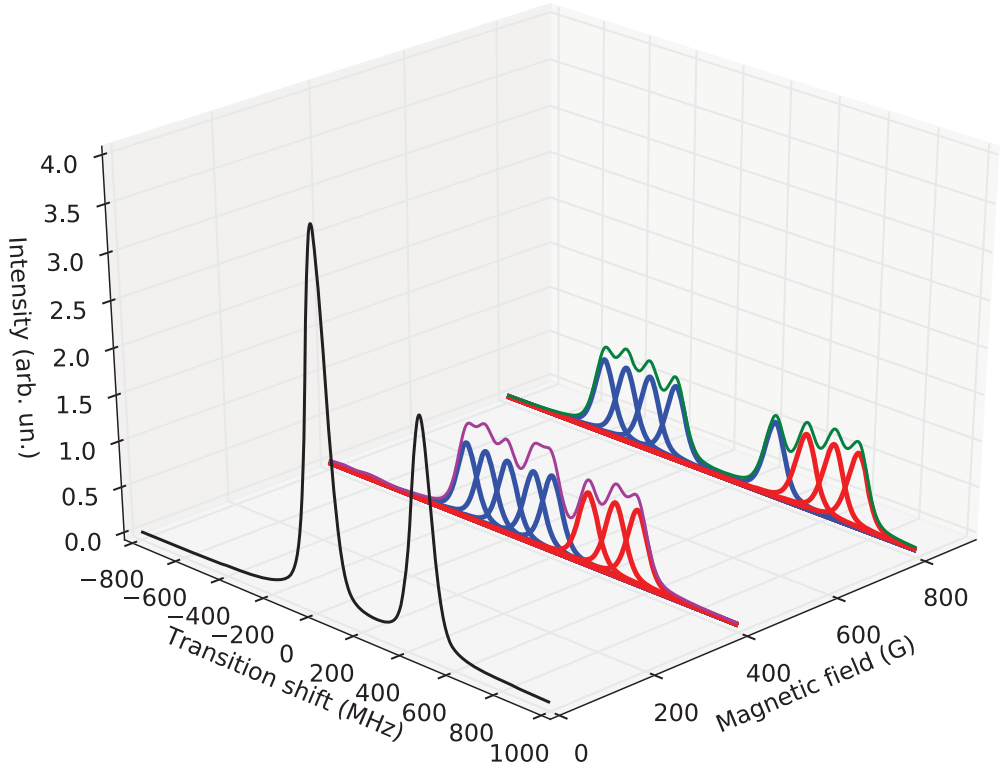

Figure 2.4: ^{39}K 3D spectra of D_2 line for π polarized exciting radiation at 0 G, 400 G and 800 G magnetic fields. The zero is $F_g = 2 \rightarrow F_e = 1$.

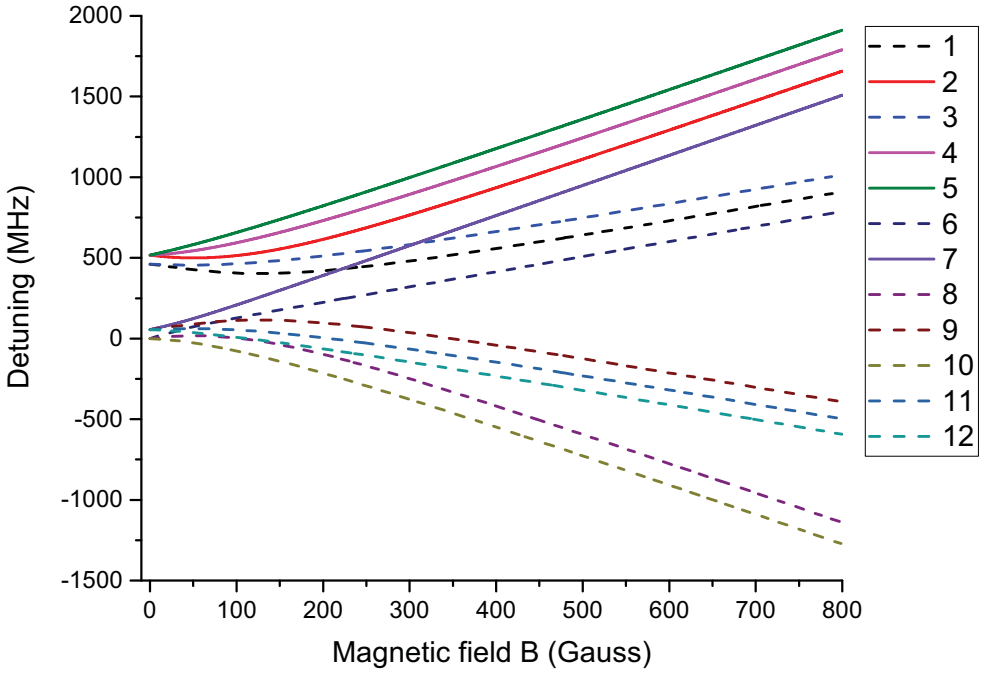

(a) Frequency shift dependence on magnetic field.

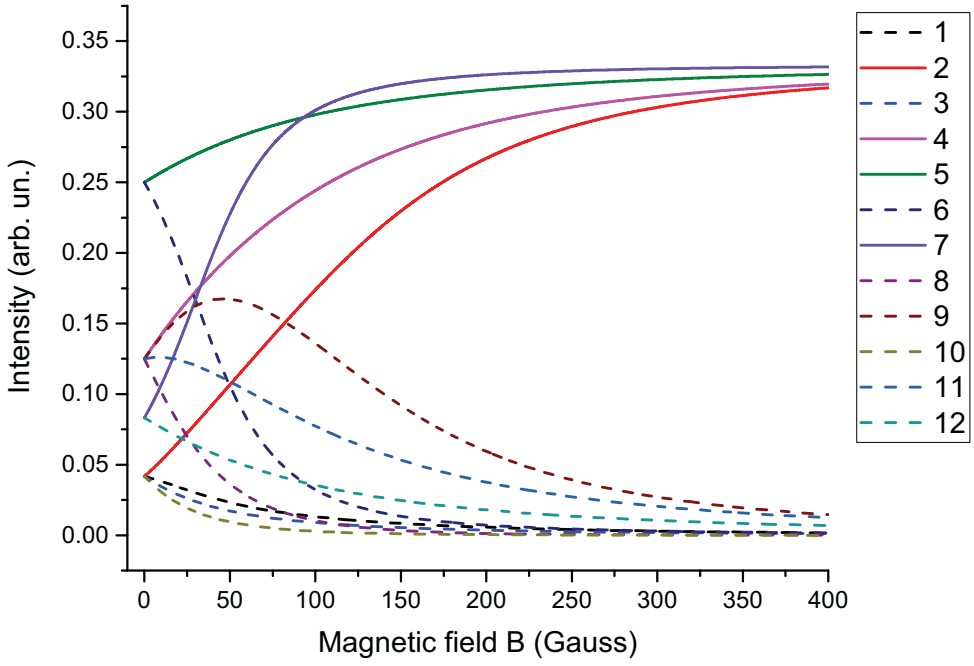

(b) The transitions intensity versus magnetic field.

Figure 2.5: The calculated frequency shift and intensity modification for ^{39}K transitions D_1 line for σ^+-polarized exciting radiation. The zero is $F_g = 2 \rightarrow F_e = 1$.

D1 line (|J=1/2> → |J'=1/2>), labels for σ^+ transitions. |F=1, m_F> → |F', $m_F'=m_F+1$>

	m_F=-2	m_F=-1	m_F=0	m_F=1	m_F=2
F'=2			2	4	5
F'=1			1	3	

D1 line (|J=1/2> → |J'=1/2>), labels for σ^+ transitions. |F=2, m_F> → |F', $m_F'=m_F+1$>

	m_F=-2	m_F=-1	m_F=0	m_F=1	m_F=2
F'=2		7	9	11	12
F'=1		6	8	10	

(a) Table 4. The transitions labels in F, m_F basis.

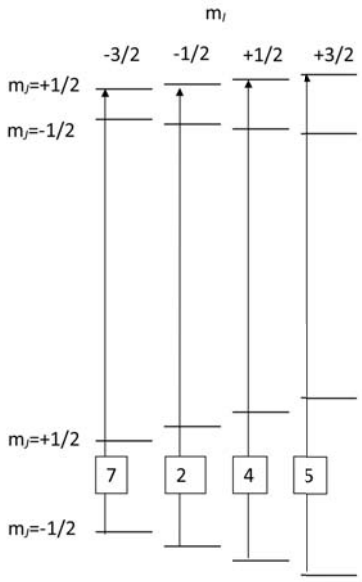

(b) Diagram 3. The transitions labels in m_I, m_J basis.

The transitions labels for ^{39}K D_1 line for σ^+-polarized exciting radiation in different basis. The labels correspond to the labels on figure.

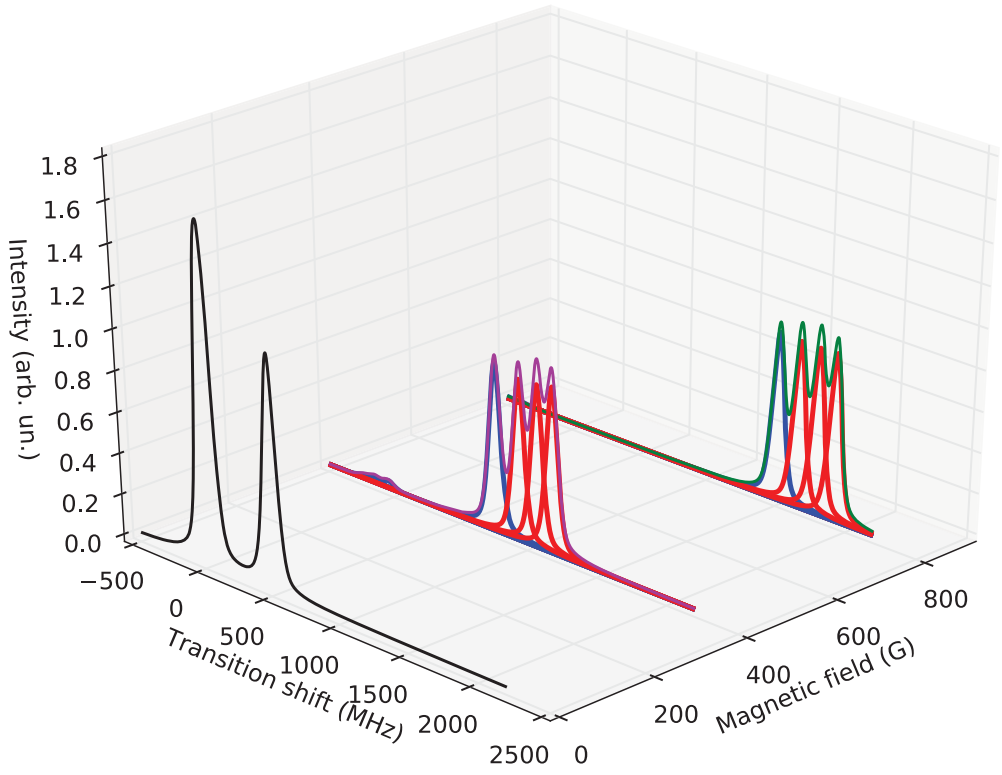

Figure 2.6: ^{39}K 3D spectra of D_1 line for σ^+-polarized exciting radiation at 0 G, 400 G and 800 G magnetic fields. The zero is $F_g = 2 \rightarrow F_e = 1$.

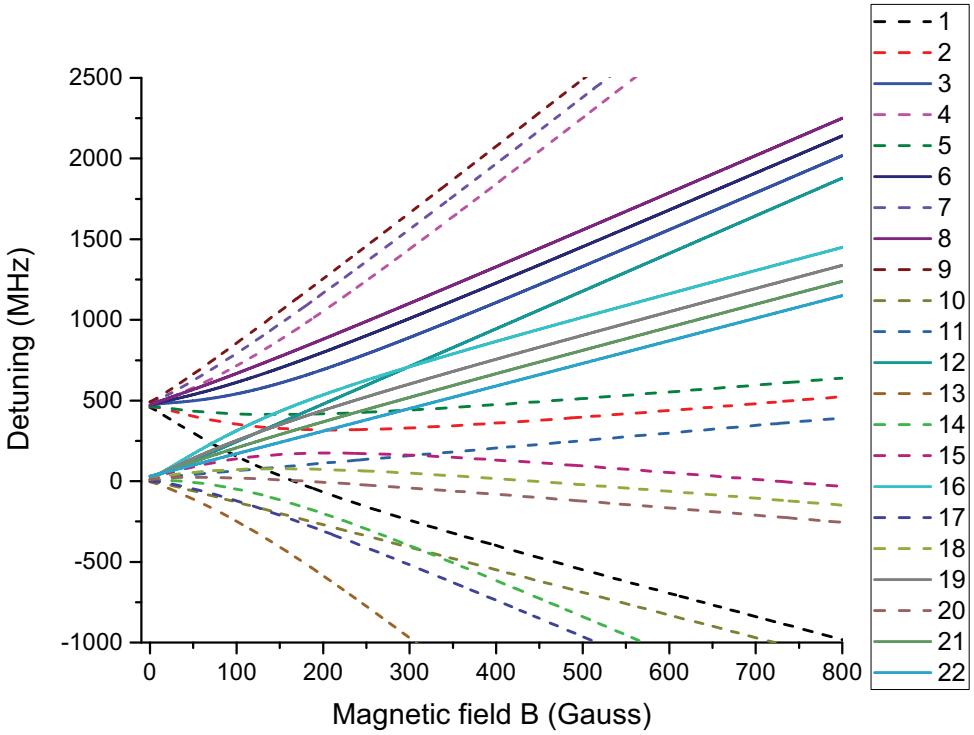

(a) Frequency shift dependence on magnetic field.

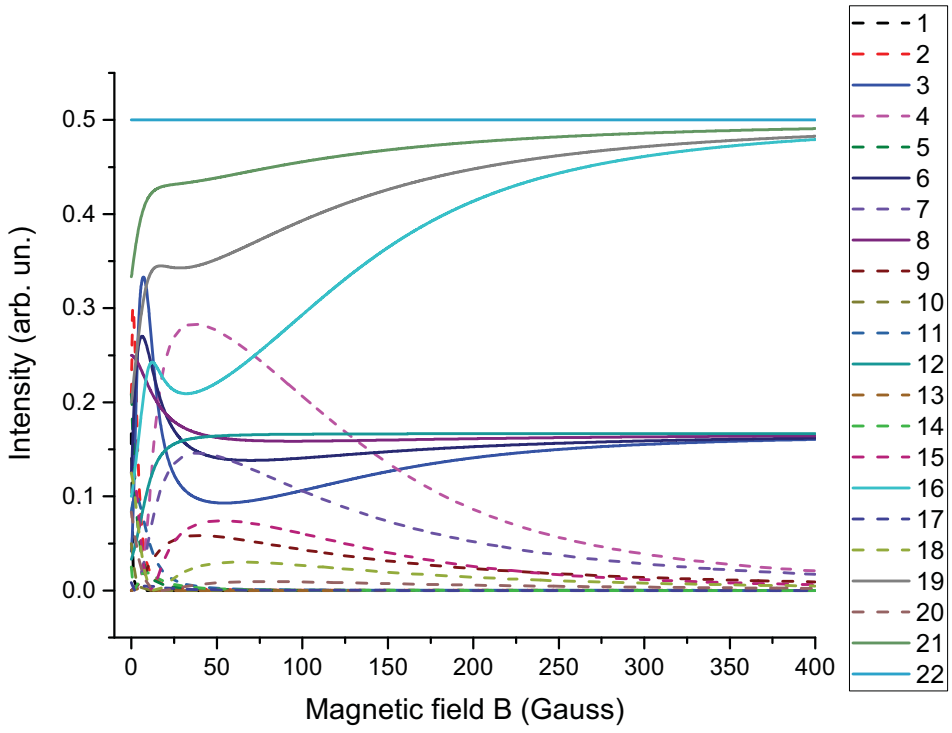

(b) The transitions intensity versus magnetic field.

Figure 2.7: The calculated frequency shift and intensity modification for ^{39}K transitions D_2 line for σ^+-polarized exciting radiation. The zero is $F_g = 2 \rightarrow F_e = 1$.

D2 line (|J=1/2> → |J'=3/2>), labels for σ^+ transitions. |F=1, m_F> → |F', m_F'=m_F+1>

	m_F=-3	m_F=-2	m_F=-1	m_F=0	m_F=1	m_F=2	m_F=3
F'=3				4	7	9	
F'=2				3	6	8	
F'=1				2	5		
F'=0				1			

D2 line (|J=1/2> → |J'=3/2>), labels for σ^+ transitions. |F=2, m_F> → |F', m_F'=m_F+1>

	m_F=-3	m_F=-2	m_F=-1	m_F=0	m_F=1	m_F=2	m_F=3
F'=3			12	16	19	21	22
F'=2			11	15	18	20	
F'=1			10	14	17		
F'=0				13			

(a) Table 5. The transitions labels in F, m_F basis.

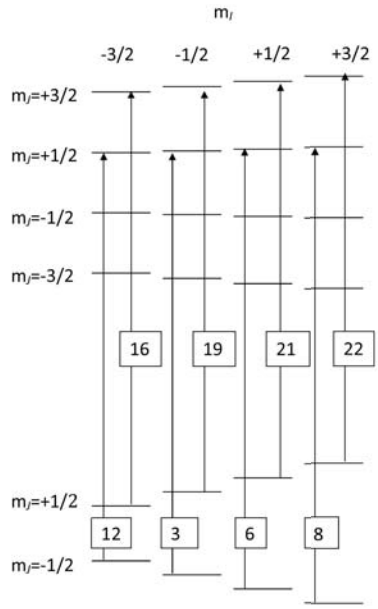

(b) Diagram 4. The transitions labels in m_I, m_J basis.

The transitions labels for ^{39}K D_2 line for σ^+-polarized exciting radiation in different basis. The labels correspond to the labels on figure.

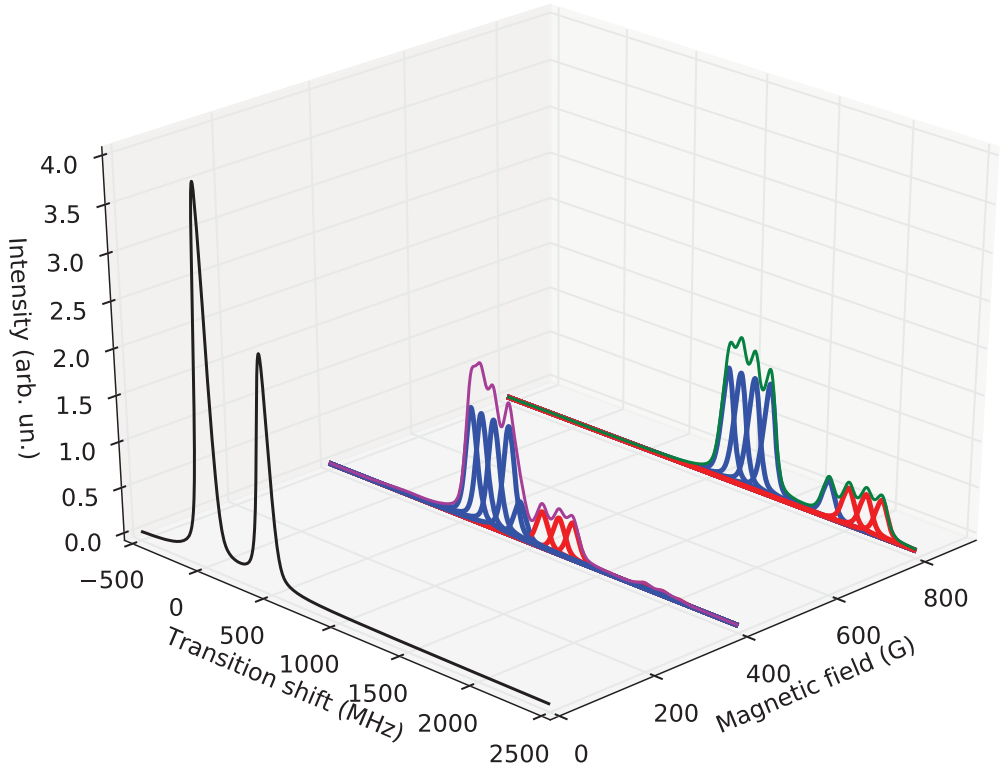

Figure 2.8: ^{39}K 3D spectra of D_2 line for σ^+-polarized exciting radiation at 0 G, 400 G and 800 G magnetic fields. The zero is $F_g = 2 \rightarrow F_e = 1$.

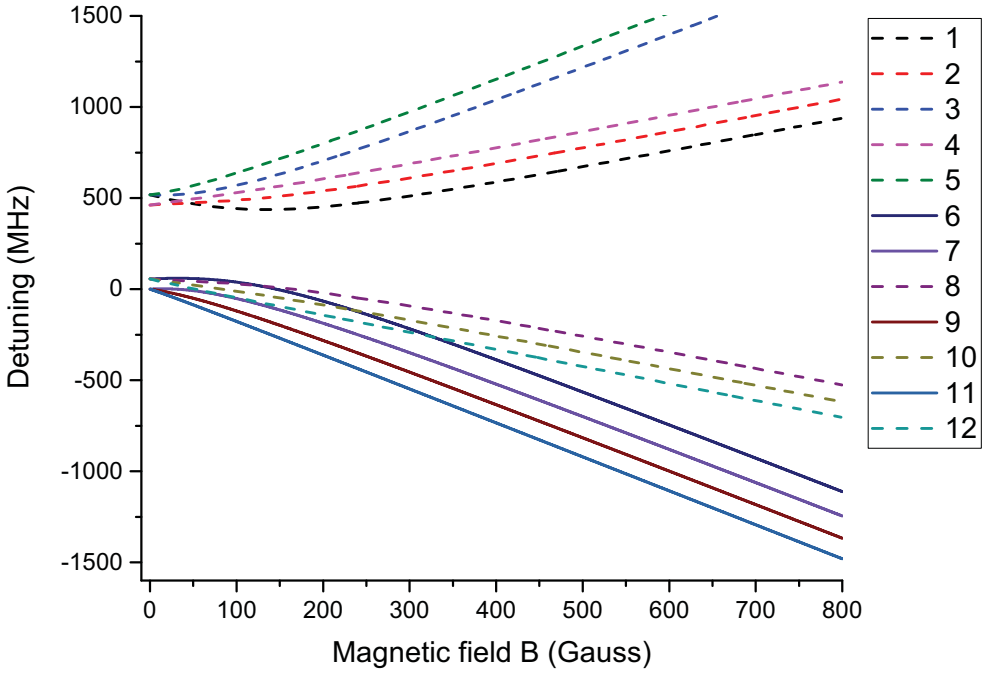

(a) Frequency shift dependence on magnetic field.

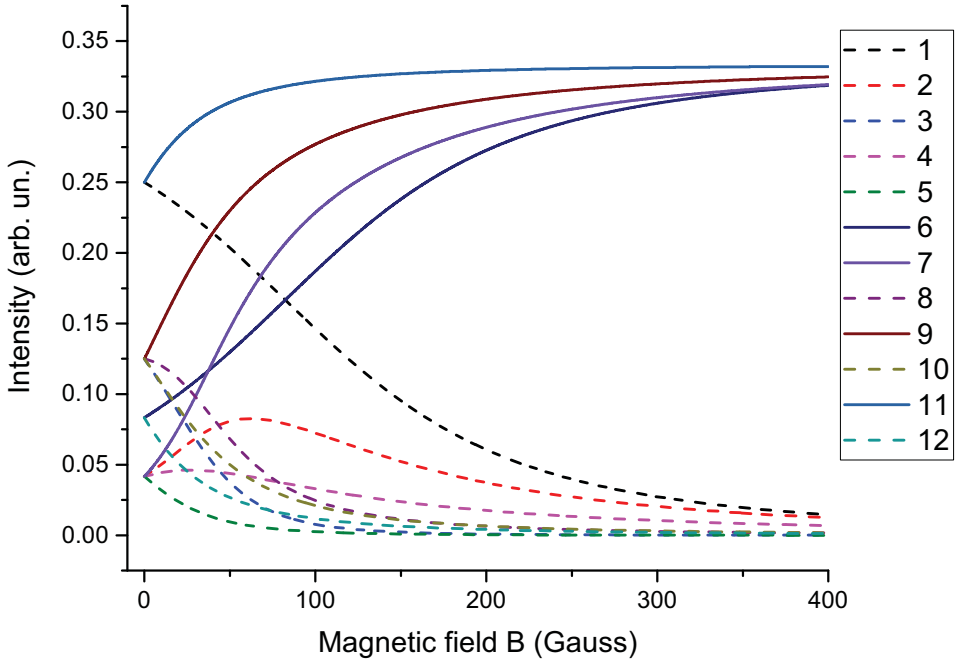

(b) The transitions intensity versus magnetic field.

Figure 2.9: The calculated frequency shift and intensity modification for ^{39}K transitions D_1 line for σ^--polarized exciting radiation. The zero is $F_g = 2 \rightarrow F_e = 1$.

D1 line (|J=1/2> → |J'=1/2>), labels for σ^- transitions. |F=1, m_F> → |F', m_F'=m_F-1>

	m_F=-2	m_F=-1	m_F=0	m_F=1	m_F=2
F'=2	1	3	5		
F'=1		2	4		

D1 line (|J=1/2> → |J'=1/2>), labels for σ^- transitions. |F=2, m_F> → |F', m_F'=m_F-1>

	m_F=-2	m_F=-1	m_F=0	m_F=1	m_F=2
F'=2	6	8	10	12	
F'=1		7	9	11	

(a) Table 6. The transitions labels in F m_F basis.

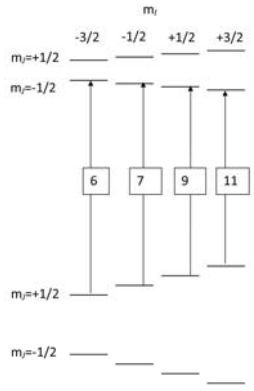

(b) Diagram 5. The transitions labels in m_I, m_J basis.

The transitions labels for ^{39}K D_1 line for σ^--polarized exciting radiation in different basis. The labels correspond to the labels on figure.

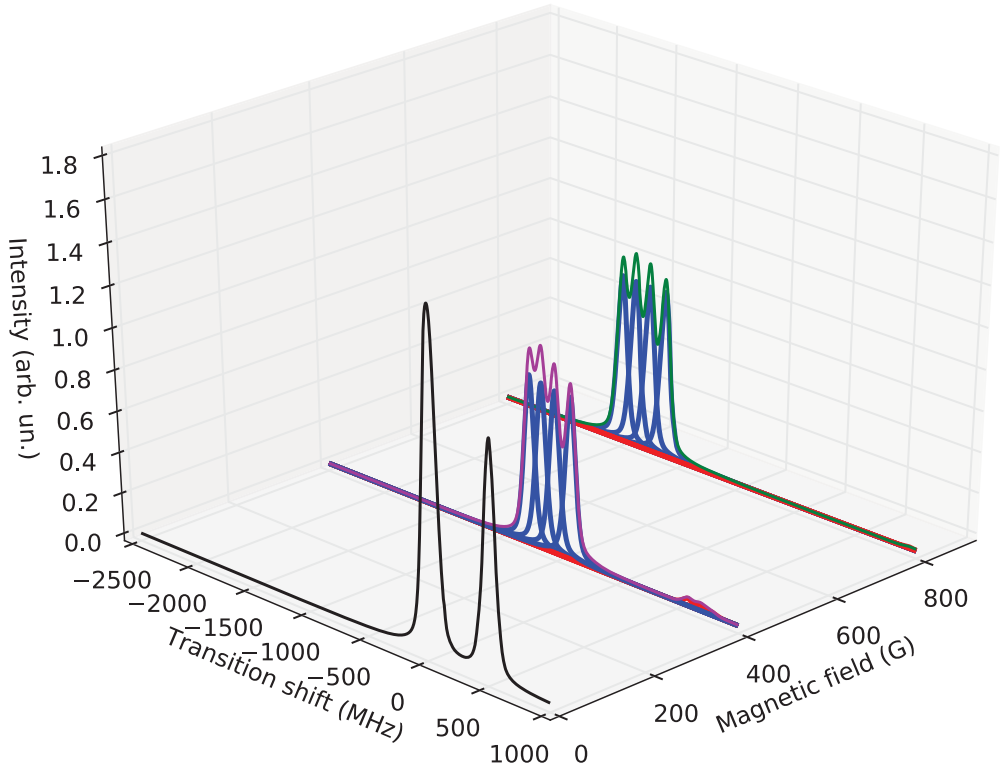

Figure 2.10: ^{39}K 3D spectra of D_1 line for σ^--polarized exciting radiation at 0 G, 400 G and 800 G magnetic fields. The zero is $F_g = 2 \rightarrow F_e = 1$.

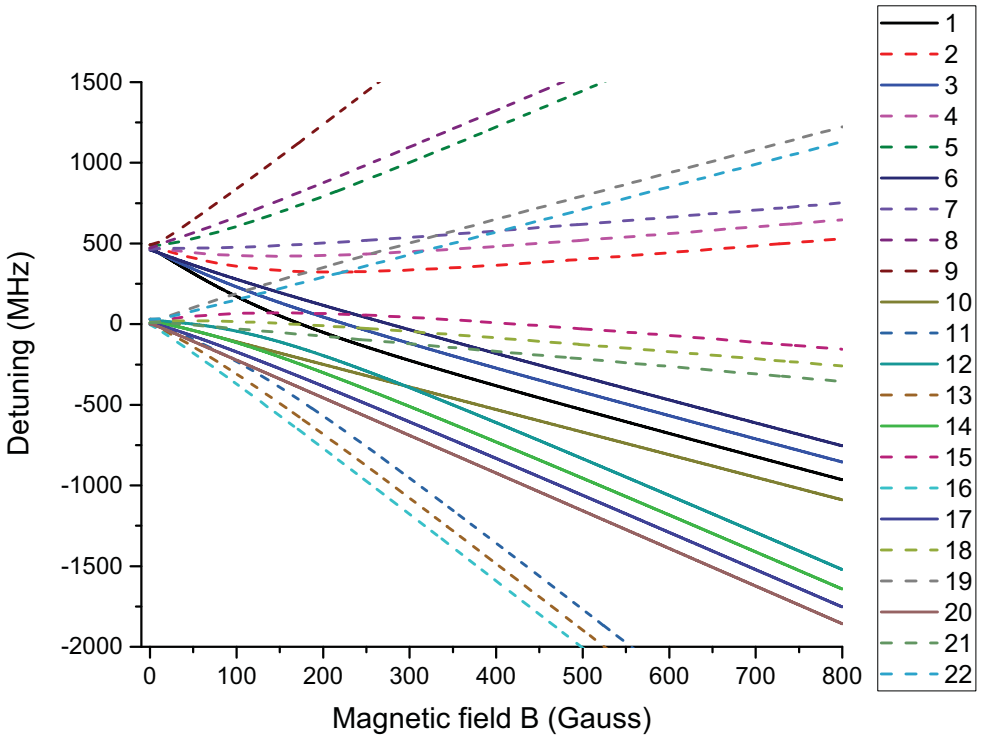

(a) Frequency shift dependence on magnetic field.

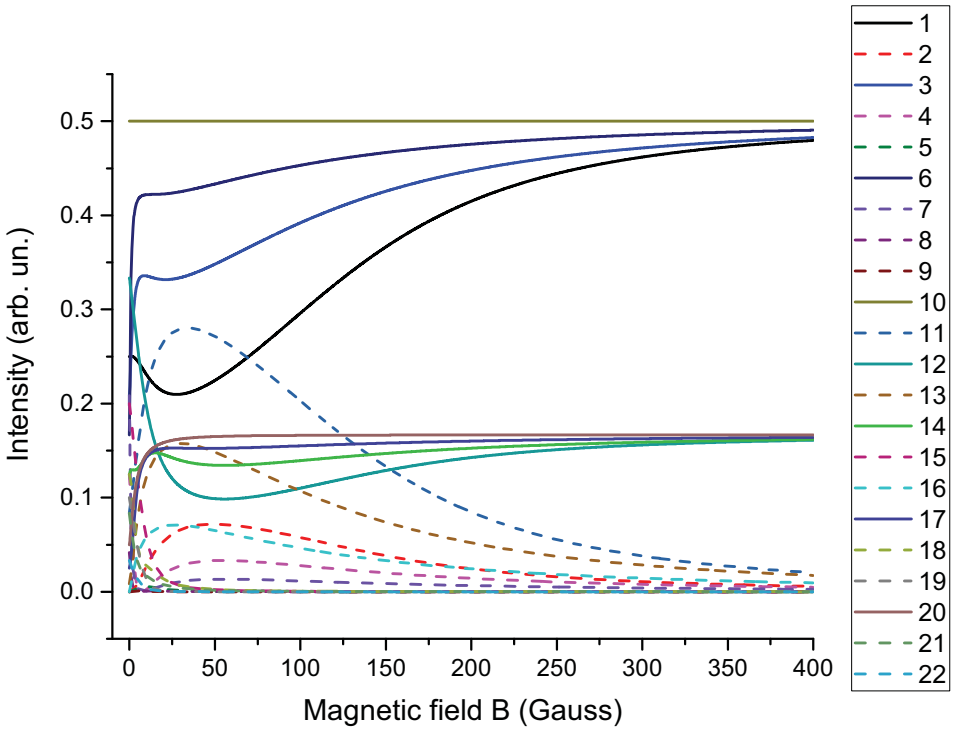

(b) The transitions intensity versus magnetic field.

Figure 2.11: The calculated frequency shift and intensity modification for ^{39}K transitions D_2 line for σ^--polarized exciting radiation. The zero is $F_g = 2 \rightarrow F_e = 1$.

D2 line (|J=1/2> → |J'=3/2>), labels for σ^- transitions. |F=1, m_F> → |F', m_F'=m_F-1>

	m_F=-3	m_F=-2	m_F=-1	m_F=0	m_F=1	m_F=2	m_F=3
F'=3		2	5	9			
F'=2		1	4	8			
F'=1			3	7			
F'=0				6			

D2 line (|J=1/2> → |J'=3/2>), labels for σ^- transitions. |F=2, m_F> → |F', m_F'=m_F-1>

	m_F=-3	m_F=-2	m_F=-1	m_F=0	m_F=1	m_F=2	m_F=3
F'=3	10	12	15	19	22		
F'=2		11	14	18	21		
F'=1			13	17	20		
F'=0				16			

(a) Table 7. The transitions labels in F, m_F basis.

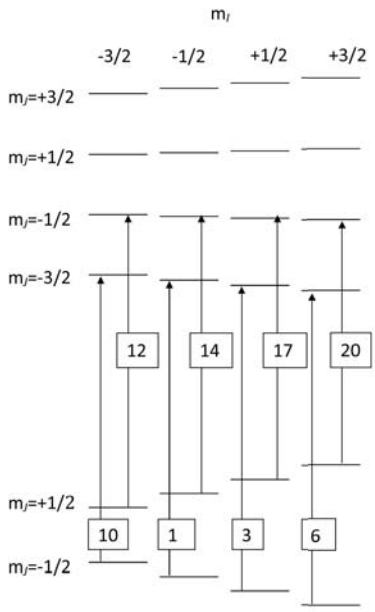

(b) Diagram 6. The transitions labels in m_I m_J basis.

The transitions labels for ^{39}K D_2 line for σ^--polarized exciting radiation in different basis. The labels correspond to the labels on figure.

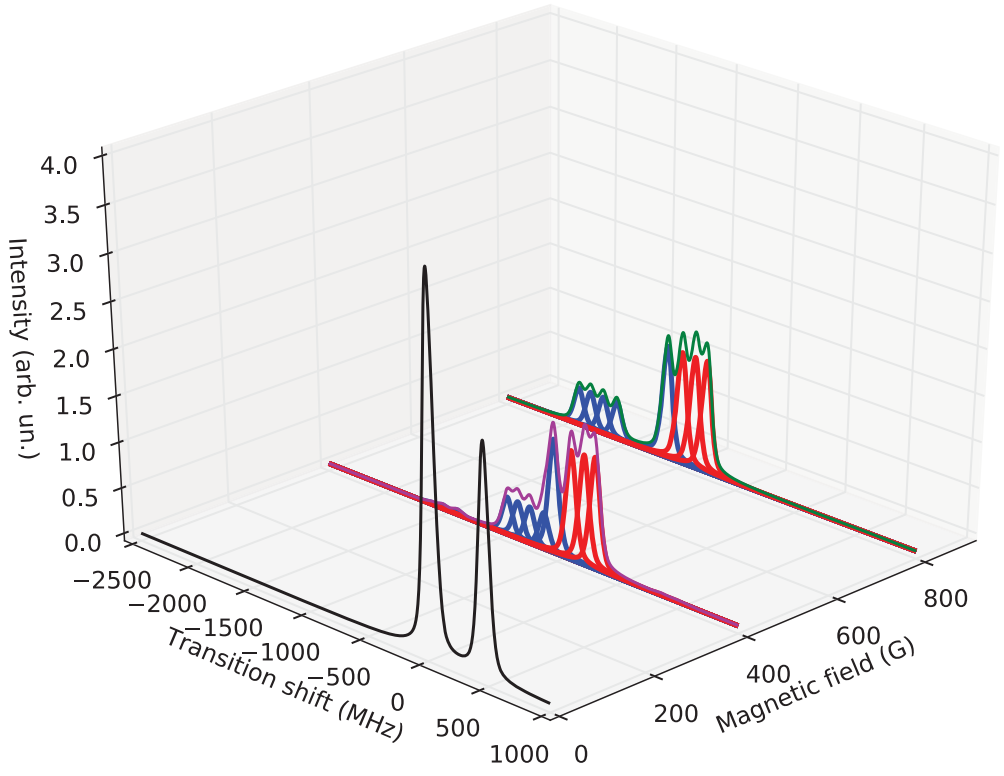

Figure 2.12: ^{39}K 3D spectra of D_2 line for σ^--polarized exciting radiation at 0 G, 400 G and 800 G magnetic fields. The zero is $F_g = 2 \rightarrow F_e = 1$.

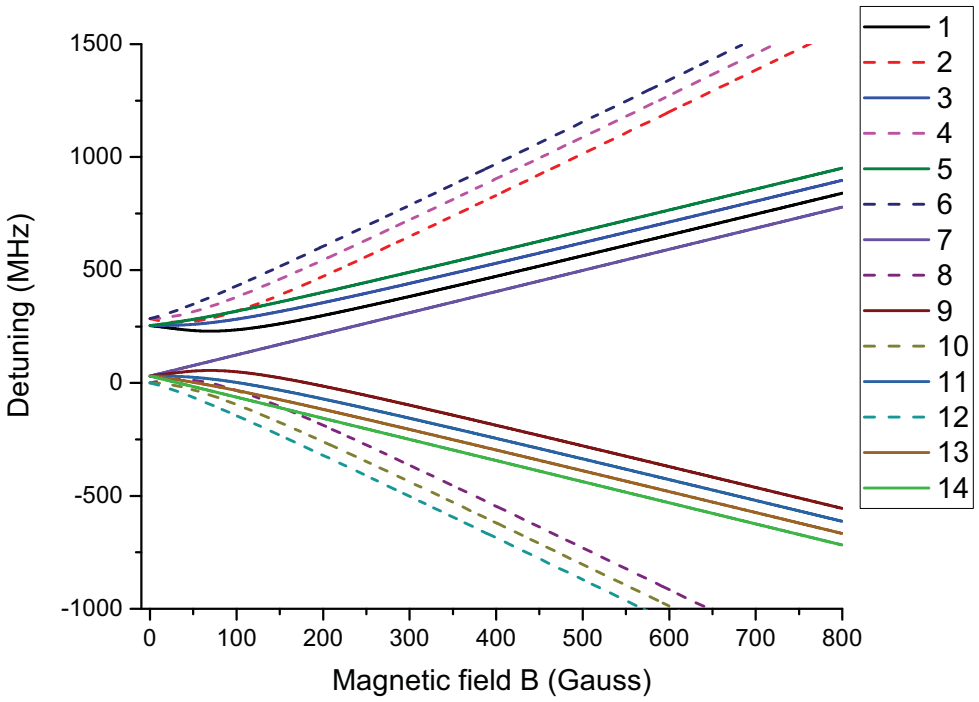

(a) Frequency shift dependence on magnetic field.

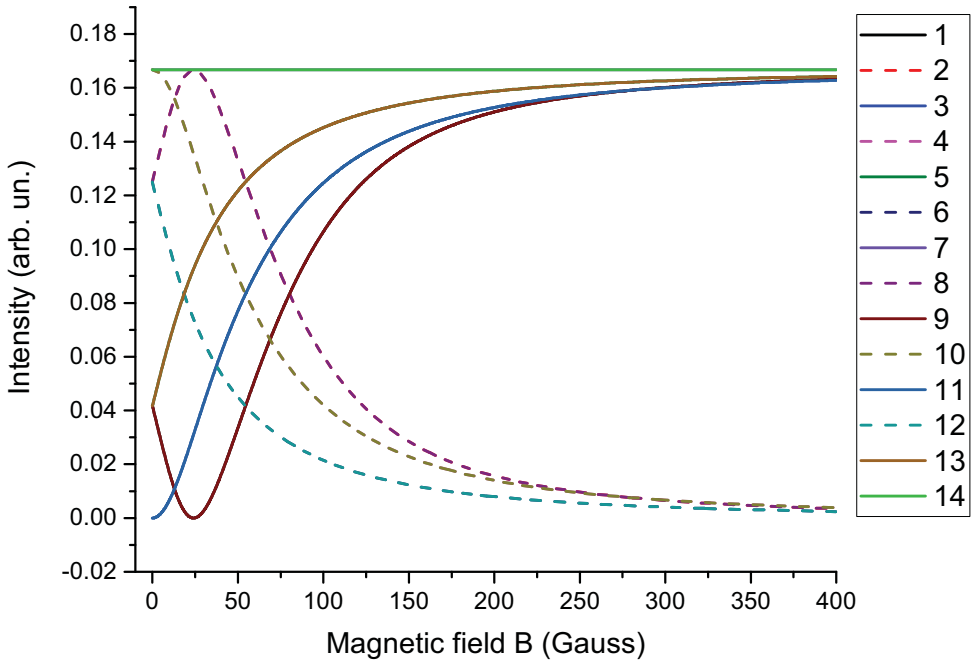

(b) The transitions intensity versus magnetic field.

Figure 2.13: The calculated frequency shift and intensity modification for ^{41}K transitions D_1 line for π polarized exciting radiation. The zero is $F_g = 2 \rightarrow F_e = 1$.

D1 line (|J=1/2> → |J'=1/2>), labels for π transitiors. |F=1, m_F> → |F', m_F'=m_F>

	m_F=-2	m_F=-1	m_F=0	m_F=1	m_F=2
F'=2		2	4	6	
F'=1		1	3	5	

D1 line (|J=1/2> → |J'=1/2>), labels for π transitiors. |F=2, m_F> → |F', m_F'=m_F>

	m_F=-2	m_F=-1	m_F=0	m_F=1	m_F=2
F'=2	7	9	11	13	14
F'=1		8	10	12	

(a) Table 8. The transitions labels in F m_F basis.

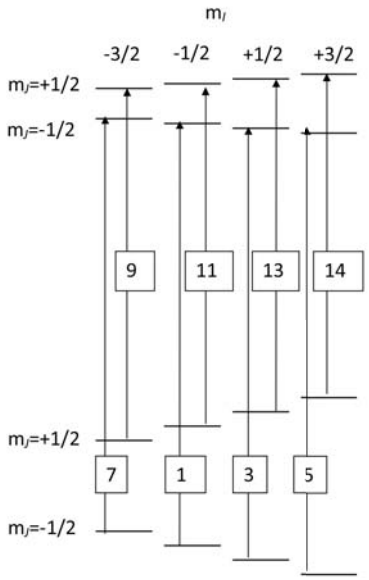

(b) Diagram 7. The transitions labels in m_I m_J basis.

The transitions labels for ^{41}K D_1 line for π polarized exciting radiation in different basis. The labels correspond to the labels on figure.

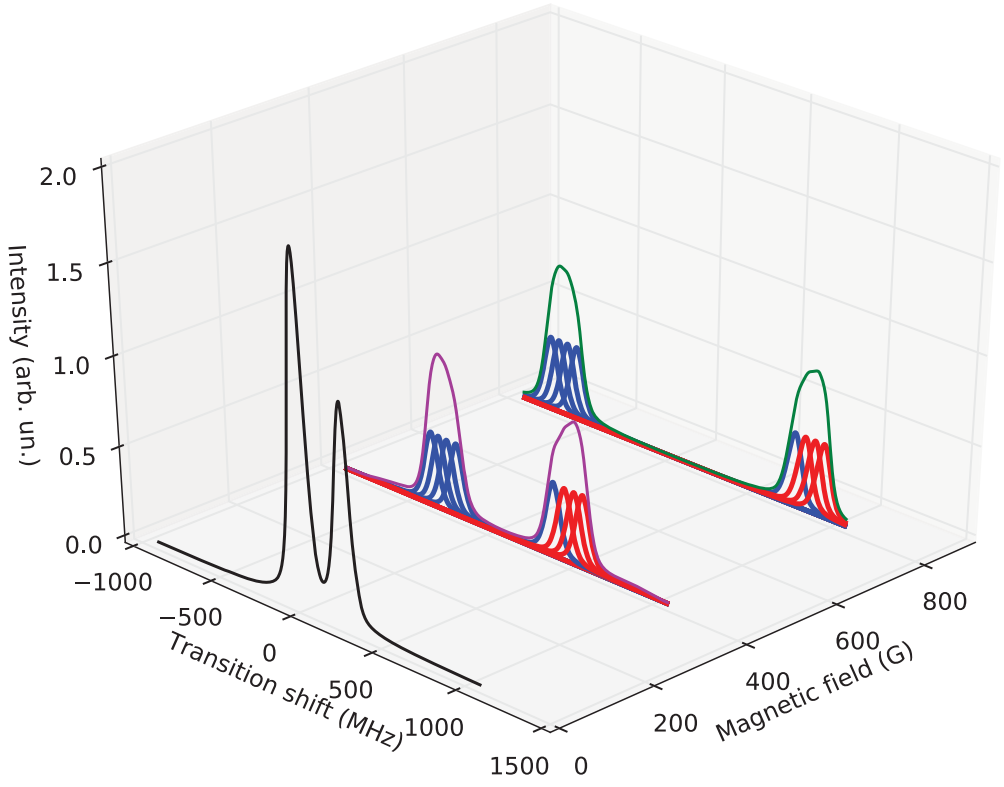

Figure 2.14: ^{41}K 3D spectra of D_1 line for π polarized exciting radiation at 0 G, 400 G and 800 G magnetic fields. The zero is $F_g = 2 \rightarrow F_e = 1$.

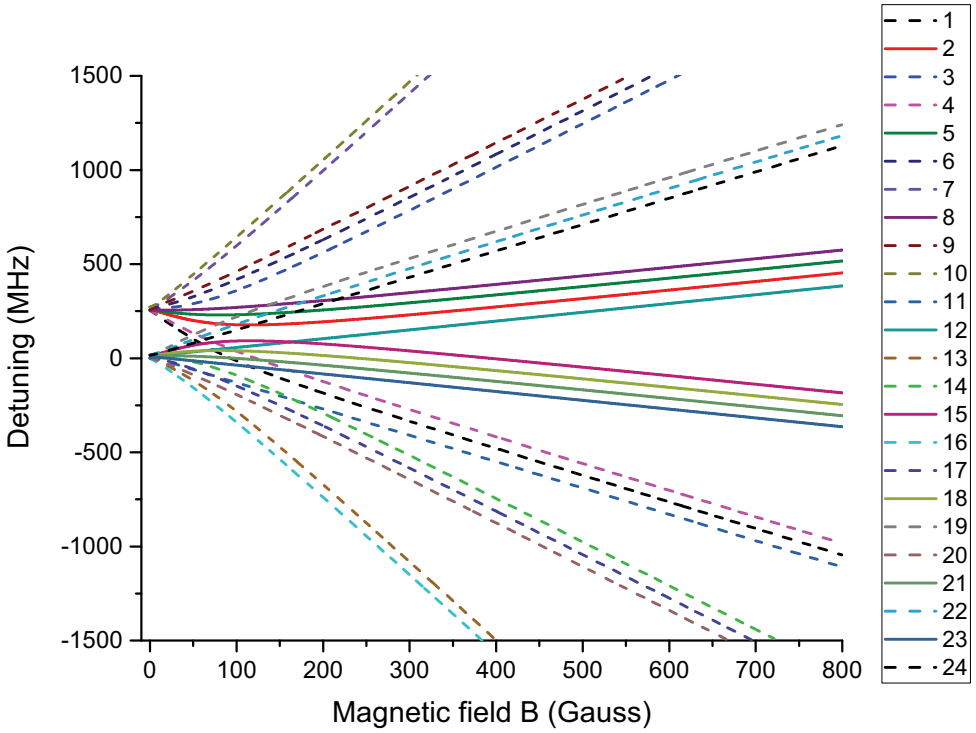

(a) Frequency shift dependence on magnetic field.

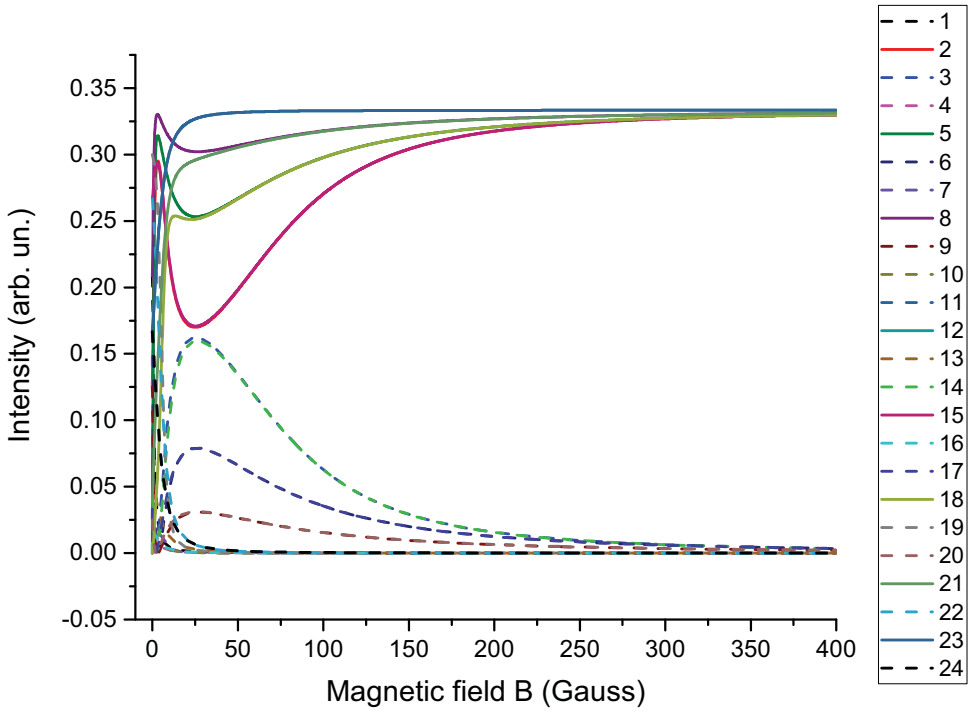

(b) The transitions intensity versus magnetic field.

Figure 2.15: The calculated frequency shift and intensity modification for ^{41}K transitions D_2 line for π polarized exciting radiation. The zero is $F_g = 2 \rightarrow F_e = 1$.

D2 line (|J=1/2> → |J'=3/2>), labels for π transitions. |F=1, m_F> → |F', m_F'=m_F>

	m_F=-3	m_F=-2	m_F=-1	m_F=0	m_F=1	m_F=2	m_F=3
F'=3			3	7	10		
F'=2			2	6	9		
F'=1			1	5	8		
F'=0				4			

D2 line (|J=1/2> → |J'=3/2>), labels for π transitions. |F=2, m_F> → |F', m_F'=m_F>

	m_F=-3	m_F=-2	m_F=-1	m_F=0	m_F=1	m_F=2	m_F=3
F'=3		12	15	19	22	24	
F'=2		11	14	18	21	23	
F'=1			13	17	20		
F'=0				16			

(a) Table 9. The transitions labels in F m_F basis.

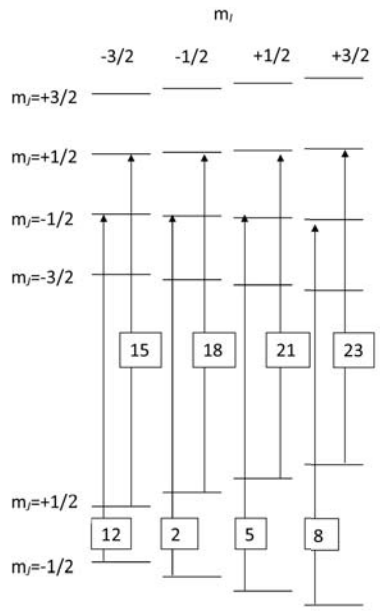

(b) Diagram 8. The transitions labels in m_I m_J basis.

The transitions labels for ^{41}K D_2 line for π polarized exciting radiation in different basis. The labels correspond to the labels on figure.

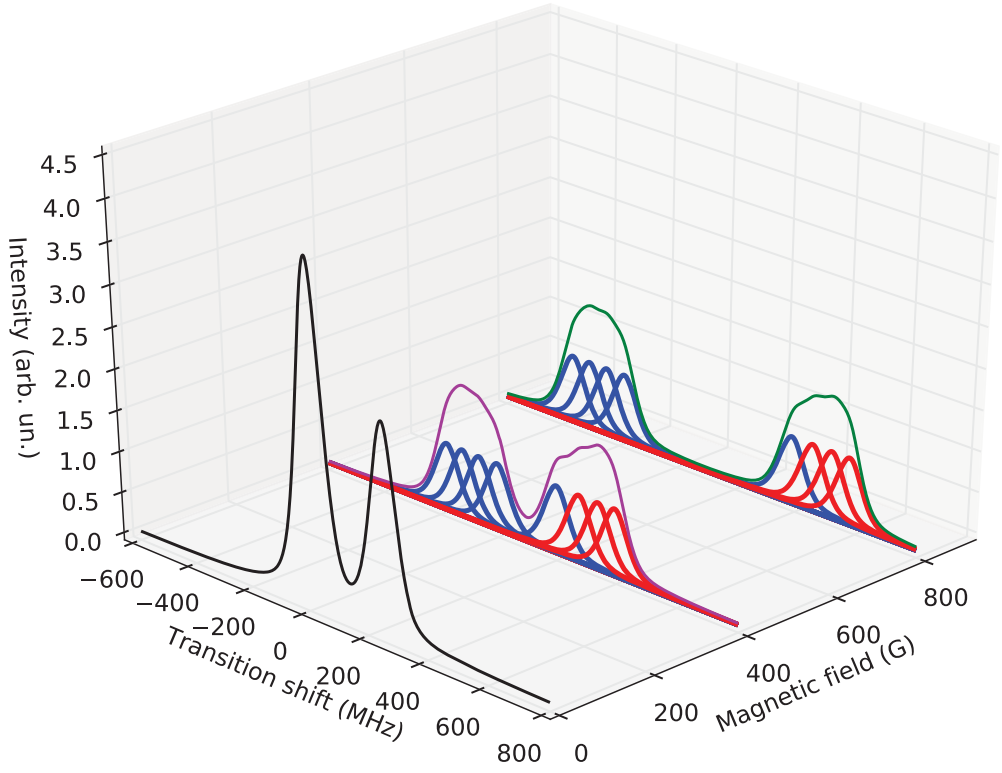

Figure 2.16: ^{41}K 3D spectra of D_2 line for π polarized exciting radiation at 0 G, 400 G and 800 G magnetic fields. The zero is $F_g = 2 \rightarrow F_e = 1$.

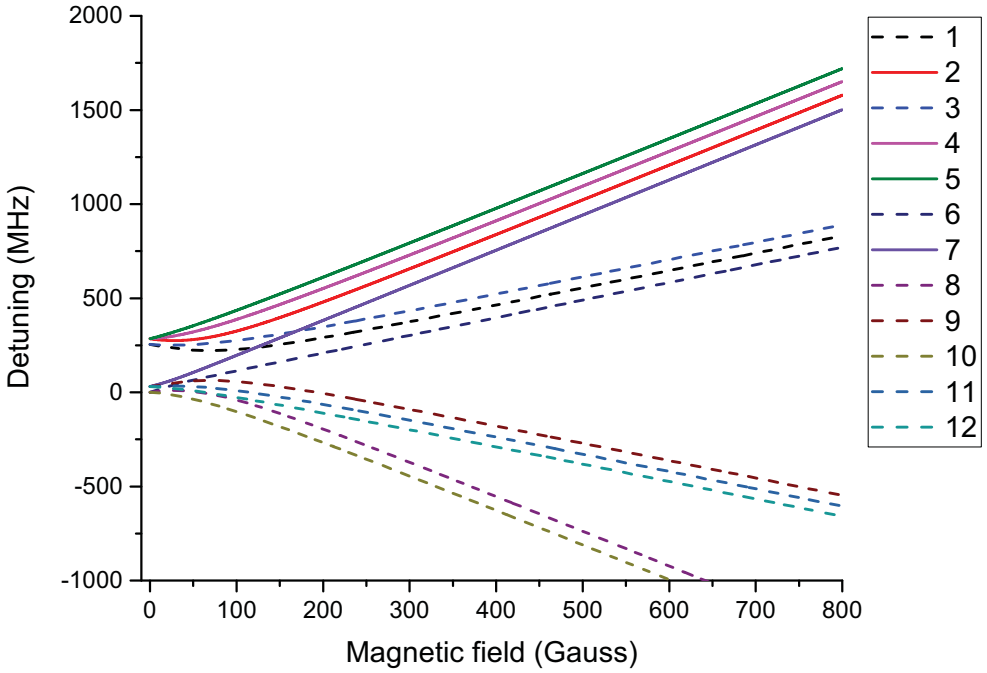

(a) Frequency shift dependence on magnetic field.

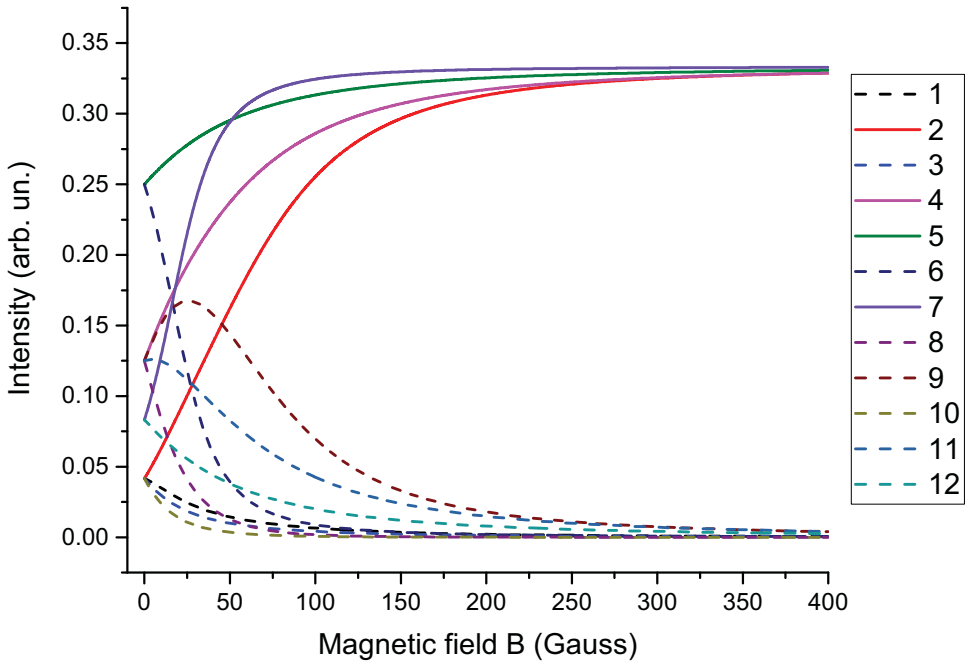

(b) The transitions intensity versus magnetic field.

Figure 2.17: The calculated frequency shift and intensity modification for ^{41}K transitions D_1 line for σ^+-polarized exciting radiation. The zero is $F_g = 2 \rightarrow F_e = 1$.

D1 line (|J=1/2> → |J'=1/2>), labels for σ^+ transitions. |F=1, m_F> → |F', $m_F'=m_F+1$>

	m_F=-2	m_F=-1	m_F=0	m_F=1	m_F=2
F'=2			2	4	5
F'=1			1	3	

D1 line (|J=1/2> → |J'=1/2>), labels for σ^+ transitions. |F=2, m_F> → |F', $m_F'=m_F+1$>

	m_F=-2	m_F=-1	m_F=0	m_F=1	m_F=2
F'=2		7	9	11	12
F'=1		6	8	10	

(a) Table 10. The transitions labels in F m_F basis.

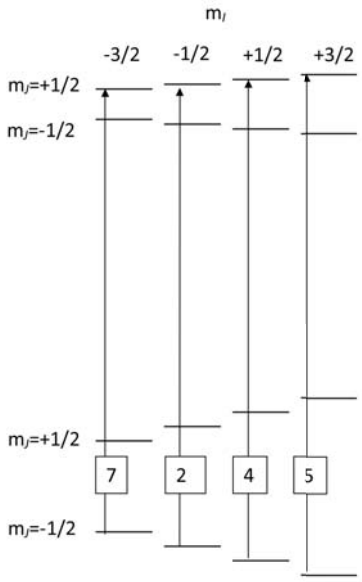

(b) Diagram 9. The transitions labels in m_I m_J basis.

The transitions labels for ^{41}K D_1 line for σ^+-polarized exciting radiation in different basis. The labels correspond to the labels on figure.

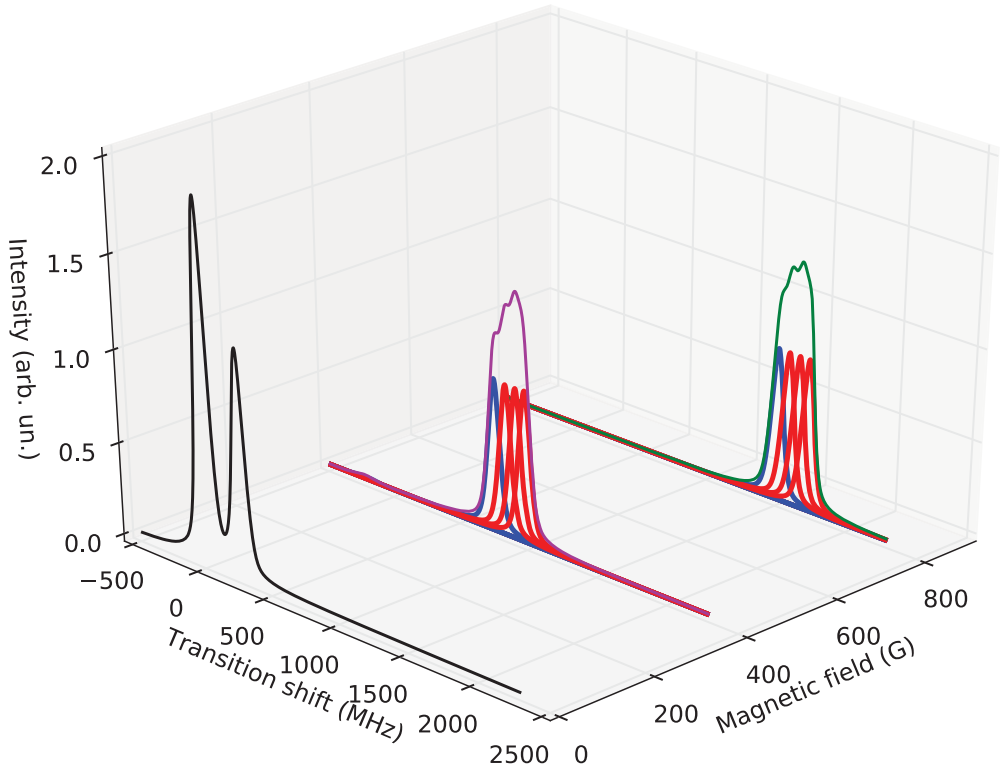

Figure 2.18: ^{41}K 3D spectra of D_1 line for σ^+-polarized exciting radiation at 0 G, 400 G and 800 G magnetic fields. The zero is $F_g = 2 \rightarrow F_e = 1$.

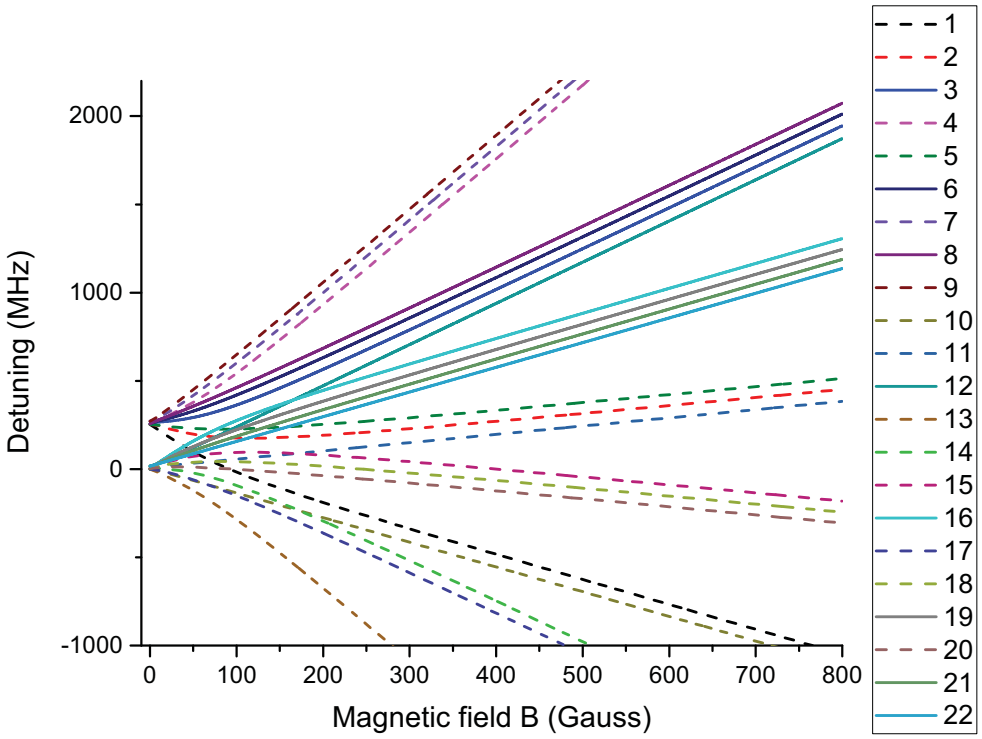

(a) Frequency shift dependence on magnetic field.

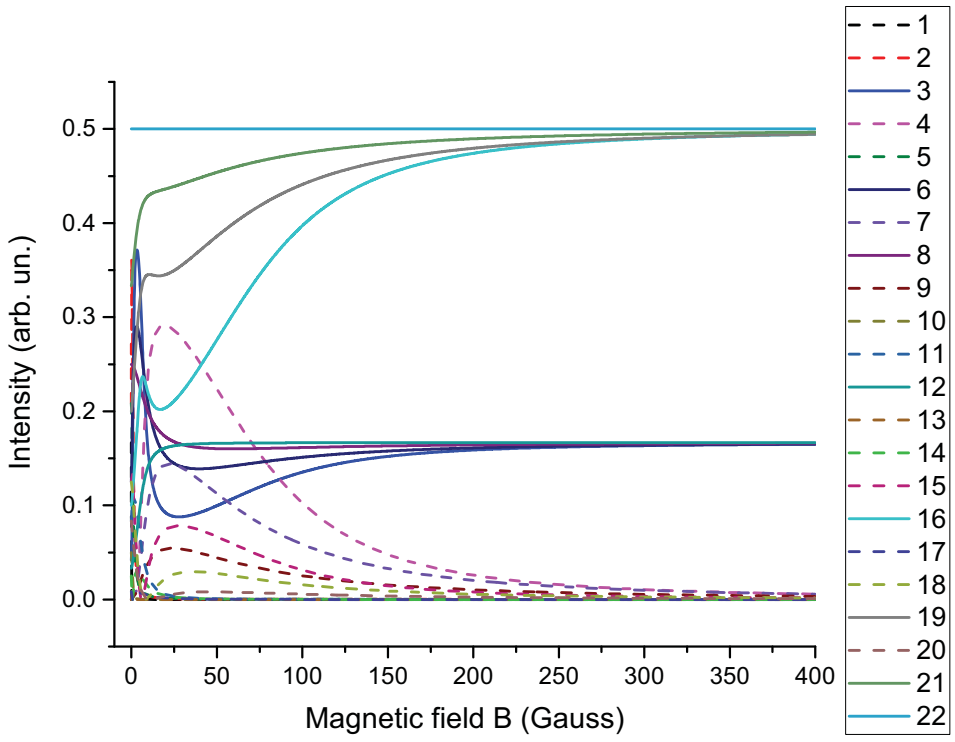

(b) The transitions intensity versus magnetic field.

Figure 2.19: The calculated frequency shift and intensity modification for ^{41}K transitions D_2 line for σ^+-polarized exciting radiation. The zero is $F_g = 2 \rightarrow F_e = 1$.

D2 line (|J=1/2> → |J'=3/2>), labels for σ^+ transitions. |F=1, m_F> → |F', m_F'=m_F+1>

	m_F=-3	m_F=-2	m_F=-1	m_F=0	m_F=1	m_F=2	m_F=3
F'=3				4	7	9	
F'=2				3	6	8	
F'=1				2	5		
F'=0				1			

D2 line (|J=1/2> → |J'=3/2>), labels for σ^+ transitions. |F=2, m_F> → |F', m_F'=m_F+1>

	m_F=-3	m_F=-2	m_F=-1	m_F=0	m_F=1	m_F=2	m_F=3
F'=3			12	16	19	21	22
F'=2			11	15	18	20	
F'=1			10	14	17		
F'=0				13			

(a) Table 11. The transitions labels in F m_F basis.

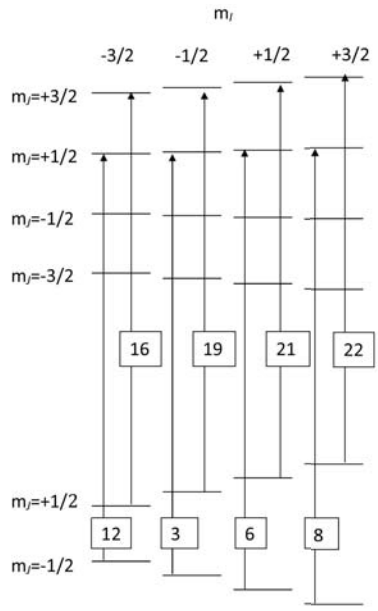

(b) Diagram 10. The transitions labels in m_I m_J basis.

The transitions labels for ^{41}K D_2 line for σ^+-polarized exciting radiation in different basis. The labels correspond to the labels on figure.

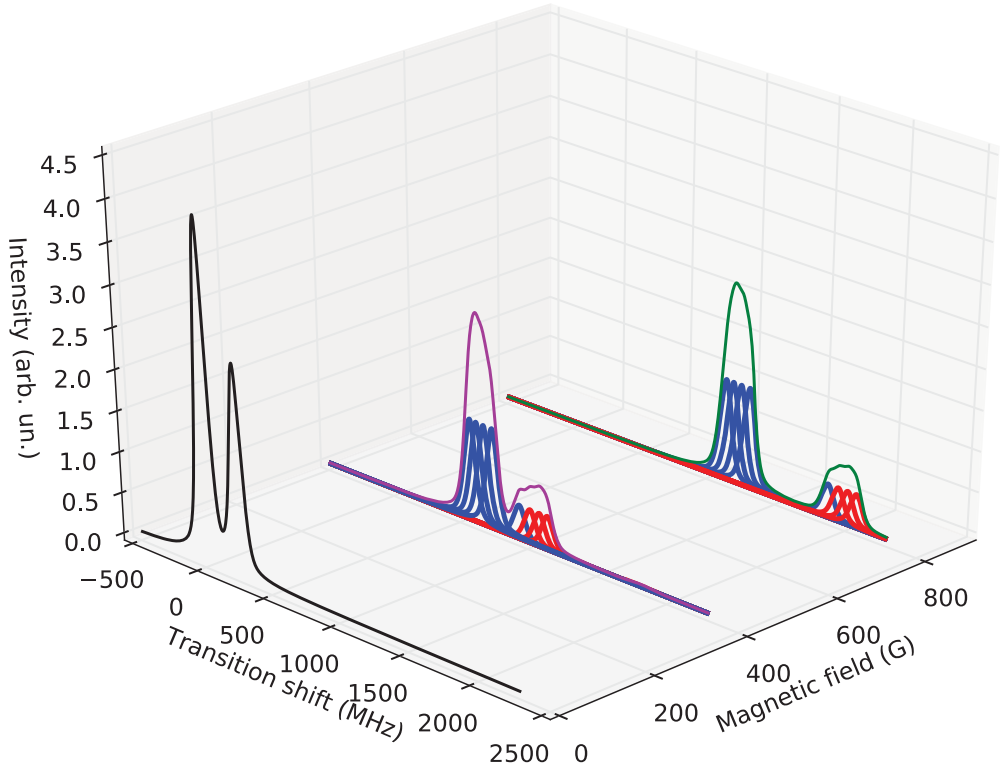

Figure 2.20: ^{41}K 3D spectra of D_2 line for σ^+-polarized exciting radiation at 0 G, 400 G and 800 G magnetic fields. The zero is $F_g = 2 \rightarrow F_e = 1$.

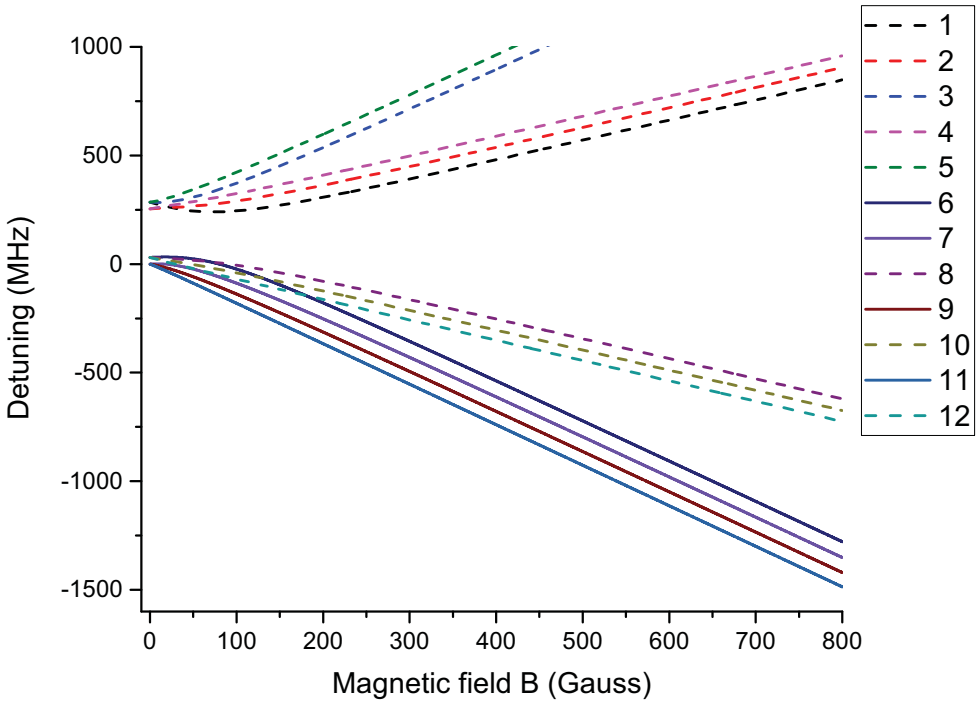

(a) Frequency shift dependence on magnetic field.

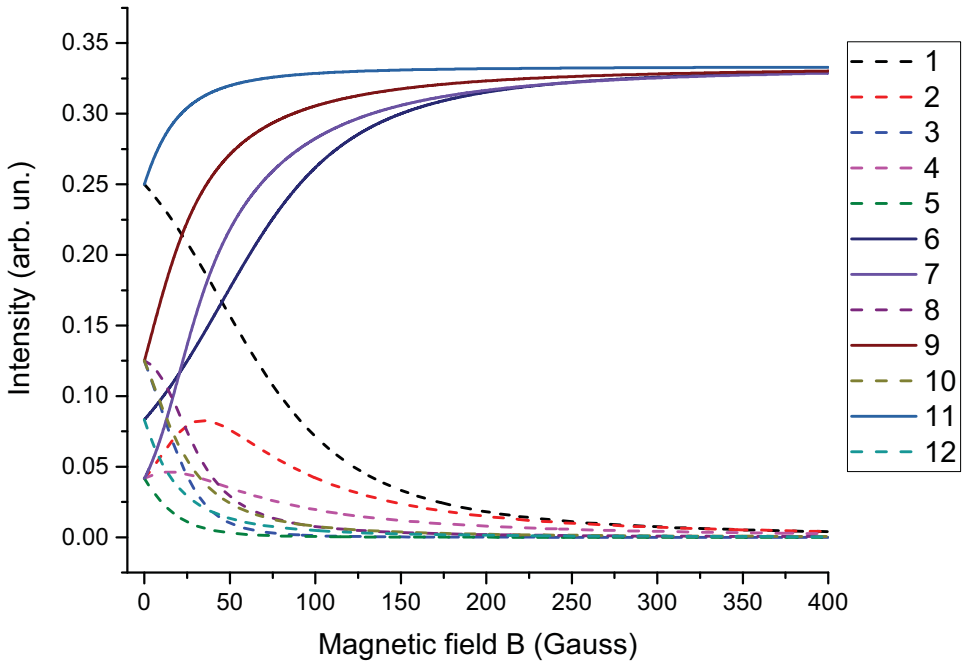

(b) The transitions intensity versus magnetic field.

Figure 2.21: The calculated frequency shift and intensity modification for ^{41}K transitions D_1 line for σ^--polarized exciting radiation. The zero is $F_g = 2 \rightarrow F_e = 1$.

D1 line (|J=1/2> → |J'=1/2>), labels for σ^- transitions. |F=1, m_F> → |F', m_F'=m_F-1>

	m_F=-2	m_F=-1	m_F=0	m_F=1	m_F=2
F'=2	1	3	5		
F'=1		2	4		

D1 line (|J=1/2> → |J'=1/2>), labels for σ^- transitions. |F=2, m_F> → |F', m_F'=m_F-1>

	m_F=-2	m_F=-1	m_F=0	m_F=1	m_F=2
F'=2	6	8	10	12	
F'=1		7	9	11	

(a) Table 12. The transitions labels in F m_F basis.

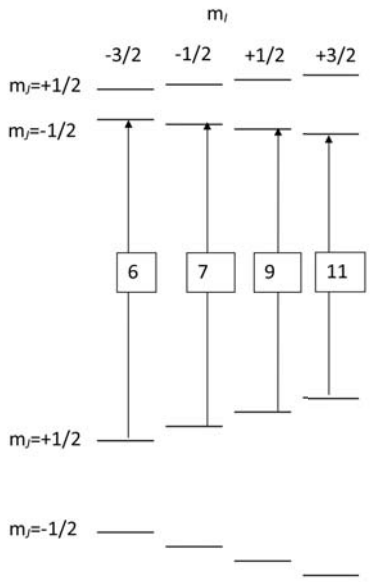

(b) Diagram 11. The transitions labels in m_I m_J basis.

The transitions labels for ^{41}K D_1 line for σ^--polarized exciting radiation in different basis. The labels correspond to the labels on figure.

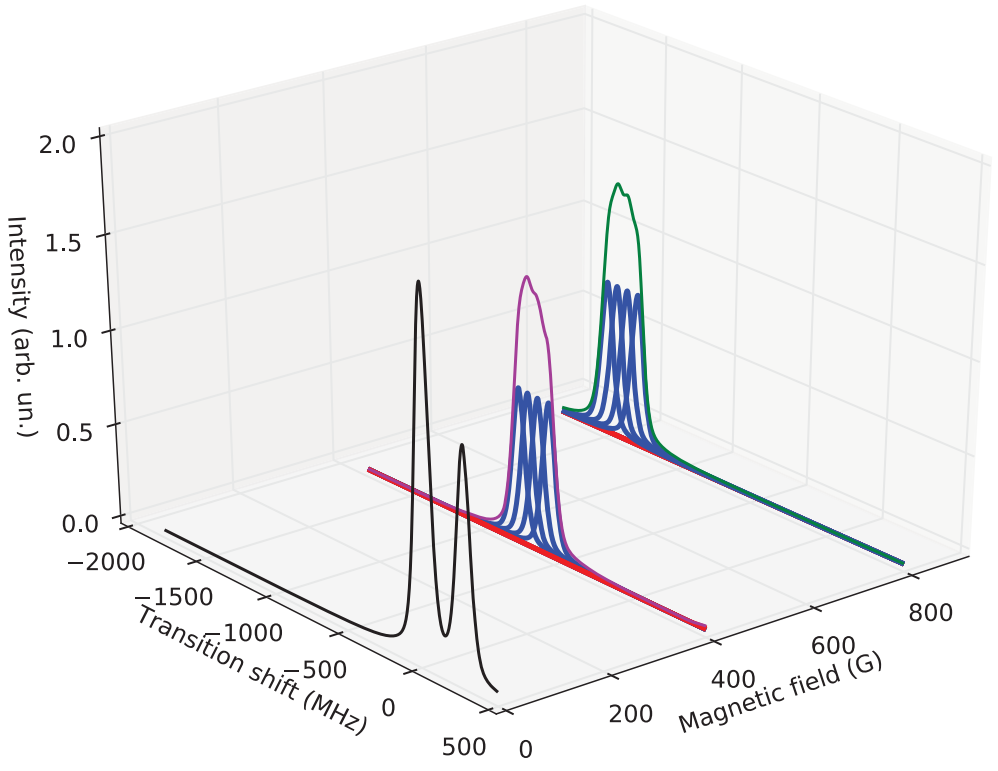

Figure 2.22: ^{41}K 3D spectra of D_1 line for σ^--polarized exciting radiation at 0 G, 400 G and 800 G magnetic fields. The zero is $F_g = 2 \rightarrow F_e = 1$.

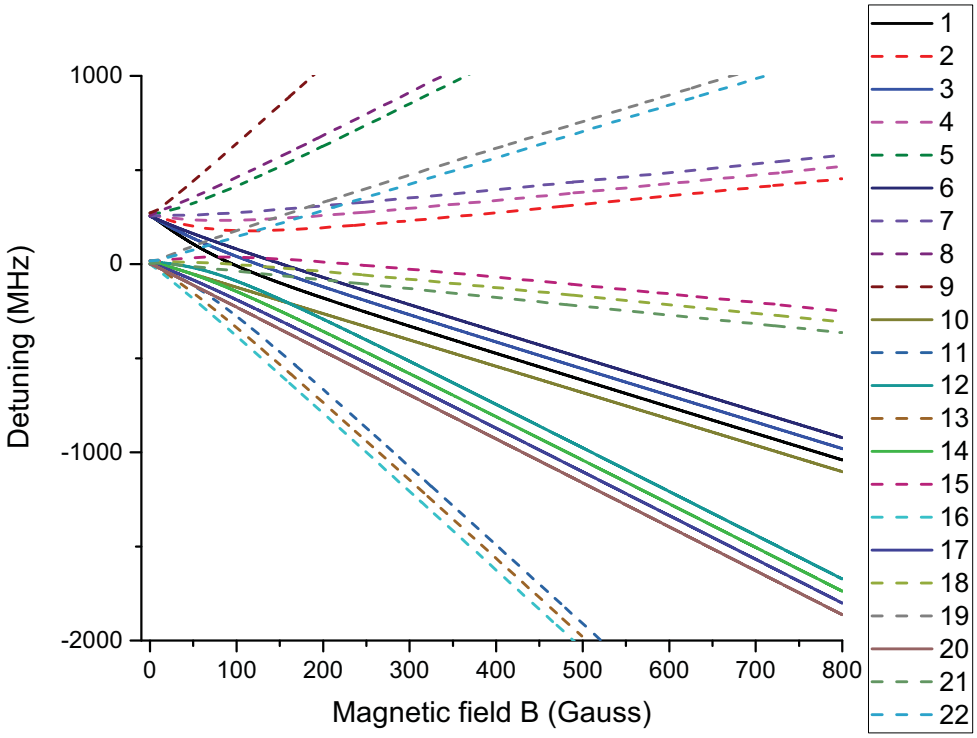

(a) Frequency shift dependence on magnetic field.

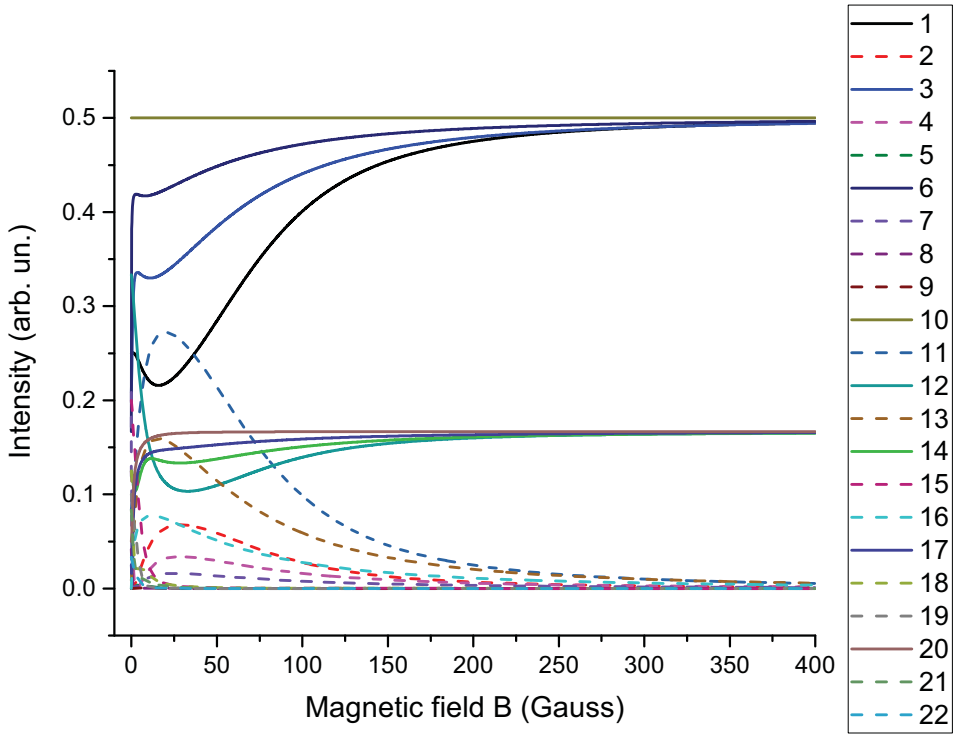

(b) The transitions intensity versus magnetic field.

Figure 2.23: The calculated frequency shift and intensity modification for ^{41}K transitions D_2 line for σ^--polarized exciting radiation. The zero is $F_g = 2 \rightarrow F_e = 1$.

D2 line (|J=1/2> → |J'=3/2>), labels for σ^- transitions. |F=1, m_F> → |F', m_F'=m_F-1>

	m_F=-3	m_F=-2	m_F=-1	m_F=0	m_F=1	m_F=2	m_F=3
F'=3		2	5	9			
F'=2		1	4	8			
F'=1			3	7			
F'=0				6			

D2 line (|J=1/2> → |J'=3/2>), labels for σ^- transitions. |F=2, m_F> → |F', m_F'=m_F-1>

	m_F=-3	m_F=-2	m_F=-1	m_F=0	m_F=1	m_F=2	m_F=3
F'=3	10	12	15	19	22		
F'=2		11	14	18	21		
F'=1			13	17	20		
F'=0				16			

(a) Table 13. The transitions labels in F m_F basis.

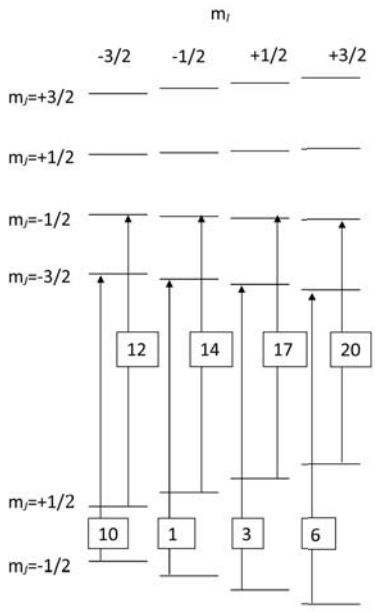

(b) Diagram 12. The transitions labels in m_I m_J basis.

The transitions labels for ^{41}K D_2 line for σ^--polarized exciting radiation in different basis. The labels correspond to the labels on figure.

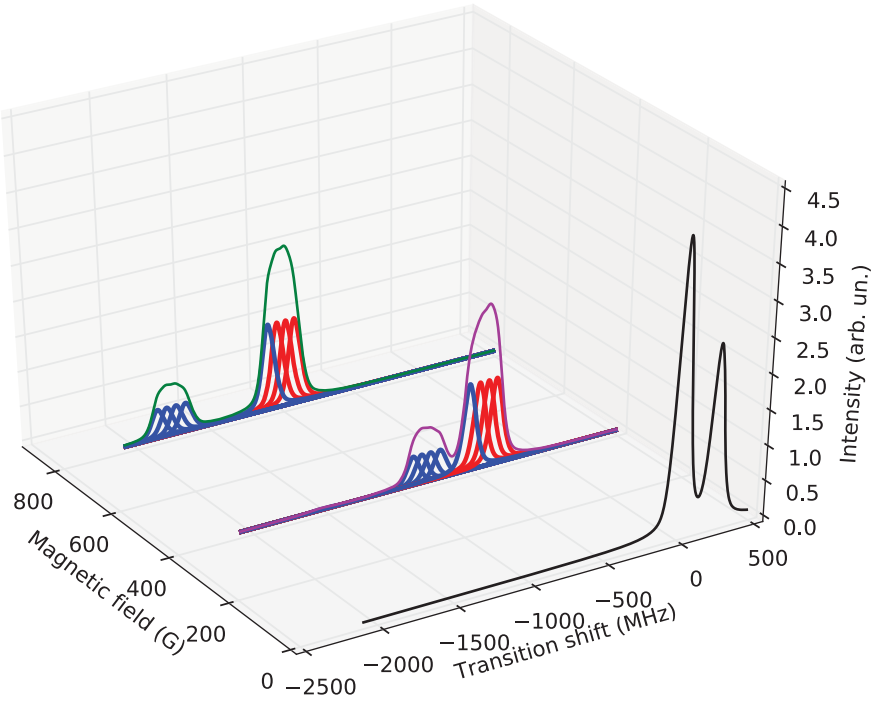

Figure 2.24: ^{41}K 3D spectra of D_2 line for σ^--polarized exciting radiation at 0 G, 400 G and 800 G magnetic fields. The zero is $F_g = 2 \rightarrow F_e = 1$.

2.4 Summary

We have calculated theoretical curves of dependence of individual atomic transitions probabilities and frequency shifts on external magnetic fields. In the range of $0-10$ kG magnetic fields, D_1 and D_2 lines of ^{39}K and ^{41}K have been studied theoretically.

The ^{40}K isotope calculations are not presented here. The point is that its natural density is $\sim 0.01\%$. Besides, its nuclear quantum number is $I = 4$ leading to 72 levels for the $S_{1/2}, P_{1/2}, P_{3/2}$ states. As a result, the obtained figures contain huge number of transitions and corresponding transition intensities and their presentation is not acceptable to the eye. However, in case of necessity for someone, these figures will be presented in www.arXiv.org later.

Chapter 3

SPECTROSCOPY OF ALKALI ATOMS IN STRONG MAGNETIC FIELDS, HYPERFINE PASCHEN-BACK REGIME

Rubidium, Cesium and Potassium atoms are widely used in laser atomic physics due to their strong atomic transitions, which wavelengths are located in the near infrared region and there are available diode lasers with good parameters in this domain. Rb and Cs atoms are widely used in laser cooling experiments, information storage, spectroscopy, magnetometry etc. In an external magnetic fields atomic energy levels split into Zeeman sub-levels. Shift of the frequency of atomic transitions deviate from the linear behavior in a quite moderate magnetic field. Also, probability of atomic transitions usually changes significantly as a function of an external magnetic B-field value. That's why detailed knowledge of the behavior of Rb, Cs and K atomic transitions, particularly, in an external magnetic field is of high importance.

The splitting of atomic levels in weak magnetic fields is described by the total angular momentum $F = J + I$ of the atom and its projections m_F, where $J = L + S$ is the total angular momentum of electrons and I is the nuclear spin. In the hyperfine Paschen-Back regime, J and I become decoupled and the splitting of the atomic levels is described by the

projections m_J and m_I. For alkali metals, the hyperfine Paschen-Back regime takes place in the fields $B \gg B_0 = A_{hfs}/\mu_B$, where A_{hfs} is the ground-state hyperfine coupling coefficient and μ_B is the Bohr magneton. For ^{133}Cs, ^{87}Rb and ^{85}Rb atoms $B_0 \sim 1.7$ kG, 2 kG and 0.7 kG, respectively. It is worth to note that ^{39}K has the smallest $B_0 \simeq 0.165$ kG caused by the smallest hyperfine splitting $\Delta \simeq 462$ MHz of the ground level $4S_{1/2}$ (note that $A_{hfs} = \Delta/(I + 1/2)$). Thus, one expects to obtain complete J and I decoupling of ^{39}K at relatively low magnetic fields $B \gg 165$ G.

The manifestations of the hyperfine Paschen-Back regime, particularly, are as follows:

i) Strong reduction of the number of atomic transitions (compared with that at low magnetic fields) to a fixed number which is easy to determine from the diagram on the basis of m_J and m_I quantum numbers;

ii) The fixed frequency slope inside the group of transitions;

iii) The transitions probabilities tend to the same value inside the group;

iv) The energy of the ground and upper levels, as well as the slopes and the frequency intervals between the transitions can be calculated from the analytic expression 3.1.

3.1 Complete hyperfine Paschen-Back regime at relatively small magnetic fields realized in Potassium nano-cell

The atomic spectroscopy based on the NC filled with Rb or Cs atomic vapors, with a thickness of the vapor column L which is of the order of the optical radiation wavelength has been found to be very efficient to study the optical atomic transitions in external magnetic fields [88 - 95]. There are three interconnected effects: splitting of the atomic energy levels to Zeeman sublevels and shifting of frequencies (deviating from the linear dependence observed in quite moderate magnetic fields), and significant change in atomic transitions probabilities as a function of the B-field. These studies benefit from the following features of NC:

i) sub-Doppler spectral resolution for atomic vapor thickness $L = \lambda/2$ and $L = \lambda$ (λ-

being the resonant wavelength of Potassium $D_{1,2}$, Rubidium $D_{1,2}$ or Cesium $D_{1,2}$ lines) needed to resolve a huge number of Zeeman transition components in transmission or fluorescence spectra;

ii) possibility to apply a strong magnetic field using permanent magnets in spite of a strong inhomogeneity of the B field (in our case it can reach 150 G/mm). Note that the variation of the B field inside the atomic vapor is negligible as the vapor column thickness is small. Potassium vapor in magnetic fields was studied in [65] using a few centimeter-long cell and saturation absorption technique. However, due to the presence of strong cross-over resonances in the absorption spectrum, the technique is useful only for $B < 100$ G. Here we present the first experimental studies of Potassium (^{39}K) vapor confined in NC and under the influence of relatively low magnetic fields ($B < 2$ kG). The NC with $L = \lambda/2$ and $L = \lambda$ are used in the case of excitation with σ^+ and linear (π) polarized laser radiations.

3.1.1 Potassium nano-cell

A photograph of the Potassium nano-cell with a tapered gap is shown in Fig. 3.1. The windows of the NC were constructed with well-polished crystalline sapphire with the c axis perpendicular to the window surface to minimize birefringence. The regions with the thickness $L = \lambda/2 = 385$ nm and $L = \lambda = 770$ nm are marked by ovals in Fig. 3.1. A sapphire side-arm (SA) filled with metallic K is seen at the bottom of Fig. 3.1. The side-arm was heated to $150 - 160$ °C (the temperature on the windows was by 20 °C higher in order to prevent vapor condensation) providing the density of atoms $N = (5 - 8)10^{12}$ at/cm^3. The NC can operate up to 500 °C.

The hyperfine energy levels (partially) diagram of the D_1 line of ^{39}K is shown in Fig. 3.2.

3.1.2 Experimental setup

A sketch of the experimental setup is shown in Fig. 3.3. The linearly polarized beam of an extended cavity diode laser ($\Delta\nu_L < 1$ MHz), resonant with a ^{39}K D_1 line after passing through a Faraday isolator (FI) was focused onto a 0.5 mm diameter spot on the Potassium nano-cell orthogonally to the cell window. A Polarization Beam Splitter (PBS) was used to purify the initial linear polarization of the laser; a $\lambda/4$ plate (1) was used to produce a σ^+ circular

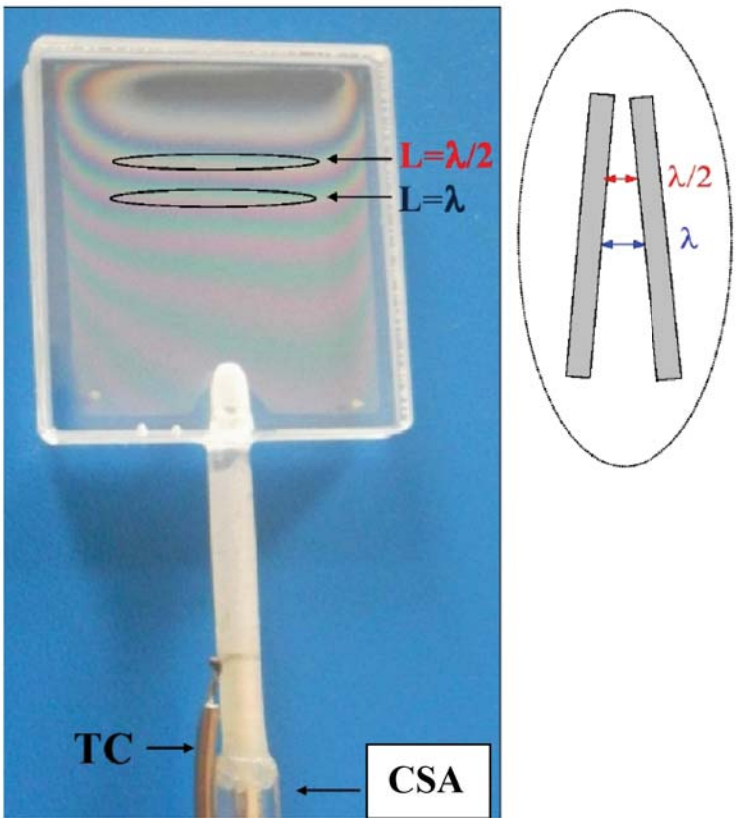

Figure 3.1: Photograph of the nano-cell filled with ^{39}K. The thickness of the wedge-shaped gap is 50 nm $< L <$ 1500 nm. One can see the interference fringes formed owing to reflection of light from the inner surfaces of the cell windows. The regions $L = \lambda/2 = 385$ nm and $L = \lambda = 770$ nm are marked by ovals. The wedge-shaped gap between the inner surfaces of the windows is shown schematically at right.

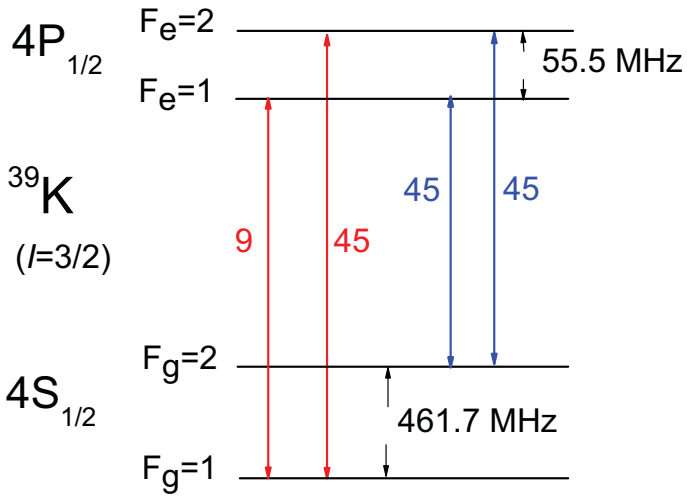

Figure 3.2: The hyperfine energy levels diagram of the D_1 line of ^{39}K. Only the levels which have been used in the experiment are shown. 9, 45, 45, 45 numbers are transitions relative probabilities.

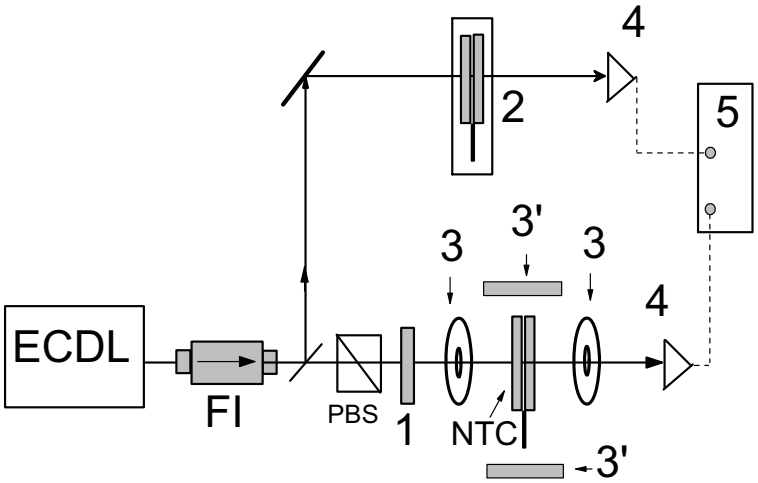

Figure 3.3: Sketch of the experimental setup. ECDL: diode laser; FI: Faraday isolator; 1: $\pi/4$ plate; NC-main Potassium nano-cell with the thickness $L = \lambda/2$ or $L = \lambda$ in the oven; PBS: polarizing beam splitter; 2: auxiliary Potassium nano-cell; 3: permanent magnets. In the case of σ^+ polarized laser radiation, the B-field is directed along the laser propagation direction k, (magnets 3). In the case of π polarized laser radiation, the B-field is directed along the laser electric field E (magnets 3); 4: photodetectors; 5: oscilloscope

polarization. In the experiments the thicknesses of the vapor column $L = \lambda$ and $L = \lambda/2$ are used. The transmission signal was detected by a photodiode (4) and was recorded by a Tektronix TDS 2014B four-channel storage oscilloscope (5). To record the transmission spectra, the laser radiation was linearly scanned within up to a ~ 5 GHz spectral region covering the studied group of transitions. About 30% of the laser power was branched to the reference unit with an auxiliary Potassium nano-cell (2). The absorption spectrum of the latter with thicknesses $L = \lambda/2$ or $L = \lambda$ was used as frequency reference.

3.1.3 Potassium experiments

For our purpose a one-dimensional nano-metric-thin cell filled with natural potassium (93.25% ^{39}K, 0.01% ^{40}K and 6.7% ^{41}K) has been built (for the first time) and used for the experiment. The design of the NC is similar to that of the extremely thin cell described earlier [95] (the details of nano-cell design can be found in Chapter I). The nano-cell allows one to exploit a variable vapor column thickness L in the range of $50 - 1500$ nm. It is demonstrated that for K vapor the key parameter determining the spectral width and the shape of the absorption

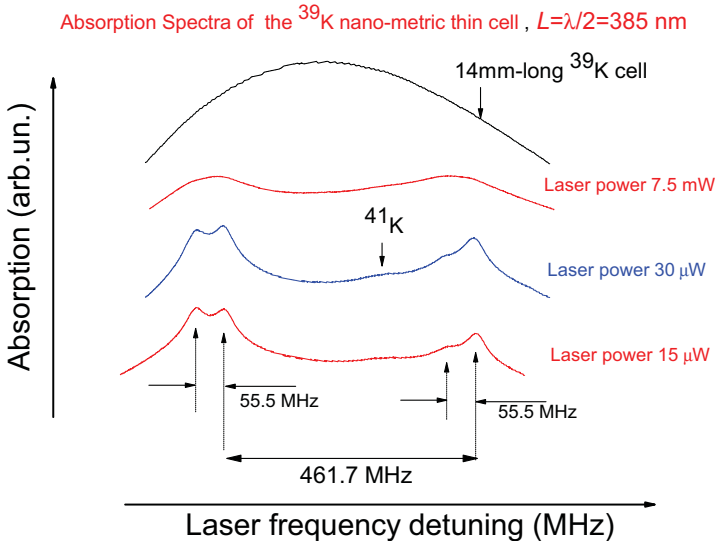

Figure 3.4: Absorption spectra of the D_1 line of ^{39}K. The top spectrum is the reference (yielded by 14 mm long cell). The lower spectra are obtained by $\lambda/2$. In the blue line ^{41}K is visible (smallest peak).

line in the NC is the ratio L/λ, with $\lambda = 770$ nm being the wavelength of the laser radiation resonant with the atomic transition of D_1 line (as it was earlier demonstrated for the NC filled with Cs or Rb). In particular, it was shown that the spectral width of the resonant absorption reaches its minimum value at $L = (2n+1)\lambda/2$ (n is an integer); this effect is the Dicke-type coherent narrowing [43, 44, 64]. It is also demonstrated that for $L = n\lambda$ the spectral width of the resonant absorption reaches its maximum value, close to the Doppler width (> 0.9 GHz).

3.1.4 $L = \lambda/2 = 385$ nm method

Absorption spectra of the atomic vapor of ^{39}K which is enclosed in the nano-cell with the thickness $L = \lambda/2 = 385$ nm for the different powers of laser radiation 7.5 mW, 30 μW and 15 μW are presented in Fig. 3.4 (it is called $\lambda/2$-method). The side-arm of the nano-cell is heated up to $150-160^\circ$ C. The upper curve is the absorption spectrum of 14 mm-long cell filled with Potassium, which is heated up to 50° C. As it is seen due to the sub-Doppler narrowing of the absorption of the atomic transitions, all four atomic transitions $F_g = 1,2 \rightarrow F_e = 1,2$ are well resolved, meanwhile for the absorption spectrum of 14 mm-long cell filled with K the all four atomic transitions are masked by the Doppler profile of ~ 900 MHz. As we see with the increase of the laser power the line-width increases, which is caused by well-known power-broadening effect. That's why the laser power must be adjusted in order to get narrow-band

absorption lines. In the case of $\lambda/2$-method full width at half maximum (FWHM) is of order 110-120 MHz. For the low laser power $P = 2$ μW the experimental (the line-width is the narrowest) and theoretical absorption spectra of K atomic vapor contained in the NC with $L = \lambda/2 = 385$ nm are shown in Fig. 3.5 (a) and (b). The large width of the spectrum at the base of the line profile is caused by huge Doppler broadening > 0.9 GHz at 170° C at the NC windows.

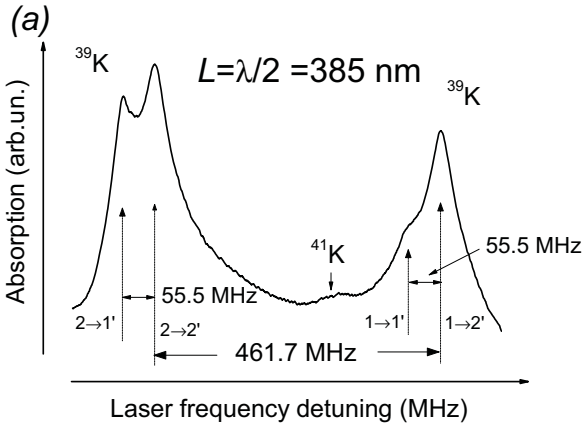

(a) Experimental absorption spectrum of ^{39}K atomic vapor contained in the NC with $L = 385$ nm for the laser power $P = 2$ μW, the side-arm temperature is 150°C, a small absorption of the isotope ^{41}K is also seen.

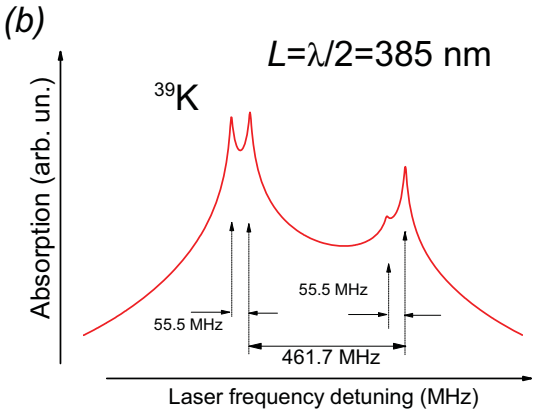

(b) Theoretical absorption spectrum with the parameters: thermal velocity $V_{th} = 450$ m/s, the value of the laser Rabi frequency is $\Omega/2\pi = 0.06\gamma_N$ ($\gamma_N \simeq 6$ MHz).

Figure 3.5: Experimental and theoretical absorption spectra of ^{39}K atomic vapor using NC with the thickness of $L = 385$ nm.

3.1.5 $L = \lambda = 770$ nm method

In this case, spectrally narrow velocity selective optical pumping (VSOP) resonances located exactly at the positions of atomic transitions spectrum appear in the transmission spectrum of the NC with thickness $L = \lambda$ shown in Fig. 3.6. The VSOP parameters are shown to be immune against 10% thickness deviation from $L = \lambda$, which makes the λ-method feasible. Laser power is ~ 15 μW (for a lower power the VSOP line-width is less than 30 MHz, but is noisier). The insets in dashed rectangles show the results of fitting by Lorentzian profiles. Note that the ratio of the VSOPs amplitudes $F_g = 1, 2 \rightarrow F_e = 1, 2$ coincides with that deduced from the values given in Fig. 3.2 which means linear dependence on laser power. In a magnetic field, the VSOPs are split into many components. The amplitude and frequency positions of VSOPs depend on the B-field, which makes it convenient to study each individual transition separately.

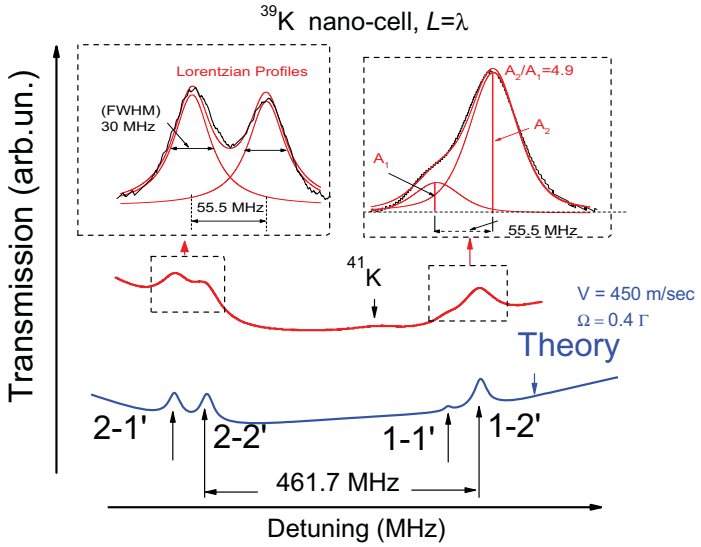

Figure 3.6: The upper curve is the experimental transmission spectrum of ^{39}K atomic vapor contained in the NC with $L = 770$ nm for the laser power $P = 15$ μW, the side-arm temperature is 150°C; in the spectrum appear spectrally narrow velocity selective optical pumping (VSOP) resonances located exactly at the positions of atomic transitions. The inset shows the results of fitting by Lorentzian profiles; the ratio of the VSOPs amplitudes coincides with that deduced from the values given in Fig. 3.2. The lower curve is the theoretical spectrum [95] with the parameters: thermal velocity $V_{th} = 450$ m/s, the value of the laser Rabi frequency is $\Omega/2\pi = 0.06\gamma_N$ ($\gamma_N \simeq 6$ MHz).

3.1.6 Magnetometry with $\lambda/2$- and λ-methods, σ^+ polarized laser excitation

The assembly of an oven with NC inside was placed between the permanent ring magnets. The magnetic field B was directed along the laser radiation propagation direction k. An extremely small thickness of the NC is advantageous for the application of strong magnetic fields with the use of permanent magnets (having a 2 mm diameter hole for the laser beam passage). Such magnets are unusable for centimeter-long cells because of the strong inhomogeneity of the magnetic field, while in the NC, the variation of the B-field inside the atomic vapor column is by several orders less than the applied B value. The B-field strength was measured by a calibrated Hall gauge with an absolute imprecision less than 30 G throughout the applied B-field range. The absorption spectra of ^{39}K vapor contained in NC with $L = \lambda/2$ (for σ^+ polarized excitation) versus magnetic field is shown in Fig. 3.7.

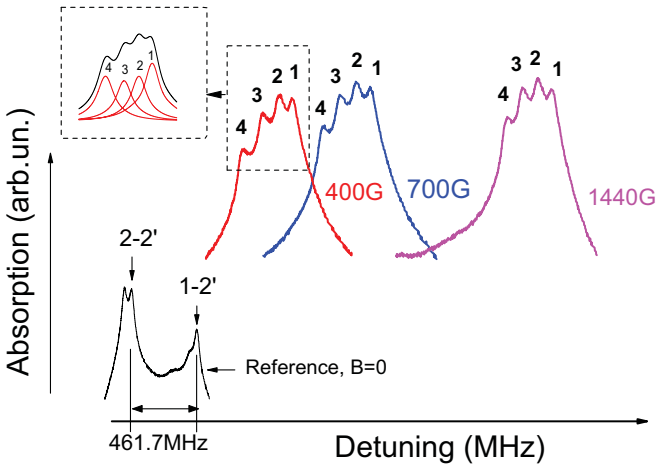

Figure 3.7: Absorption spectrum of ^{39}K vapor contained in the NC with $L = \lambda/2$ for $B =$ 400 G, 700 G and 1440 G; σ^+ polarized excitation. The bottom curve is the reference showing the positions of ^{39}K transitions for $B = 0$ G. The inset shows the results of fitting by four "pseudo-Voigt" functions (note that the amplitude of the transition labeled 4 is larger than that of 3). The absolute value of the peak absorption of transition 1 is $\sim 0.3\%$.

The bottom curve is the reference one. Four atomic transitions are well observable. Four atomic transitions for the hyperfine Paschen-Back regime are predicted by the diagram presented in Fig. 3.9. Note that the frequency separation between the two well resolved VSOP labeled 1 and 2 is about 90 MHz, which is more than 10 times less than the Doppler line-width.

The transmission spectra of ^{39}K vapor contained in the NC with $L = \lambda$ (for σ^+ polarized laser excitation) versus magnetic field is shown in Fig. 3.8 (the bottom curve is the reference one). Four atomic transitions labeled 1-4 are well observable. Also, the VSOPs have the same amplitudes which is an additional evidence of HPB regime.

Let us briefly stress the benefits of $\lambda/2$- and λ-methods. The $\lambda/2$-method requires less laser intensity and in case of small absorption the peak absorption A is proportional to σNL, where σ is the absorption cross section proportional to d^2 (with d being the dipole momentum). Thus, by direct comparison of A_i (A_i is the peak amplitudes of the absorption of the i-th transition), it is straightforward to estimate the relative probabilities (i.e. line intensities). On the other hand, the λ-method provides a fivefold better spectral resolution. Thus, the methods can be considered as complementary depending on particular requirements. Moreover, it is easy to switch from the thickness $\lambda/2$ to the thickness λ just by vertical translation of the NC. Note, that in the case where there is a big frequency separation between the transitions (as it is for the ^{87}Rb isotope) also a 1 mm long cell can be used [129 - 131]. Theoretical simulations for the B-field dependences of the atomic transition frequency shifts and relative transition probabilities for $Fg = 1, 2 \rightarrow F_e = 1, 2$ transitions of the ^{39}K D_1 line were based on the calculation of the eigenvalues and eigenvectors of the Hamiltonian matrix versus magnetic field for the full hyperfine structure manifold [see Chapter II]. Although for the ^{39}K atom D_1 line the Rabi-Breit formula could be also used, however the theoretical model is preferable since it is valid also for ^{39}K atom D_2 line. Note, that in the case of HPB regime the energy of the ground $4S_{1/2}$ and upper $4P_{1/2}$ levels for the ^{39}K D_1 line is given by the formula (3.1).

$$E_{|Jm_JIm_I\rangle} \simeq A_{hfs} m_J m_I + B_{hfs} \frac{9(m_I m_J)^2 - 3J(J+1)m_I^2 - 3I(I+1)m_J^2 + I(I+1)J(J+1)}{4J(2J-1)I(2I-1)} + \mu_B(g_J m_J + g_I m_I)B_z \tag{3.1}$$

The values for the Landé factors g_J, g_I and the hyperfine constants A_{hfs} are given in [132]. The dependence of the frequency shifts on the magnetic field (relative to the position of the

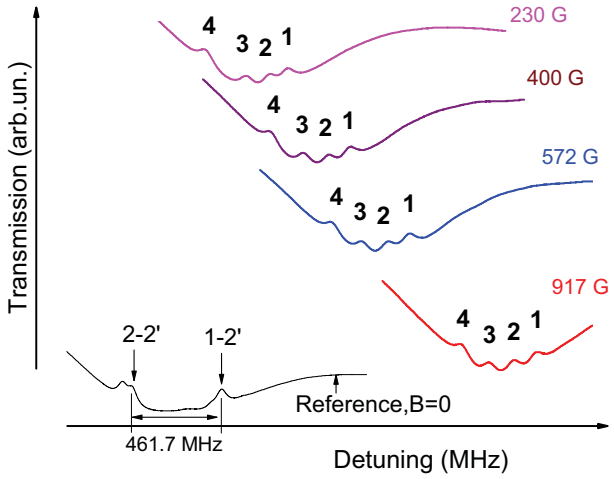

Figure 3.8: Transmission spectrum of ^{39}K atomic vapor contained in the NC with $L = \lambda = 770$ nm for $B = 230$ G, 400 G, 572 G and 917 G and σ^+ polarized laser excitation. The bottom curve is the reference showing the positions of ^{39}K transitions for $B = 0$ G.

$F_g = 2 \rightarrow F_e = 2$ transition at $B = 0$) is shown in Fig. 3.10, where the red lines are obtained by exact numerical calculation, while the black lines are plotted according to the formula 3.1; the black squares are the experimental results. The inaccuracy does not exceed 2%. A good agreement of theory and experiment is observed.

In Fig. 3.11 it is presented the residual difference between numerical calculations (Fig. 3.10 red lines) and with the formula 3.1 (Fig. 3.10 black lines). It is remarkable that at a relatively low magnetic field $\sim$ 1000 G formula 3.1 describes the transition frequency values with an inaccuracy of $\leq 1\%$. Note that at $B = 1.8$ kG the difference is $\leq 0.3\%$ which could be considered as practically the full HPB regime.

The theoretical values of the ^{39}K atomic transition probabilities (intensities) as a function of the B-field is shown in Fig. 2.5 (theory, Chapter 2). As seen, the intensities of transitions $1, 2, 3$ and 4 (which are labeled as $5, 4, 2$ and 7 respectively in Fig. 2.5) at $B \geq 1$ kG tend to the same asymptotic value (HPB regime), which coincides with the experiment, while at $B < 400$ G, the intensity of the transition labeled 4 (7) (Fig. 3.7) is larger than those of the 3 (2) and 2 (4) ones - this also coincides with the experiment.

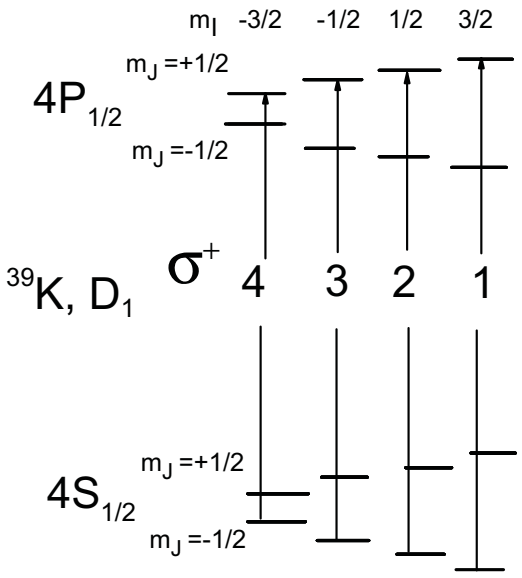

Figure 3.9: Diagram of ^{39}K D_1 line transitions in hyperfine Paschen-Back regime for σ^+ polarized laser excitation. The selection rules are $\Delta m_J = 1$; $\Delta m_I = 0$. Four atomic transitions labeled 1-4 are existing, which coincides with the experimental results shown in Fig. 3.7 and Fig. 3.8

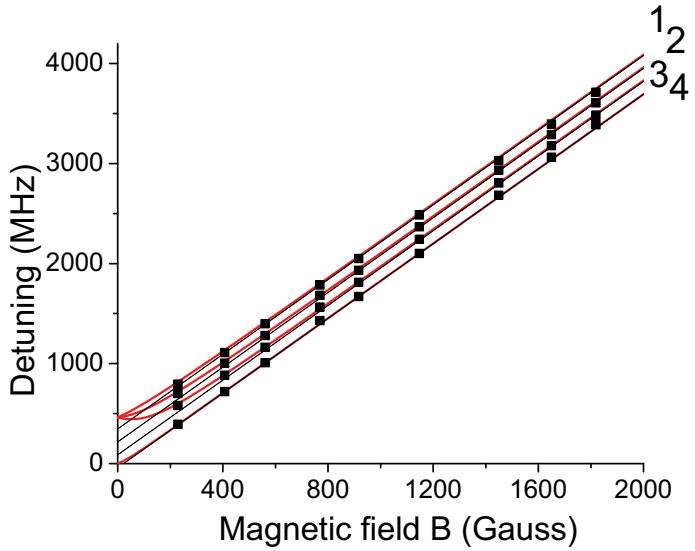

Figure 3.10: B-field dependence of the frequency shifts for transitions 1 - 4 of the ^{39}K D_1 line in the case of σ^+ polarized laser excitation. Red lines are given by exact numerical calculations, black solid lines by formula (3.1), black squares shows the experimental results. The inaccuracy is $\sim 2\%$.

3.1.7 Magnetometry with λ-method, π polarized laser excitation

For this case the B-field is directed along the laser electric field E (magnets numbered 3' are used and $\lambda/4$ plate is removed, see Fig. 3.3). Fig. 3.12 shows the hyperfine splitting energy levels diagram of the D_1 line of ^{39}K atoms in a magnetic field ($B < B_0$) and 14 possible

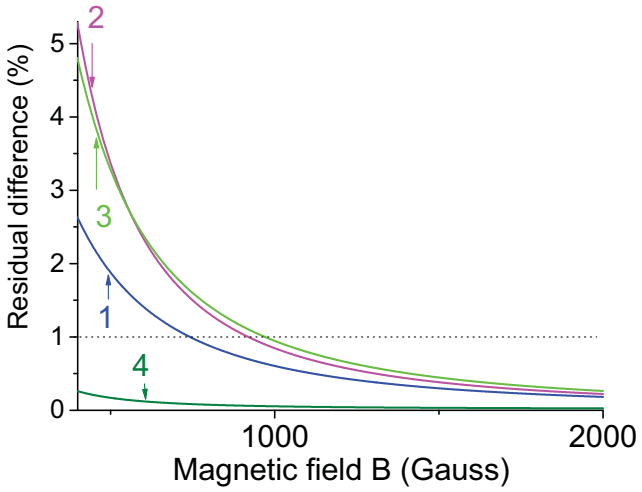

Figure 3.11: The residual difference between numerical calculation and formula (3.1) for curves 1 - 4. As it is seen, at a relatively low magnetic fields $\sim$ 1000 G the formula (3.1) describes the transition frequency values with an inaccuracy of $\leq 1\%$. Note that at $B = 1.8$ kG the difference is $\leq 0.3\%$ which could be considered as practically the full HPB regime.

atomic Zeeman transitions for π polarized excitation. Also, two forbidden at $B = 0$ atomic transitions [87] are shown by dashed lines that we call "initially forbidden further allowed" (IFFA) transitions. Fig. 3.13 presents the diagram of eight remaining transitions. Note, that the probabilities rise with the B-field increase.

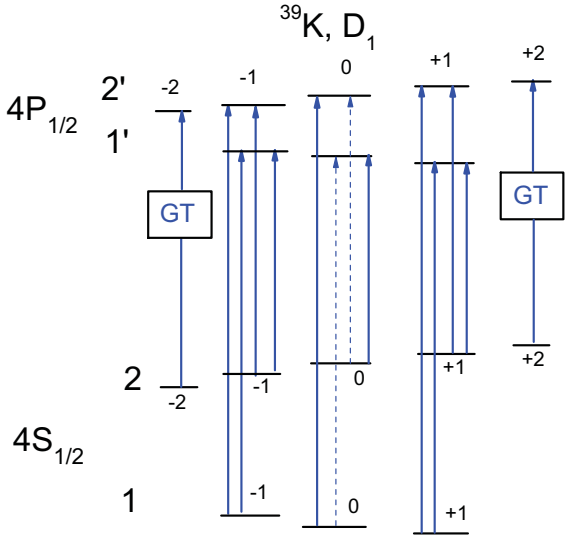

Figure 3.12: Diagram of the hfs energy levels of D_1 line of ^{39}K in a magnetic field (in F, m_F basis) and possible Zeeman transitions for π polarized excitation are shown. The selection rules are $\Delta F = 0, \pm 1$; $\Delta m_F = 0$. "Guiding transitions" (GT) are labeled by rectangles; two "Initially forbidden further allowed transitions" IFFAT are indicated by dashed lines.

Note, that the necessary conditions for a modification of the probability are the following

[18, 19]: the perturbation induced by the B-field couples only sublevels with $m_F - m'_F = 0$ which satisfy the selection rules $\Delta L = 0, \Delta J = 0, \Delta F = 1$, and modification of the probability is possible only for the transitions between ground and excited sublevels when at least one of them is coupled with another transition's sublevel according to the selection rules. As seen from Fig. 3.12, sublevels, which could be mixed with the four side atomic states of ^{39}K $F_g = 2, m_F = -2, F_g = 2, m_F = 2, F_e = 2, m'_F = -2$ and $F_e = 2, m'_F = 2$, according to the selection rules are absent. Thus, the probabilities of these two transitions, $F_g = 2, m_F = -2 \rightarrow F_e = 2, m'_F = -2$ and $F_g = 2, m_F = 2 \rightarrow F_e = 2, m'_F = 2$, remain the same in the whole range of applied B-fields, while the probabilities of other transitions differ significantly at low fields, but tend to the same value within the group at $B \gg B_0$. It is remarkable that the probabilities of all the other atomic transitions tend to that of these two side atomic transitions (this is confirmed by the numerical calculations). This is the reason why we call them Guiding Transitions.

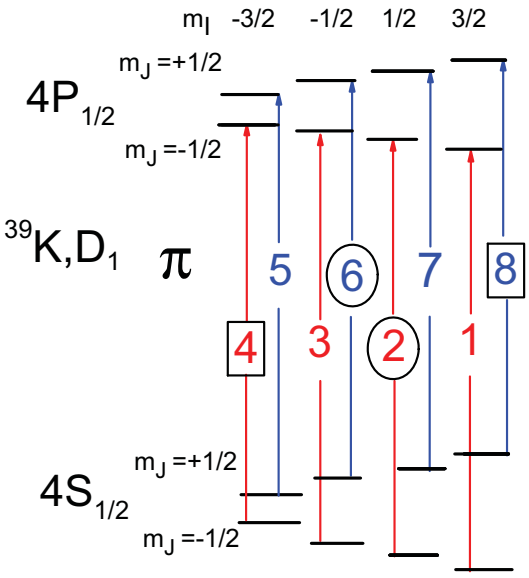

Figure 3.13: Diagram of the ^{39}K D_1 line transitions in the HPB regime (in m_I, m_J basis) for π polarized laser excitation. The selection rules are: $\Delta m_J = 0$; $\Delta m_I = 0$. Two IFFATs are labeled by ovals. Eight atomic transitions labeled 1-8 are existing, which coincides with the experimental results shown in Fig. 3.14

In Fig. 3.14 the transmission spectra of π polarized excitation of the potassium NC, $L = \lambda$ for $B = 345, 420, 470$ and 645 G are shown. GT and IFFA transitions are labeled by rectangles and ovals, respectively (as seen IFFA transitions undergo strong modification under the influence of the B-field).

The B-field dependence of the frequency shifts for transitions $1 - 8$ for π polarized laser

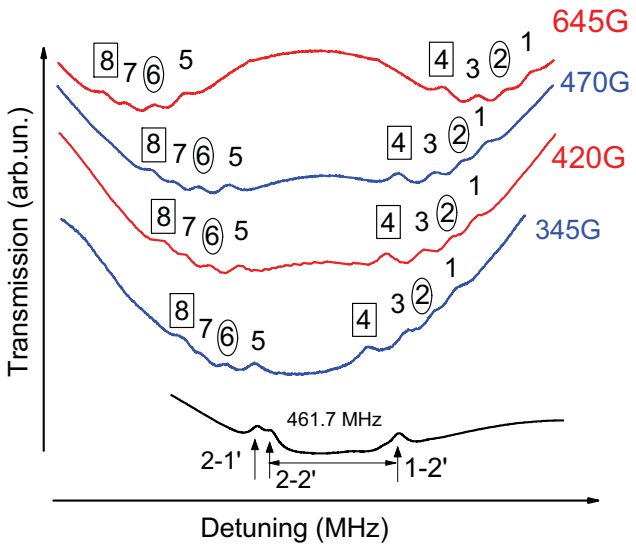

Figure 3.14: Transmission spectrum of the NC with ^{39}K for $L = \lambda$ for $B = 345$ G, 420 G, 470 G and 645 G; π polarized laser excitation is used. GTs and IFFATs are labeled by rectangles and ovals, respectively. The bottom curve is the reference

radiation is shown in Fig. 3.15. Guiding Atomic Transitions and IFFA transitions are labeled by rectangles and ovals, respectively. We see that transitions $1-8$ are collected in two groups of four atomic transitions in each. Theoretically slope (s) is given by

$$s \simeq [g_J(P_{3/2})m_J - g_J(S_{1/2})m_J]\mu_B/B. \tag{3.2}$$

The value is approximated as we ignore the $g_I m_I$ contribution, because $g_I \ll g_J$. Note that the frequency slope of the four transitions inside the group asymptotically tends to the slope of Guiding Atomic Transition. It is easy to show that they are equal to $s = 0.94$ MHz/G and $s = -0.94$ MHz/G for groups $1-4$ and $5-8$, respectively. Solid lines are the calculated curves, while the black squares shows the experimental results. The inaccuracy is $\sim 2\%$. As it is seen there is a good agreement between the theory and the experiment.

In Fig. 3.16(a) the initial quantum numbers F, m_F for the ground and the upper levels for the atomic transitions 1-3 and $1' - 3'$ are presented (shown in Fig. 3.15). In Fig. 3.16(b) the initial quantum numbers F, m_F for the ground and the upper levels for the atomic transitions $4 - 8$ and $4' - 6'$ are presented (shown in Fig. 3.15).

Figure 2.1 (theory, Chapter II) presented the intensity and the frequency shifts of the ^{39}K

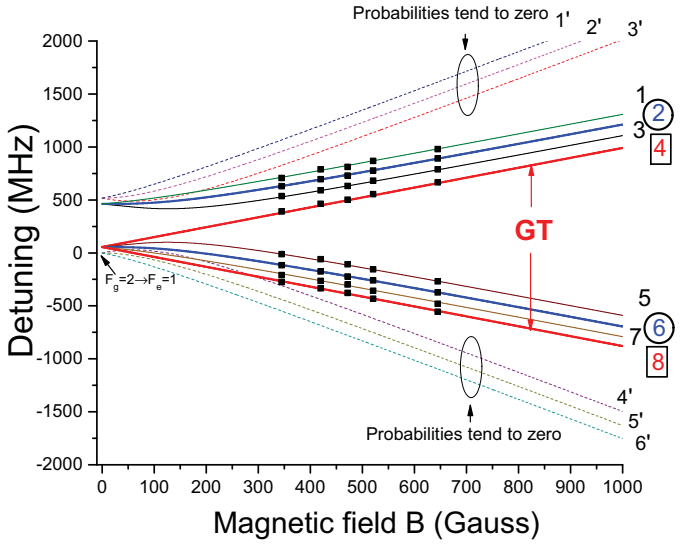

Figure 3.15: The B-field dependence of the frequency shifts for transitions 1-8 for π polarized laser radiation. GTs and IFFATs are labeled by rectangles and ovals, respectively. There are 1-8 transitions which are collected in two groups of four atomic transitions in each. The probabilities of $1'$-$3'$ and $4'$-$6'$ tend to zero. Solid lines are the calculated curves. Black squares show the experimental results. The inaccuracy is $\sim 2\%$.

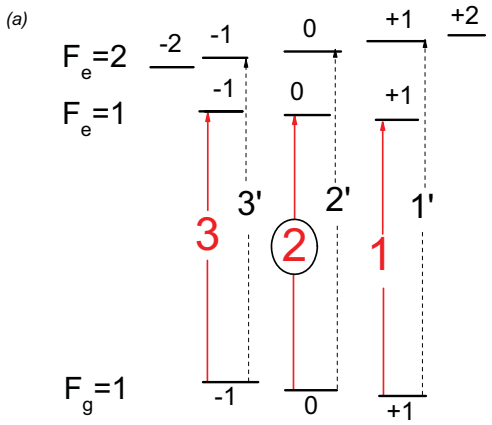

(a) The diagram of the transitions from $F_g = 1$: 1-3 and $1'$-$3'$.

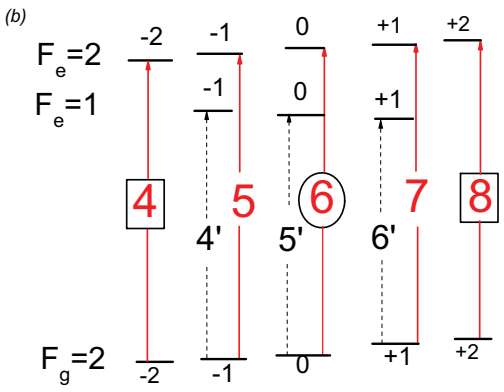

(b) The diagram of the transitions from $F_g = 2$: 4-8 and $4'$-$6'$.

Figure 3.16: The diagrams of the transitions shown in Fig. 3.15 from the different ground levels.

transitions as a function of the B-field for π polarized laser excitation. As seen for magnetic fields $B \gg B_0$ only transitions $1-8$ remain and the probabilities at $B \gg B_0$ tend asymptotically to the same value as it is for the Guiding Atomic Transition (by module it is 4.66×10^{-18} ESU). The inset shows the diagram of the KD_1 line transitions in the HPB regime with Guiding Atomic Transition and "initially forbidden further allowed" transitions which are marked.

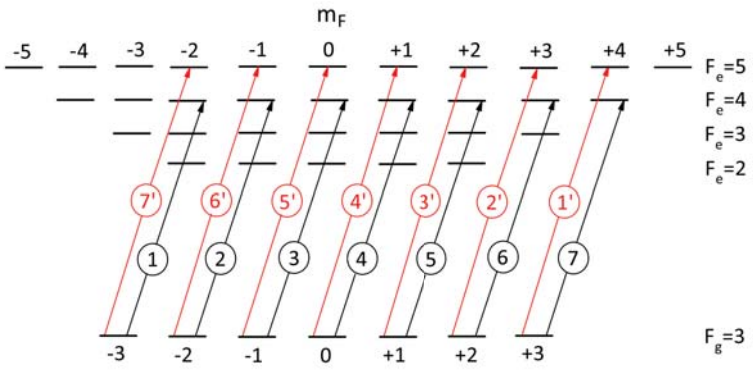

Figure 3.17: The diagram of the relevant transitions between Zeeman sub-levels of ground ($F_g = 3$) and excited ($F_e = 4, 5$) states for D_2 line of ^{133}Cs (nuclear spin $I = 7/2$) with σ^+ polarized laser excitation. Labeling of transitions is given in circles.

3.2 ^{133}Cs atoms in magnetic field

In this Paragraph we present the results of experimental and theoretical studies of giant transition probability modification for Cs D_2 line $6S_{1/2}, F_g = 3 \rightarrow 6P_{3/2}, F_e = 5$ transitions ($\lambda = 852$ nm) induced by a magnetic field varied in a wide range up to 3.5 kG. These transitions are forbidden at zero magnetic fields according to the selection rule $\Delta F = 0, \pm 1$ for the total angular momentum F of atom. This means that neither an absorption nor a fluorescence can be detected in the same conditions (as it is for other transitions $F_g = 3 \rightarrow F_e = 2, 3, 4$ or $F_g = 4 \rightarrow F_e = 3, 4, 5$) when a laser frequency is in resonance with $F_g = 3 \rightarrow F_e = 5$ transitions. To the best of our knowledge, there are only 3 articles where such type of transitions have been studied quantitatively [81, 87, 137]. Diagram of the relevant transitions between Zeeman sub-levels of ground ($F_g = 3$) and excited ($F_e = 4, 5$) states for D_2 line of ^{133}Cs. The diagram of relevant σ^+ components ($\Delta m_F = +1$) of CsD_2 line transitions $F_g = 3 \rightarrow F_e = 4$ labeled $1 - 7$, and $F_g = 3 \rightarrow F_e = 5$ labeled $1' - 7'$ is shown in Fig. 3.17. The transitions $1' - 7'$ are forbidden for zero magnetic field because of selection rule $\Delta_F = 0, \pm 1$. The transitions $F_g = 3 \rightarrow F_e = 2, 3$ are not shown, since for $B > 500$ G their probabilities strongly reduce, and these transitions are practically not detectable in the absorption spectrum.

As it was demonstrated earlier, strong narrowing in absorption spectrum can be attained with the use of an atomic vapor cell of half-wavelength thickness ($L = \lambda/2$, where λ is the resonant wavelength of laser radiation, $L = 426$ nm for the case of Cs D_2 line). Particularly, the absorption linewidth for Cs D_2 line reduces to $\simeq 100$ MHz (FWHM), as opposed to $\simeq 400$

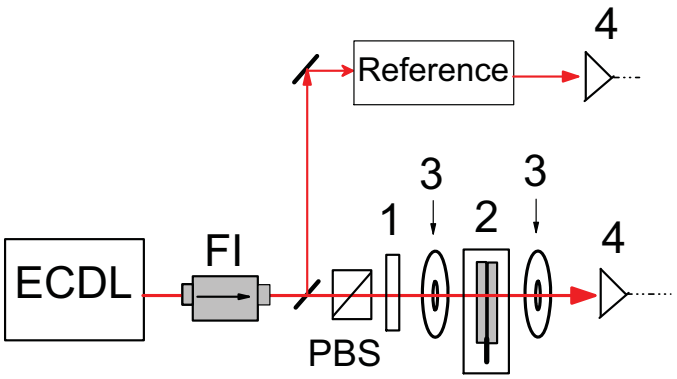

Figure 3.18: Sketch of the experimental setup. ECDL- external cavity diode laser; FI- Faraday isolator; 1- $\lambda/4$ plate; 2- NC in the oven; PBS- polarizing beam splitter; 3- permanent ring magnets; 4- photodetectors; auxiliary Cs nano-cell providing a Reference spectrum for B=0 G.

MHz in an ordinary cell (several centimeters long). Moreover, the absorption lines for $L = \lambda/2$ exhibit Voigt profile with sharp (nearly Gaussian) peak, which allows separation of closely spaced individual transitions and study their transition probabilities in an external magnetic field. In addition, the $\lambda/2$-method is tolerant against 10% deviation of thickness (weak influence on the absorption linewidth). These benefits make it convenient to use $\lambda/2$-method for studies of closely spaced individual atomic transition components in a magnetic field.

3.2.1 Experimental setup

Schematic diagram of the optical part of the experimental setup is shown in Fig. 3.18. A circularly polarized laser radiation beam ($\lambda = 852$ nm, $P_L = 5$ mW, $\Delta\nu_L = 1$ MHz) resonant with CsD_2 line was focused ($\varnothing = 0.5$ mm) onto a Cs nano-cell with a vapor column of thickness $L = \lambda/2$ at normal incidence angle. The 8 mm-thick assembly of the oven with nano-cell inside was placed between two permanent ring magnets with gradually adjustable spacing, providing control of longitudinal B-field.

Extremely small thickness of nano-cell is advantageous for application of very strong magnetic field with the use of permanent magnets otherwise unusable because of strong inhomogeneity in nano-cell, the variation of the B-field inside the cell is several orders less than the

applied B value. To record transmission and fluorescence spectra, the laser radiation was linearly scanned within up to 15 GHz spectral region covering the studied group of transitions. The nonlinearity of the scanned frequency ($< 1\%$ throughout the spectral range) was monitored by simultaneously recorded transmission spectra of a FabryPérot etalon (not shown). About 30% of the pump power was branched to an auxiliary Cs nano-cell with thickness $L = \lambda/2$ providing the reference absorption spectrum for $B = 0$. All the spectra were detected by photodiodes with amplifiers followed by a four channel digital storage oscilloscope Tektronix TDS 2014B.

3.2.2 Giant modification of the $F_g = 3 \rightarrow F_e = 5$ transitions probabilities

A nano-thin cell filled with the Cs has been used in our experiment, which allows obtaining of sub-Doppler spectra, thus resolving a large number of hyperfine and Zeeman transition components. The general design of the Cesium nano-cell is similar to that described in [40, 72] and the photograph with a tapered gap is shown in Fig. 1.3 (Chapter I). The region with the thickness $L = \lambda/2 = 426$ nm which is used in the experiments is marked by the oval in Fig. 1.3. Compact oven has been used to set the needed temperature regime. The temperature was set to 100° C, which corresponds to number density of Cs atoms $N \simeq 10^{13} cm^{-3}$. Adjustment of needed vapor column thickness without variation of thermal conditions was attained by smooth vertical translation of the cell + oven ensemble.

3.2.3 Experimental data

The recorded absorption spectrum of Cs NC with thickness $L = \lambda/2$ for σ^+ laser excitation ($P_L = 10$ μW) and $B = 920$ G is shown in Fig. 3.19. The fourteen above labeled transition components appear with $\simeq$ 100 MHz line-width, thus being completely frequency resolved except for transitions $5, 6$ and $7'$ resolved partially, and $6'$ and 7, which are fully overlapped. The region of these transitions marked by a dashed rectangle is explored in the inset of Fig. 3.19, showing also the result of the fitting of overlapped individual absorption lines. The fitting

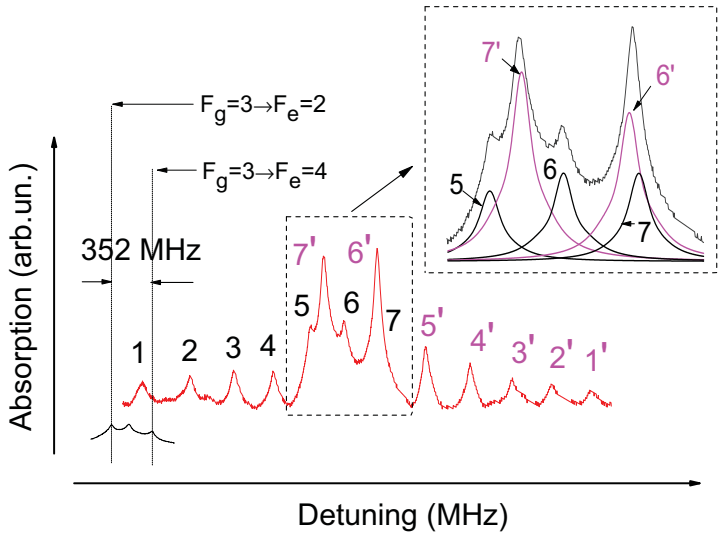

Figure 3.19: Absorption spectrum of Cs nano-cell with $L = \lambda/2$ for $B = 920$ G and σ^+ laser excitation. For labeling of transitions, see Fig. 3.17. The bottom-left curve is fluorescence spectrum of the reference nano-cell showing positions of $6S_{1/2}, F_g = 3 \rightarrow 6P_{3/2}$, F_e=2, 3, 4 transitions for magnetic field $B = 0$ G. Inset shows the result of fitting of the spectrum fragment framed in a dashed rectangle, where atomic transitions are partially overlapped.

is justified thanks to the following advantageous property of the $\lambda/2$-method: for the case of a weak absorption, the absorption coefficient of an individual transition component A is proportional to σNL. Measuring the ratio of A_i values for different individual transitions, it is straightforward to estimate their relative probabilities (line intensities). As is seen from the inset, the amplitudes of $7'$ and $6'$ transitions forbidden at $B = 0$ are the largest among all fourteen transitions.

Further increase of magnetic field to $B = 1450$ G results in better resolution of individual transitions presented in Fig. 3.20. Complete separation of all the fourteen transition components occurs at $B > 3000$ G. The absorption spectrum for $B = 3450$ G and otherwise invariable experimental conditions as in Fig. 3.19 and Fig. 3.20 is presented in Fig. 3.21. Here also the groups of seven transitions $1 - 7$ ($F_g = 3 \rightarrow F_e = 4$) and $1' - 7'$ ($F_g = 3 \rightarrow F_e = 5$) are completely separated within dashed rectangles. In addition, two transition components from the group $F_g = 4 \rightarrow F_e = 5$ appear to be located on the low frequency side of the spectrum.

Noteworthy that the intensity of the transition component labeled $7'$ is the largest among all the twenty five atomic transitions of $F_g = 3 \rightarrow F_e = 2, 3, 4, 5$ group for the magnetic field range 250 G $< B <$ 3200 G, while for $B >$ 3400 G the intensity of transition labeled 7 becomes dominant.

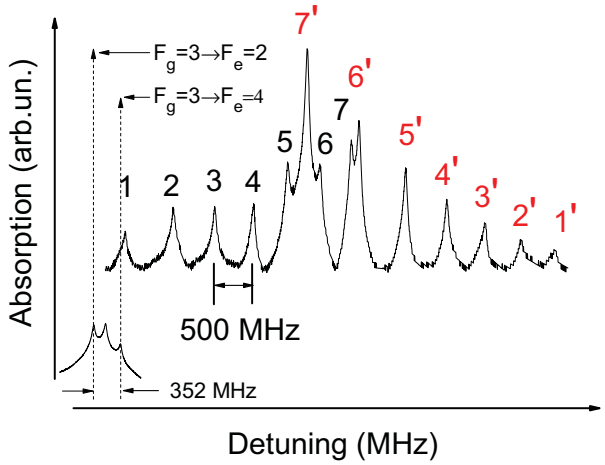

Figure 3.20: Absorption spectrum of Cs NC with $L = \lambda/2$ for $B = 1450$ G and σ^+ laser excitation. For labeling of transitions, see Fig. 3.17. The bottom-left curve is the fluorescence spectrum of the reference nano-cell showing the positions of $6S_{1/2}, F_g = 3 \rightarrow 6P_{3/2}, F_e = 2, 3, 4$ transitions for $B = 0$ G.

The simulations of magnetic sublevel energy and relative transition probabilities for $F_g = 3 \rightarrow F_e = 2, 3, 4, 5$ transitions of CsD_2 line have been made with a theoretical model presented in Chapter II. The dependence of frequency shifts of transitions $1' - 7'$ and $1 - 7$ on magnetic field relative to position of $F_g = 3 \rightarrow F_e = 4$ transition at $B = 0$ for the case of σ^+ excitation is shown in Fig. 3.22. Good agreement of theory and experiment is observed throughout the whole explored range of B-field (up to 3500 G).

The calculated dependence of $1'-7'$ and $1-7$ transition probabilities (absorption amplitudes) versus magnetic field for the case of σ^+ laser excitation are shown in Fig. 3.23.

Since the absolute value of the absorption amplitude A depends on parameters of the experiment (laser intensity, atomic density, etc.), it is expedient to present also the B-field dependence of the ratio of absorption amplitudes A'_i of $1' - 7'$ transitions to absorption amplitude A_7 of the transition 7. The latter is the strongest in the $F_g = 3 \rightarrow F_e = 4$ group; moreover, the absorption amplitude A_7 is nearly constant in a wide range 250 G $< B <$ 4000 G (see Fig.3.23), which makes it convenient to use as a reference. The theoretical ratio A'_i/A_7 versus B-field is plotted in Fig. 3.24 together with experimental results (the ratio is easily measurable). The dashed line marks the unity ratio. As it is seen from Fig. 3.24., $A'_7/A_7 > 1$ holds in a wide range 200 G $< B <$ 3200 G, and the maximum value of the ratio is 2.3.

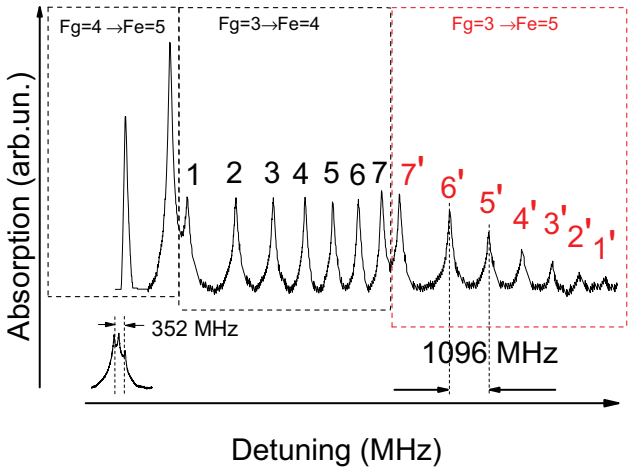

Figure 3.21: Absorption spectrum of Cs nano-cell with $L = \lambda/2$ for magnetic field $B = 3450$ G and σ^+ circular polarized excitation. For labeling of transitions, see Fig. 3.17. The bottom-left curve is the fluorescence spectrum of the reference nano-cell showing the positions of $6S_{1/2}, F_g = 3 \rightarrow 6P_{3/2}, F_e = 2, 3, 4$ transitions for $B = 0$ G. All the individual Zeeman transitions 1-7 and $1'$-$7'$ are completely resolved. Two shifted components of the $6S_{1/2}, F_g = 4 \rightarrow 6P_{3/2}, F_e = 5$ transition appear at the low frequency region.

Thus, the transition $7'$, as well as $6'$ and $5'$, which are forbidden for $B = 0$ undergo giant modification under the influence of magnetic field, becoming predominant over the initially allowed transitions $1-7$. It is worth noting that the maximum value of transition probability for $7'$ transition reaches 76% of the probability for $F_g = 4, m_F = +4 \rightarrow F_e = 5, m_F = +5$ transition, which is the strongest among all the 54 Zeeman transitions of the Cs D_2 line. It is worth to note that the probability of the transition $F_g = 4, m_F = +4 \rightarrow F_e = 5, m_F = +5$ remains the same in the range of magnetic field from zero up to 10 kG. For the explanation see Fig. 3.25. The perturbation induced by the magnetic field couples only sublevels with $\Delta m_F = 0$ which also satisfy the selection rules $\Delta L = 0, \Delta J = 0, \Delta F = \pm 1$ and the modification of the probability is possible only for transition between sublevels at least one of the sublevel is coupled with another transition's sublevel according to these selection rules. As seen from Fig. 3.25 the condition of the probability modification is not fulfilled for $F_g = 4, m_F = +4 \rightarrow F_e = 5, m_F = +5$.

Another group of transitions forbidden at $B = 0, 6S_{1/2}, F_g = 4 \rightarrow 6P_{3/2}, F_e = 2$ (5 transition components for the case of σ^+ excitation), also exhibits modification induced by magnetic field. However, its maximum probability achieved at $B = 60$ G is over 30 times smaller than the maximum probability for $F_g = 3 \rightarrow F_e = 5$.

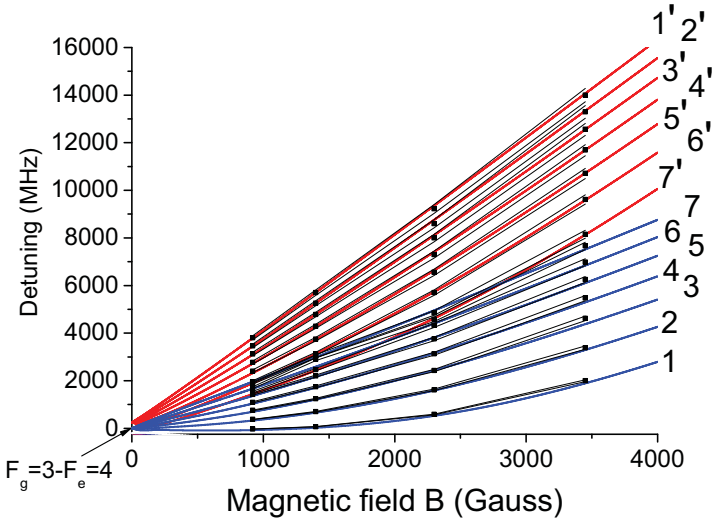

Figure 3.22: Magnetic field dependence of the frequency shift (σ^+ circular polarized laser excitation) for atomic transitions labeled 1′-7′ and 1-7 relative to the position of $F_g = 3 \rightarrow F_e = 4$ transition at magnetic field $B = 0$ G. Black squares: experimental results (inaccuracy $\simeq 2\%$); solid curves: calculated dependence of the frequency shift as a function of magnetic field.

The decoupling of the total angular momentum J and the nuclear momentum I (hyperfine Paschen-Back regime) for Cs atom occurs for $B \gg B_0 = A_{hfs}/\mu_B \simeq 1700$ G, where $A_{hfs} = h \times 2.3$ GHz is the hyperfine constant for $6S_{1/2}$. In this case the splitting of transitions is described by the projections m_J and m_I. At $B > 6000$ G, sixteen transitions are observable in the absorption spectrum: by 8 starting from the ground states $6S_{1/2}, m_J = -1/2$ and $6S_{1/2}, m_J = +1/2$. For $B > 3000$ G and σ^+ excitation, the group of $F_g = 3 \rightarrow F_e = 5$ transitions are always located at the high frequency side of $F_g = 3 \rightarrow F_e = 2, 3, 4$ transitions, with line intensities monotonically reducing and completely vanishing at $B > 9000$ G.

It is interesting to compare the maximum probability of magnetic field-induced Cs $6S_{1/2}$, $F_g = 3 \rightarrow 6P_{3/2}, F_e = 5$ transition normalized to the strongest D_2 transition with the corresponding values for D_2 line transitions forbidden at $B = 0$ for other alkali metal atoms. The theoretical calculations show that for Rb transitions ^{85}Rb $5S_{1/2}, F_g = 2 \rightarrow 5P_{3/2}, F_e = 4$ and ^{87}Rb $5S_{1/2}, F_g = 1 \rightarrow 5P_{3/2}, F_e = 3$, the maximum value is less 1.10 and 1.36 times, correspondingly. Also for $3S_{1/2}, F_g = 1 \rightarrow 3P_{3/2}, F_e = 3$ transitions of Na and $4S_{1/2}, F_g = 1 \rightarrow 4P_{3/2}, F_e = 3$ of K the maximum values are less (1.31 and 1.33 times, correspondingly). Thus, the modification of the probabilities for Cs $F_g = 3 \rightarrow F_e = 5$ transitions is the strongest among all the alkali atoms.

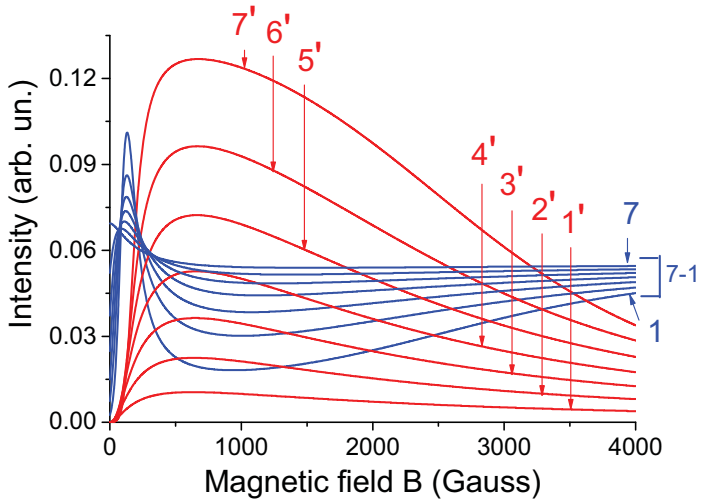

Figure 3.23: Calculated probabilities (absorption amplitudes) of transitions 1′-7′ and 1-7 as a function of magnetic field for σ^+ circular polarized laser excitation.

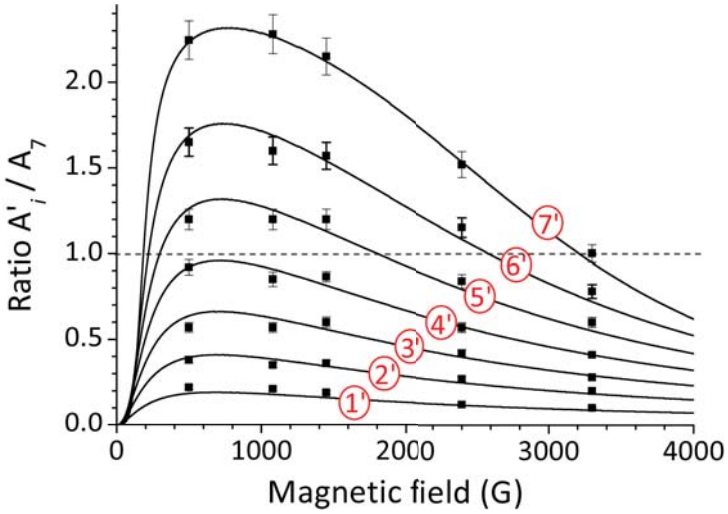

Figure 3.24: Ratio of the absorption amplitudes $A_{i'}$ (transitions 1′-7′) to A_7 as a function of magnetic field B for the case of σ^+ circular polarized laser excitation.

3.3 Rubidium atoms (^{85}Rb and ^{87}Rb) in strong magnetic fields

In this section we present the results of experimental and theoretical studies of the Rb D_2 line atomic transitions, $\lambda = 780$ nm (both for the ^{87}Rb and the ^{85}Rb isotopes) in a wide range of magnetic fields of $B \sim 3$ kG -7 kG, for the case of σ^+ circular and π linear polarized laser excitation, using nano-cells filled with the Rb atomic vapor, with the cell thickness $L = \lambda/2 = 390$ nm.

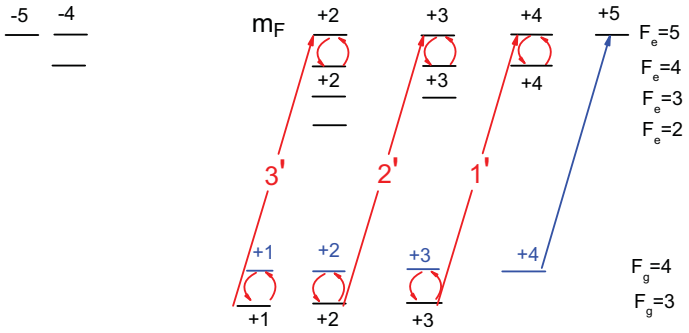

Figure 3.25: Partial diagram of the atomic transitions of D_2 line of Cs. The transition probability between two states can be modified in an external magnetic field only if at least one of the states is mixed. According to the selection rules $\Delta m_F = 0, \Delta L = 0, \Delta J = 0, \Delta F = \pm 1$, there only 4 states ($F_g = 4, m_F = +4, F_g = 4, m_F = -4, F_e = 5, m_F = +5 and F_e = 5, m_F = -5$) which are not mixed. Therefore, for D_2 line and σ^+ radiation the transition probability between $F_g = 4, m_F = +4 \rightarrow F_e = 5, m_F = +5$ remains the same.

3.3.1 Case of σ^+ circular polarized laser excitation, ^{85}Rb, ^{87}Rb, D_2 line

A nano-cell filled with the Rb atomic vapor has been used in our experiment, allowing to obtain sub-Doppler spectra, thus resolving a large number of hyperfine and Zeeman transition components. The general design of the Rb nano-cell is similar to that described in [40, 72] and the photograph with a tapered gap is shown in Fig. 1.4 (Chapter I). The region with the thickness $L = \lambda/2 = 390$ nm which is used in the experiments is marked by the oval in Fig. 1.4. The side arm temperature in present experiment was 120° C, while the windows temperature was kept about 20° C higher to prevent condensation. This temperature regime corresponds to the Rb atomic number density $N = 2 \times 10^{13}$ at/cm^3. The nano-cell operated with a special oven with two optical outlets. The oven (with the nano-cell fixed inside) was rigidly attached to a translation stage for smooth vertical movement to adjust the needed vapor column thickness without variation of thermal conditions. Note, that all experimental results have been obtained with Rb vapor column thickness $L = \lambda/2 = 390$ nm.

Experimental setup

Fig. 3.26 presents the experimental scheme for the detection of the absorption spectrum of the nano-cell filled with Rb. It is important to note that the implemented $\lambda/2$-method exploits strong narrowing of absorption spectrum at $L = \lambda/2$ as compared with the case of an ordinary

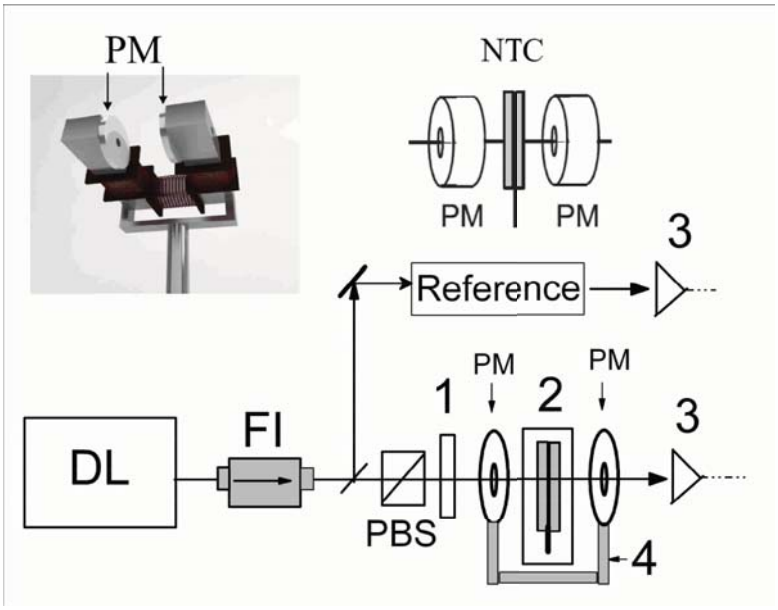

Figure 3.26: Sketch of the experimental setup. DL - tunable diode laser, FI - Faraday isolator, 1 - $\lambda/4$ plate, PBS Polarizing Beam Splitter, 2 - NC in the oven, Reference - auxiliary Rb NC providing $B = 0$ G reference spectrum, PM permanent magnets, 3 - photo-detectors, 4 - metallic magnetic core.

cm-size cell. Particularly, the absorption line-width for Rb D_2 line ($L = \lambda/2 = 390$ nm) reduces to about of 200 MHz (FWHM), as opposed to that in an ordinary cell (about of 500 MHz). In the experiment we used the radiation of a continuous wave narrowband diode laser with the wavelength of 780 nm and the width of 10 MHz. In the current experiment we had the choice to use a diode laser with the line-width of $\simeq 1$ MHz, however the mode hop free regime is only of 5 GHz, which is too small to register all 20 atomic transitions. Meanwhile with the laser used in the experiment the mode hop free tuning range is 40 GHz. The linearity of the scanned frequency was tested by simultaneously recorded transmission spectra of a Fabry-Pérot etalon (not shown). The nonlinearity has been evaluated to be about 1% throughout the spectral range. The strong magnetic field was produced by two ∅50 mm permanent magnets (PM) with 3 mm holes (to allow the radiation to pass) placed on the opposite sides of the NC oven and separated by a distance that was varied between 40 and 25 mm (see the upper inset in Fig. 3.26). The magnetic field was measured by a calibrated Hall gauge. To control the magnetic field value, one of the magnets was mounted on a micrometric translation stage for longitudinal displacement. In the case where the minimum separation distance is of 25 mm, the magnetic field B produced inside the NC reaches 3600 G. To enhance the magnetic field up to 6 kG,

the two PM were fixed to a metallic magnetic core with a cross section of 40 mm ×50 mm. Additional form-wounded Cu coils allow for the application of extra B-fields (up to ±1 kG) (see the inset in Fig. 3.26.). The beam with σ^+ circular polarization was formed by a $\lambda/4$ plate. The beam was focused by a lens (f = 20 cm) on the nano-cell to create a spot size ($1/e^2$ diameter, i.e. the distance where the power drops to 13.5 % of its peak value) in the cell of d = 0.6 mm and then collimated by a second lens (not shown in Fig. 3.26). To form the frequency reference (from which the frequency shifts were measured), a part of the laser beam was directed to a unit composed of an additional NC with $L = \lambda/2$. The absorption spectrum of the latter at the atomic transition $F_g = 1 \rightarrow F_e = 1, 2$ served as a reference (another weak transition $F_g = 1 \rightarrow F_e = 0$ is not well seen).

3.3.2 Experimental results and discussions

Magnetic field $B < 4$ kG

In case of relatively low magnetic fields ($\sim$ 1 kG) there are 60 allowed Zeeman transitions when circular laser radiation excitation is used, with 22 atomic transitions belonging to ^{87}Rb, and 38 transitions belonging to ^{85}Rb D_2 line. These numerous atomic transitions are strongly overlapped and can be partially resolved in case of using ^{87}Rb or ^{85}Rb isotope. While using natural Rb, the implementation of $\lambda/2$-method allows one to resolve practically each individual atomic transition in the case of $B \geq 4$ kG. The reduction of the total number of allowed atomic transitions at high magnetic fields down to 20 is caused by the effect of strong reduction of the atomic transitions probabilities for 40 transitions. Note, that for $B \gg B_0$ the number of allowed transitions can be simply obtained from the diagrams shown in Fig. 3.27.

In Fig. 3.28 the absorption spectrum of Rb nano-cell with $L = \lambda/2$ for the longitudinal magnetic field B = 3550 G and σ^+ polarized laser excitation is shown. The laser power is 10 μW. For Rb D_2 line there are 20 atomic absorption resonances located at the atomic transitions. Among these transitions 12 belong to ^{85}Rb, and 8 transitions belong to ^{87}Rb. The atomic transition pairs labeled (19, 18) and (7, 5) are strongly overlapped (although in the case of strongly expanded spectrum the peaks belonging to the corresponding transitions are well detected), while the other 16 transitions are overlapped partially, and the positions of the

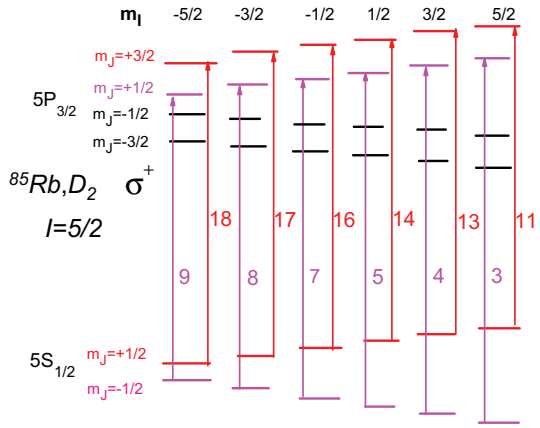

(a) ^{85}Rb ($I = 5/2$), D_2 line transitions in HPB regime. The selection rules are: $\Delta m_J = +1$; $\Delta m_I = 0$. Therefore, there are 12 atomic transitions marked by the respective numbers 3, 4, 5, 6, 8, 9, 12, 13, 15, 16, 17 and 19.

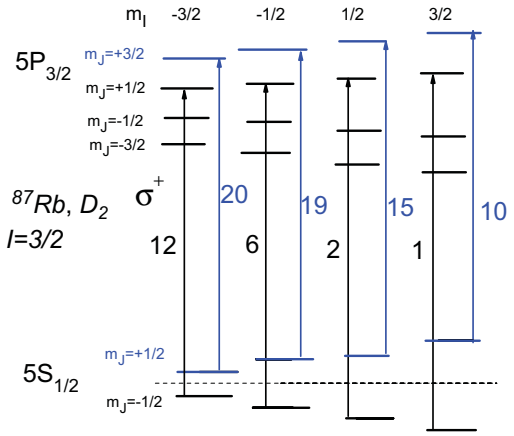

(b) ^{87}Rb ($I = 3/2$), D_2 line transitions in HPB regime. The selection rules are: $\Delta m_J = +1$; $\Delta m_I = 0$. Therefore, there are 8 atomic transitions marked by the respective numbers 1, 2, 7, 10, 11, 14, 18 and 20.

Figure 3.27: The diagrams of the transitions of ^{85}Rb and ^{87}Rb for D_2 line and σ^+ polarized radiation in the basis of m_I, m_J.

absorption peaks are well seen. Thus, the fitting of the absorption spectrum with 20 atomic transitions is not a difficult problem. The vertical bars presented in Fig. 3.28 indicate the frequency positions and the magnitudes for individual transitions between the Zeeman sublevels as given by numerical simulations using the model described below. The corresponding atomic transitions presented by the vertical bars are indicated in the upper corner of Fig. 3.28.

Magnetic field $B > 4$ kG: hyperfine Paschen-Back regime

In the case of strong ($B > 4$ kG) magnetic fields, the frequency separation between the atomic transitions increases, which allows one to separate practically any individual transition by using $\lambda/2$-method. A remarkable value of the magnetic field is 4.5 kG, since at $B > 4.5$ kG, 20 atomic transitions are regrouped to form two separate groups of ten transitions each and the frequency interval between these two groups increases with the magnetic field (see below).

In Fig. 3.29 the absorption spectrum of Rb nano-cell of $L = \lambda/2$ for $B = 6850$ G and σ^+ laser excitation is shown. There are still 20 atomic absorption resonances of Rb D_2 line located at the atomic transitions. Among these transitions, 12 belong to ^{85}Rb, and 8 transitions belong to ^{87}Rb. Atomic transition pairs labeled $19-18$, $15-14$ and $3-2$ are overlapped, while the other 14 transitions are overlapped partially, and the positions of the absorption peaks of the individual transitions are well detected. The left curve presents the absorption spectrum of

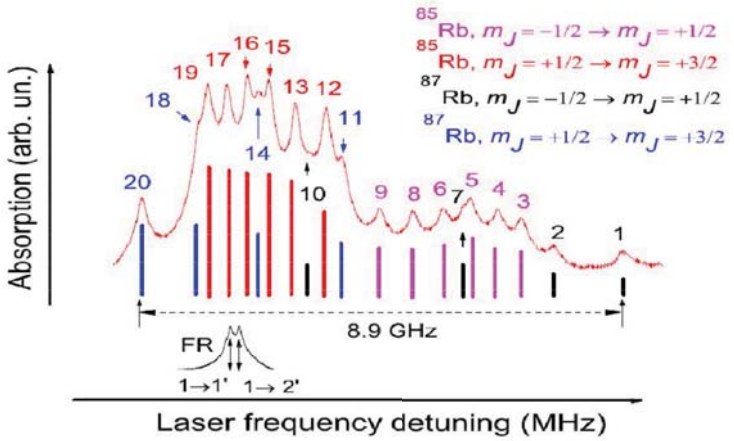

Figure 3.28: Absorption spectrum of Rb nano-cell with $L = \lambda/2$ for $B = 3550$ G and σ^+ laser excitation. The bottom curve (FR-frequency reference) is the absorption spectrum of the reference NC showing the positions of ^{87}Rb $F_g = 1 \rightarrow F_e = 1$ $(1 \rightarrow 1')$ and $F_g = 1 \rightarrow F_e = 2$ $(1 \rightarrow 2')$ transitions at $B = 0$ G (the frequency separation is 157 MHz). In the upper corner the corresponding atomic transitions are indicated. The absolute value of the peak absorption of the transition labeled as 1 is $\sim 0.3\%$.

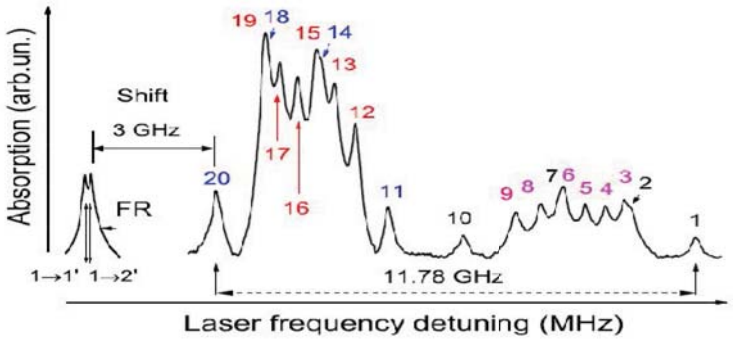

Figure 3.29: Absorption spectrum of Rb nano-cell with $L = \lambda/2$ for $B = 6850$ G and σ^+ laser excitation. For the transition labels, see Fig. 3.27. The left curve is the absorption spectrum of the reference nano-cell showing the positions of ^{87}Rb $F_g = 1 \rightarrow F_e = 1$ $(1 \rightarrow 1')$ and $F_g = 1 \rightarrow F_e = 2$ $(1 \rightarrow 2')$ transitions at $B = 0$ G (the frequency separation is 157 MHz).

the reference nano-cell with $L = \lambda/2$ showing the positions of the ^{87}Rb, $F_g = 1 \rightarrow F_e = 1, 2$ transitions for $B = 0$ (the frequency shift of the transitions is determined with respect to $1 \rightarrow 2'$ transition). Figure 3.30.(a) shows the fragment of the spectrum (presented in Fig. 3.29) for the atomic transitions labeled $1 - 10$, where the transitions labeled $1, 2, 7$ and 10 belong to ^{87}Rb, while the transitions labeled $3 - 6, 8$, and 9 belong to ^{85}Rb. The fitting (with the pseudo-Voigt profiles) is justified through the following advantageous property of the $\lambda/2$-method: in case of a weak absorption, the absorption coefficient A of an individual transition component is proportional to σNL. Measuring the ratio of A_i values for different individual transitions, it is straightforward to estimate their relative probabilities (line intensities).

The fragment of the spectrum (presented in Fig. 3.29) is shown in Fig. 3.30(b) for the atomic transitions labeled $11-20$, where the transitions labeled $11, 14, 18$ and 20 belong to ^{87}Rb, while the transitions labeled $12, 13, 15, 16, 17$ and 19 belong to ^{85}Rb. It is important to note that, (also see Fig. 3.28), the absorption peak numbered 1 is the most convenient for magnetic field measurements, since it is not overlapped with any other transition in the range of $1-10$ kG (see also Fig. 3.31), while having a strong detuning value in the range of $2-2.3$ MHz/G.

3.3.3 The manifestations of hyperfine Paschen-Back regime

As already mentioned above, the magnetic field required to decouple the electronic total angular momentum and the nuclear magnetic momentum is given by $B \gg B_0 = A_{hfs}/\mu B$. For ^{85}Rb and ^{87}Rb it is estimated to be approximately equal to B_0 (^{87}Rb) $\simeq 2$ kG, and B_0 (^{85}Rb) $\simeq 0.7$ kG. For such strong magnetic fields when I and J are decoupled (HPB regime), the eigenstates of the Hamiltonian are described in the uncoupled basis of J and I projections $(m_J;\ m_I)$. Fig. 3.27 shows 12 atomic transitions of ^{85}Rb labeled $3-6, 8, 9, 12, 13, 15-17$ and 19 for the case of σ^+ polarized laser excitation in the HPB regime and 8 transitions of ^{87}Rb labeled $1, 2, 7, 10, 11, 14, 18$ and 20.

Simulations of magnetic energy sublevels and relative transition probabilities for Rb D_2 line have been realized with the theoretical model presented in Chapter II. Fig. 3.31 illustrates the frequency positions (i.e. frequency shifts) of the components $1-20$ as functions of the magnetic field B. The theoretical curves are shown by solid lines. The black squares are the experimental results which are in a good agreement with the theoretical curves (with an error of 3%). As seen, the atomic transitions are regrouped at $B > 4500$ G to form two new sets of ten transitions each. Note, that the frequency separation between these two groups increases with B. The dashed line denotes the frequency position of the ^{87}Rb, $F_g = 1 \rightarrow F_e = 2$ transition for $B = 0$.

The experimental values of the slopes at $B = 7$ kG are $s_1 \simeq 2.29$ MHz/G for the group of transitions $1-10$ (this value for ^{85}Rb transitions is slightly larger, while for ^{87}Rb is slightly smaller) and $s_2 \simeq 1.42$ MHz/G for the group of transitions $11-20$ (this value for ^{85}Rb transitions

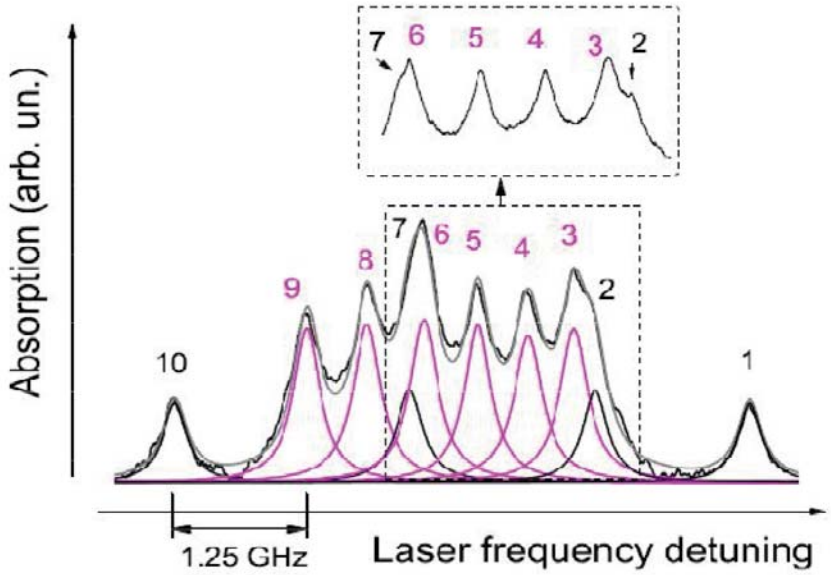

(a) The group contains the atomic transitions labeled 1-10 which are fitted with the "pseudo-Voigt" profiles with the line-width of 250 MHz; the inset shows an expanded view of the part of the experimental results limited by the dashed rectangle.

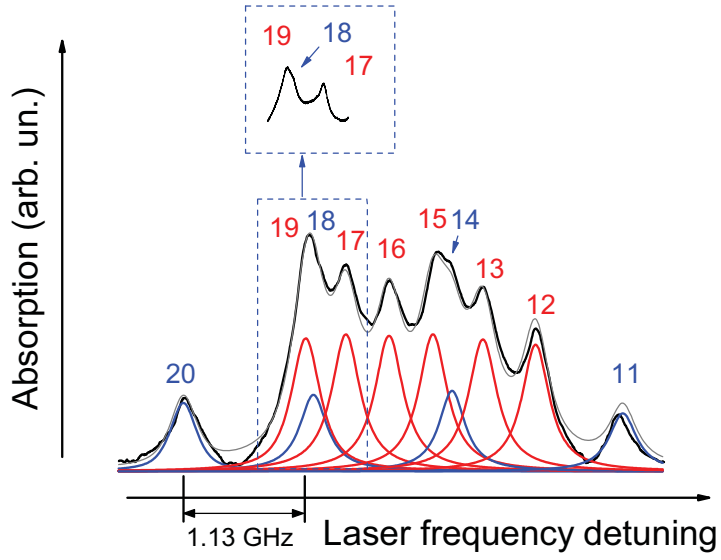

(b) The group contains the atomic transitions labeled 1120 which are fitted with the "pseudo-Voigt" profiles with the line-width of 250 MHz; the inset shows an expanded view of the part of the experimental results limited by the dashed rectangle.

Figure 3.30: Fragments of the absorption spectrum presented in Fig. 3.29.

is slightly smaller, while for ^{87}Rb is slightly larger). The theoretical values for the slopes at $B \gg B_0$ (Eq. 3.2) are $s_1 \simeq 2.33$ MHz/G and $s_2 \simeq 1.39$ MHz/G for the groups $1-10$ and $11-20$, respectively. The values for the Landé factors g_I, g_J, hyperfine constants A_{hfs} and B_{hfs} are given in [132]. Consequently, at $B \geq 20$ kG (when the condition of HPB is fully satisfied

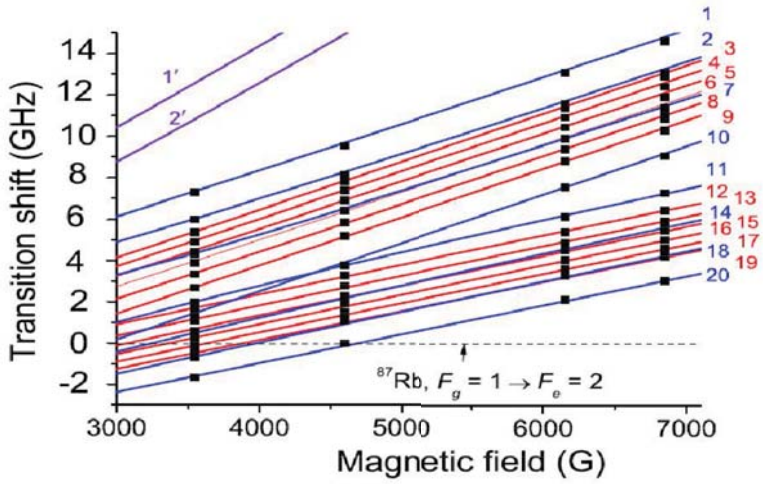

Figure 3.31: Frequency positions of the Rb, D_2 line atomic transitions 1-20 versus the magnetic field. Solid lines are the calculated curves and black squares are the experimental results (with an error of 3%). At $B > 4.5$ kG, the transitions are regrouped to form two groups of ten transitions each. For $B \gg B_0$ the frequency slope of the first group (1-10 transitions) is $s_1 \approx 2.33$ MHz/G, and for the second group (11-20 transitions) $s_2 \approx 1.39$ MHz/G. Two upper lines show $1'$ and $2'$ belonging to the ^{87}Rb, D_2, $F_g = 1 \rightarrow F_e = 3$ transitions, with the probability reducing to zero at $B > 6$ kG.

for ^{87}Rb atoms, too), the slope for the group $1-10$ increases slightly to s_1, while the slope for the group $11-20$ decreases slightly to s_2. In addition, one can easily find from Eq. (3.1) the frequency intervals between the components within each group.

Fig. 3.32 presents the theoretical values of $1-20$ atomic transitions probabilities (intensities) in the fields of $5-7$ kG. Let us compare the experimental results presented in Fig. 3.29 and Fig. 3.30 obtained for $B = 6850$ G with the theoretical calculations of the atomic transitions probabilities shown in Fig. 3.32. The atomic transitions labeled $3, 4, 5, 6, 8$ and 9 of ^{85}Rb shown in Fig. 3.30(a) have the same amplitudes (probabilities) with inaccuracy less than 5% and this is in a good agreement with the theoretical curves shown in the IV-th group in Fig. 3.32. The atomic transitions labeled $12, 13, 15-17$ and 19 shown in Fig. 3.30(b) have the same amplitudes with inaccuracy less than 5% and this is in a good agreement with the theoretical curves shown in the II-nd group in Fig. 3.32. It is easy to see that there is a similar good agreement between the amplitudes (probabilities) for the atomic transitions of ^{87}Rb shown in Fig. 3.30 with the theoretical curves shown in the I-st and III-rd groups. Note, that the probabilities of the transitions for ^{87}Rb inside the same group $1-10$ or $11-20$ are nearly two times larger than the probabilities for ^{85}Rb inside the same group. However, since for natural

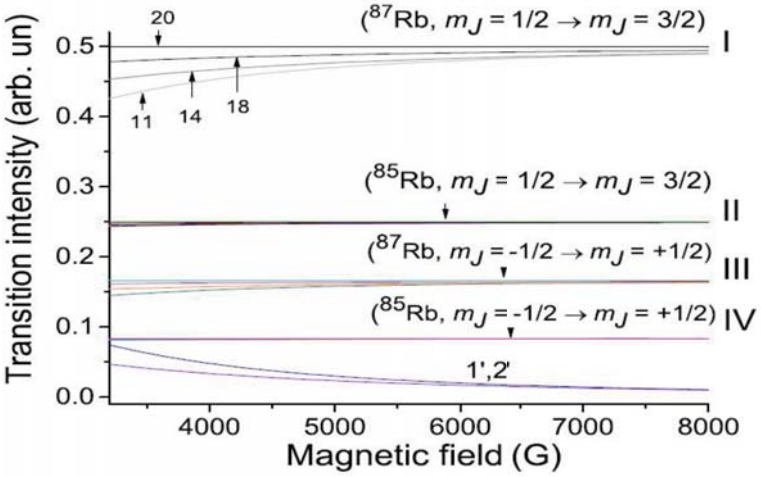

Figure 3.32: The intensities (probability) of the atomic transitions: (1-st group) ^{87}Rb, D_2 line transitions labeled 11, 14, 18, and 20; (2-nd group) ^{85}Rb, D_2 line transitions labeled 12, 13, 1517, and 19; (3-rd group) ^{87}Rb, D_2 line transitions labeled 1, 2, 7, and 10; (4-th group) ^{85}Rb, D_2 line transitions labeled as 3, 4, 5, 6, 8 and 9. The transition probabilities differ significantly at low B-fields but tend to the same value within the group at $B \gg B_0$. Two lower curves show $1'$ and $2'$ belonging to the ^{87}Rb, D_2, $F_g = 1 \rightarrow F_e = 3$ transitions, with the probability reducing to zero at $B > 6$ kG.

rubidium the atomic density ratio $N(^{85}\text{Rb})/N(^{87}\text{Rb}) \simeq 2.6$, the peak absorption of the atomic transitions for ^{85}Rb is nearly 1.5 times larger than that for ^{87}Rb (Fig. 3.30).

It is worth to note that the probability of the atomic transition for ^{87}Rb labeled 20 (for low magnetic field it could be presented as transition $F_g = 2, m_F = +2 \rightarrow F_e = 3, m_F = +3$) is the same in the whole range of magnetic field from zero up to 10 kG. This is the GT presented above. There is also guiding atomic transition for ^{85}Rb labeled 19 (it could be presented as transition $F_g = 3, m_F = +3 \rightarrow F_e = 4, m_F = +4$). It has the same probability in the range of magnetic fields from zero up to 10 kG. Since for the transitions labeled 19 and 20 the absolute value of the probability could be calculated from Eq. (3.1), thus using the experimental results presented in Fig. 3.30(b) the absolute value of the probabilities for the other atomic transitions (modified by magnetic field) can be calculated as well. Also, due to the above mentioned reason the frequency shifts of transitions labeled 19 and 20 as a function of magnetic field is simply linear with a fixed slope of $s = 1.39$ MHz/G. Note, that the reduction of the total number of Rb D_2 transitions to strictly 20 in strong magnetic fields (which are well described by the diagrams presented in Fig. 3.27), as well as the behavior of the slopes s_1 and s_2 of ^{85}Rb and ^{87}Rb (which are close to the values obtained by Eq. 3.2) is the manifestation of the hyperfine

Paschen-Back regime.

3.3.4 Comparison of the peculiarities of Rb D_2 line with Rb D_1 line

There are three main distinctions in the behavior of atomic transitions for D_2 line as compared with the behavior for D_1 line (the results for D_1 line are presented in [88, 93]).

i) At $B > 4.5$ kG D_2 absorption spectrum contains 20 well resolved atomic transitions, which are regrouped in two completely separate groups of 10 atomic transitions each and frequency separation between two groups increases with magnetic field. Meanwhile, for D_1 line there are only 10 atomic transitions forming one group.

ii) There are two remarkable guiding transitions for D_2 line: for ^{87}Rb atom, the transition labeled 20 and for ^{85}Rb atom, the transition labeled 19. In a wide region of magnetic fields from zero up to 10 kG the probabilities of GT remain unchanged. Also, the frequency shifts of the guiding transitions simply linear versus magnetic B-field. Such type GT are absent for D_1 line in the case of circular polarized radiation.

iii) In order to determine theoretically the frequency positions of atomic transitions in the case of D_1 line ($J = 1/2$) the well-known Rabi-Breit formulas can be implemented, while they are not useful for D_2 line ($J = 3/2$).

3.3.5 Rb D_2 line: π polarized laser excitation

In this Paragraph we present the results of experimental and theoretical studies of the Rb D_2 line atomic transitions, $\lambda = 780$ nm (both for the ^{87}Rb and the ^{85}Rb isotopes) in a wide range of magnetic fields of $B \sim 3$ kG -7 kG, for the case of π linear polarized laser excitation, using nano-cells filled with the Rb atomic vapor, with the cell thickness $L = \lambda/2 = 390$ nm.

As it is mentioned above when $B \ll B_0$ ($B_0 \simeq 0.7$ kG for ^{85}Rb and ~ 2 kG for ^{87}Rb) the splitting of atomic levels is described by the total angular momentum of the atom, $F = J + I$ and its projection m_F, where $J = L + S$ is the total electron angular momentum and I is the nuclear magnetic momentum. With the selection rules taken into account, it can be shown that, for the case of π polarized radiation, the total number of atomic transitions between ground F_g and upper F_e levels is given by $F_e - F_g = \Delta F = 0, \pm 1, \Delta m_F = 0$. It should be noted that, in

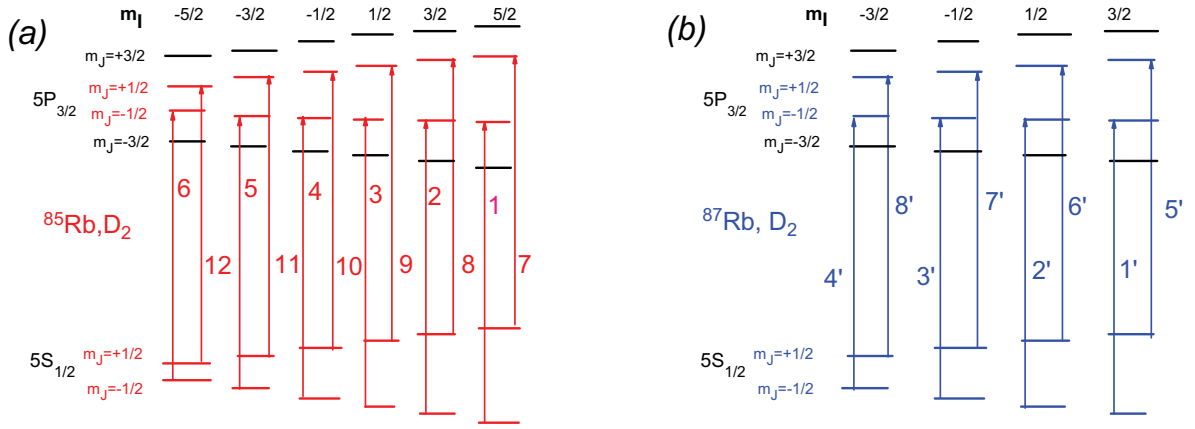

(a) The diagram of ^{85}Rb transitions. According to the selection rules for the case of -polarized radiation $\Delta m_J = 0$ and $\Delta m_I = 0$, there are 12 transitions (labeled as 1-12)

(b) The diagram of ^{87}Rb transitions. According to the selection rules for the case of -polarized radiation $\Delta m_J = 0$ and $\Delta m_I = 0$, there are 8 transitions (labeled as $1'$-$8'$)

Figure 3.33: Transition diagrams of the D_2-lines of ^{85}Rb and ^{87}Rb isotopes at the PaschenBack regime in the basis of m_I, m_J for the π polarized radiation.

the external magnetic field, the spectrum may also display transitions $F_g, m_F = 0 \to F, m_F = 0$ for the $\Delta F = 0$ case (such transitions are forbidden at $B = 0$). The total number of atomic transitions is 64, including 40 transitions of ^{85}Rb and 24 transitions of ^{87}Rb.

Strong magnetic field leads to HPB regime in hyperfine structure: for $B \gg B_0$, J and I momenta become decoupled, and the splitting between atomic levels is described by projections m_J and m_I. Figure 3.33 shows the transition scheme of ^{85}Rb and ^{87}Rb for the π polarized radiation in the HPB regime. As can be seen, in the HPB regime, the number of transitions decreases from 40 to 12 transitions of ^{85}Rb, and from 24 to 8 of ^{87}Rb (labeled $1' - 8'$). Such significant decrease in the transition number is characteristic of alkali atoms in the HPB regime.

3.3.6 Experimental Results

The same nano-cell filled with the Rb which is described in the previous paragraph has been used in below presented experiments. The experimental setup is shown schematically in Fig. 3.34. The absorption spectrum is recorded using a Rb-filled nano-cell with a thickness in the laser beam direction of $L = \lambda/2 = 390$ nm where λ is the D_2 line wavelength. The nano-cell was placed in a special oven with holes for laser radiation. Heating the nano-cell up to $115 - 120°$ C provided an atomic density of $N \sim 10^{13}$ cm^3. Atomic transitions were studied using an

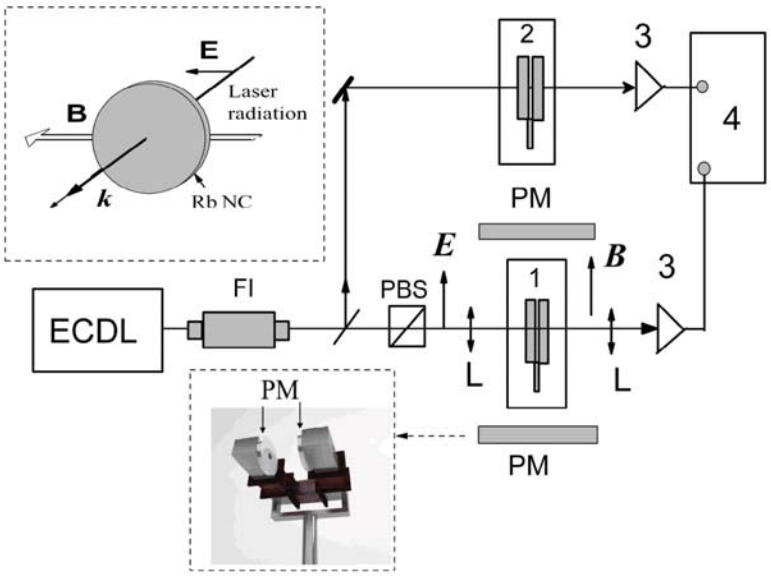

Figure 3.34: Schematic diagram of the experimental setup: (ECDL) extended cavity diode laser, (FI) Faraday isolator, PM-permanent magnets, (PBS) polarizing beam splitter, (1) the main Rb nano-cell inside an oven, (2) additional Rb nano-cell used as a frequency reference, (L) lenses, (3) photodetectors, and (4) a Tektronix TDS2014B oscilloscope.

extended cavity diode laser (ECDL) with a radiation wavelength of 780 nm and a narrow line width of ~ 1 MHz. The position of the laser beam focus spot was adjusted in such a way as to fulfill the $L = \lambda/2$ condition for the thickness of the Rb vapor column. The oven containing the nano-cell was placed between strong magnets, which were attached to a metal magnetic conductor (see the lower insert in Fig. 3.34) to obtain magnetic fields up to ~ 6 kG. A direct current coil wounded on the magnetic conductor allowed tuning the magnetic field strength in the $4.3 - 7$ kG range. Laser emission after focusing into the nano-cell ($f = 20$ cm; caustics size ~ 0.4 mm) was collimated with additional lens L (Fig. 3.34.). The relative orientations of magnetic induction B, laser electric field E, and laser wavevector k ($k = 2\pi/\lambda$) are shown in the upper inset of Fig. 3.34. To obtain the reference frequency at $B = 0$ (relative to which the frequency shifts were measured), a fraction of laser emission was directed to an additional nano-cell with a thickness of $L = \lambda/2$.

Figure 3.35 shows a total spectrum of the $5S_{1/2} \rightarrow 5P_{3/2}$ transitions ($1' - 8$' transitions of ^{87}Rb, and $1 - 12$ transitions of ^{85}Rb) for $B \simeq 5900$ G obtained using the $\lambda/2$-method for π polarized excitation. As it is seen, transitions 9 and $6'$ are spectrally resolved. The lowest curve in Fig. 3.35 is the reference spectrum for $B = 0$. This spectrum was used to verify the linearity of the frequency scanning. Absolute absorption value in the $\lambda/2$-method is 12%. Absorption

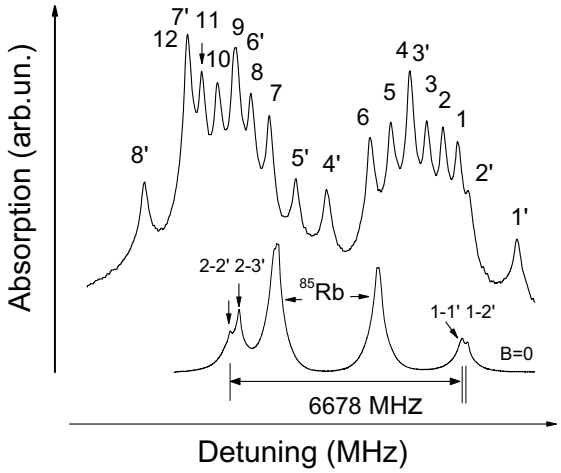

Figure 3.35: Total absorption spectrum of the Rb D_2-line obtained by the implementation of the $\lambda/2$-method for $B \approx 5.9$ kG and the laser power of 10 μW. The spectrum displays 20 $5S_{1/2} \rightarrow 5P_{3/2}$ transitions, containing the 12 transitions of ^{85}Rb (1-12) and the 8 transitions of ^{87}Rb $(1' - 8')$. The lower curve is the reference absorption spectrum at $B = 0$ G, used to determine the frequency shifts relative to the $1' - 2'$ transition of ^{87}Rb. The reference cell temperature iss 150° C.

strength may be written as $A = \sigma NL$ (see before). Consequently, the transition amplitudes in the absorption spectra are proportional to the atomic transition probabilities of the ^{87}Rb and ^{85}Rb isotope groups. To compare the transition amplitudes in the ^{87}Rb and ^{85}Rb groups, one needs to take into account the abundance ratio of ^{85}Rb and ^{87}Rb isotopes, which is $\sim 72/28$. In addition, ground levels transition numbers in ^{85}Rb and ^{87}Rb are in the 12/8 ratio (Fig. 3.33).

The absorption lines in Fig. 3.35 were approximated using a pseudo-Voigt function. The fitting results are shown in Figs. 3.36 and 3.37. The thin vertical bars correspond to the spectral positions and amplitudes of the atomic transitions $1' - 8'$ (^{87}Rb) and $1 - 12$ (^{85}Rb) at $B \simeq 5.9$ kG. The transitions which are forbidden at $B = 0$ are labeled with numbers in circles. Their probabilities rapidly increase as B increases (see Fig. 3.36 and 3.37). As is seen from these figures, the $\lambda/2$-method allows tracing the behavior of every individual transition. For the case of the usual Rb-filled gas cell with a thickness of $L = 0.1 - 1$ cm, the Doppler width is > 500 MHz. Apparently, for the magnetic fields used in the present study, individual atomic transitions may be resolved only in a pure ^{87}Rb isotope spectrum [130].

Quantitative determination of the frequencies and probabilities of the transitions of the Rb D_2-line were performed in the framework of a known model that uses the Hamiltonian

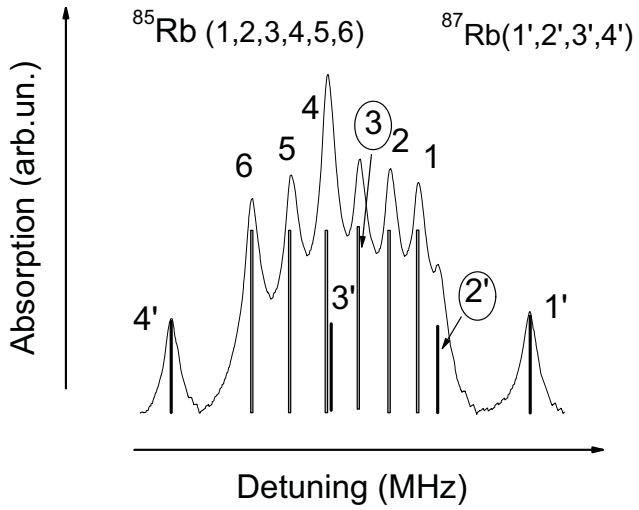

Figure 3.36: Fragment of the high frequency spectral region showing the $1' - 4'$ (^{87}Rb) and 1-6 (^{85}Rb) transitions of the Fig. 3.35. The transitions that are forbidden for $B = 0$ G are labeled with circles. Their probabilities promptly grow as B increases (see Fig. 3.39).

matrix for an atom in the magnetic field and takes into account all transitions within the atom hyperfine structure (see Chapter II). Figure 3.38 shows frequencies of the $1' - 8'$ (^{87}Rb) and $1 - 12$ (^{85}Rb) transitions for magnetic field in the $4 - 7$ kG range. The solid lines are calculated curves and the squares are experimental results. The experimental uncertainty is 2%. The frequency shift was measured relative to the ^{87}Rb, $F_g = 1 \rightarrow F_e = 1$ transition. In Fig. 3.35 this transition is denoted as $1 \rightarrow 1'$ and marked with arrow. Transitions $1'8'$ of the ^{87}Rb isotope are marked with arrows.

For $B > 5$ kG, the transitions rearrange into two large groups. The frequency gap between these groups increases with the increase in the magnetic field strength. Each group includes six transitions of ^{85}Rb and four transitions of ^{87}Rb. At $B \gg B_0$, the slope of the plot (s) may be readily obtained from formula (3.2). For the $1'-4'$ (^{87}Rb) and $1-6$ (^{85}Rb) groups of transitions, $s \simeq 0.46$ MHz/G, and, for the $5' - 8'$ (^{87}Rb) and $7 - 12$ (^{85}Rb) groups of transitions, $s \simeq 0.46$ MHz/G. It should be noted that, due to the same group of transitions, the $g_J m_J$ values for ^{87}Rb and ^{85}Rb are the same, the slope value s in the given group is the same for ^{87}Rb and ^{85}Rb.

It should also be noted that transition $1'$ of ^{87}Rb is completely resolved already at $B > 50$ G (see Fig. 3.38) and has the largest frequency as the field strength increases above this value.

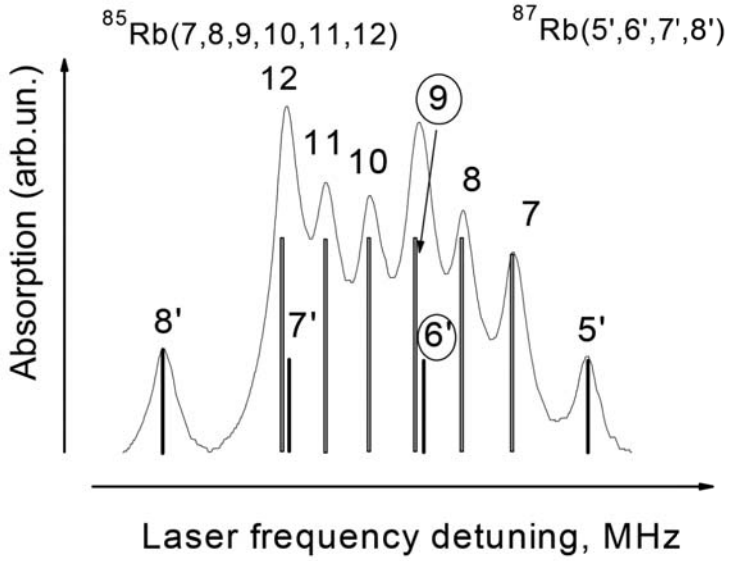

Figure 3.37: Fragment of the low frequency spectral region showing $5' - 8'$ (^{87}Rb) and 7-12 (^{85}Rb) transitions. The transitions that are forbidden for $B = 0$ G are labeled with circles. Their probabilities promptly grow as B increases (see Fig. 3.39).

In addition, the probability of this transition increases as the field strength increases. Because of these properties, this transition is well suited for measurements of strong magnetic fields (we see no restrictions on the upper boundary on the measured magnetic field strength, which can reach a few Tesla).

In addition, the Rb-filled nano-cell may be positioned with micrometer accuracy. Translation of this system may be used for mapping strongly inhomogeneous magnetic fields.

Figure 3.39 shows calculated dependence of the transitions intensities as a function of the magnetic field B. As is seen, the transition intensities of ^{85}Rb become almost the same for $B > 5$ kG. The case of ^{87}Rb requires stronger magnetic field. It stems from the large value of $B_0(^{87}\text{Rb}) \simeq 2.4$ kG, which is nearly three times larger than $B_0(^{85}\text{Rb}) \simeq 700$ kG. Consequently, attainment of the HPB regime, in which transition intensities become the same, takes place at higher fields. As is seen from Fig. 3.36 and 3.37, the transition amplitudes for ^{85}Rb are nearly equal for $B \simeq 5.9$ kG whereas the difference in the transition amplitudes for ^{87}Rb is of 10% that is in a good agreement with the theoretical curves (Fig. 3.39).

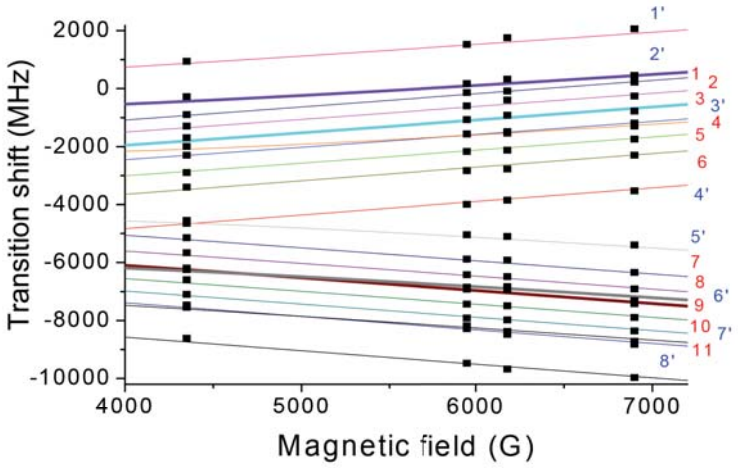

Figure 3.38: Calculated frequency shifts for the $1' - 8'$ (^{87}Rb) and 1-12 (^{85}Rb) transitions as a function of magnetic induction B. For $B \gg B_0$, transitions regroup into two groups. Each group includes six transitions of ^{85}Rb and four transitions of ^{87}Rb. Calculated curves are shown by solid lines, and experimental results are shown by squares (uncertainty is 2%). The frequency shifts were measured relative to the ^{87}Rb, $1 - 1'$ transition which is labeled with an arrow in Fig. 3.35

3.4 Summary

We have shown that the use of the nano-cell filled with K, Cs and Rb with the thickness $L = \lambda/2$ and $L = \lambda$ ($\lambda/2$- and λ- methods, where λ is the resonant wavelength of laser radiation) allowed us to study the frequency position and the line intensity of individual atomic transitions of the K, Cs and Rb atoms in a strong magnetic fields using a compact experimental setup. Before development of the nano-cells, such results could be obtained only with the use of a much more complex atomic beam technique

1. Nano-cell filled with K has been built and used to study optical atomic transitions in external magnetic fields. In particular, for π polarized radiation excitation the $\lambda/2$- and λ-methods allow to resolve eight atomic transitions of the ^{39}K (in two groups of four atomic transitions) and to reveal two remarkable transitions that we call Guiding Atomic Transitions. The probabilities of all other transitions inside the group (as well as the frequency slope vs magnetic field) tend to the probability and to the slope of GT. Note in the case of σ^+ circular polarization (D_1 line) there is one group of four transitions and GT does not exist. Among eight transitions there are also two transitions (forbidden for $B = 0$) with the probabilities undergoing strong modification under the influence of magnetic fields. Practically the complete

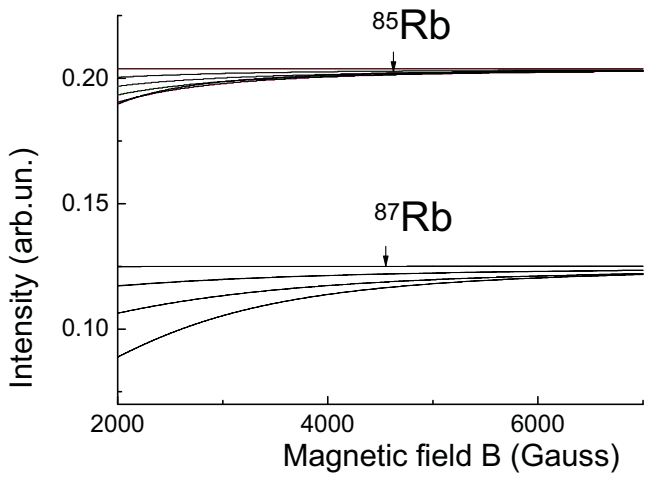

Figure 3.39: Calculated probabilities (intensities) of transitions for ^{85}Rb and ^{87}Rb as a function of magnetic induction B. For $B \gg B_0$ the probabilities of all transitions in the given group have the same asymptotic value.

decoupling of the total electronic momentum J and the nuclear spin momentum I (hyperfine Paschen-Back regime) is observed at relatively low ($\sim$ 1 kG) magnetic fields. Theoretical models describe the experiment very well.

2. Magnetic field-induced giant modification of probabilities for seven components of $6S_{1/2}, F_g = 3 \rightarrow 6P_{3/2}, F_e = 5$ transition of Cs D_2 line initially forbidden by selection rules is observed experimentally for the first time. For the case of excitation with circularly-polarized laser radiation, the probability of $F_g = 3, m_F = -3 \rightarrow F_e = 5, m_F = -2$ transition becomes the largest among 25 transitions of $F_g = 3 \rightarrow F_e = 2, 3, 4, 5$ group in a wide range of magnetic field $200 - 3200$ G. Moreover, the modification is the largest among D_2 lines of alkali metals. A nano-cell with thickness $L = 426$ nm filled with Cs has been used in order to achieve sub-Doppler resolution, which allows for separating the large number of atomic transitions that appear in the absorption spectrum when an external magnetic field is applied. For $B > 3000$ G the group of seven transitions $F_g = 3 \rightarrow F_e = 5$ is completely resolved and is located at the high frequency wing of $F_g = 3 \rightarrow F_e = 2, 3, 4$ transitions. For $B > 5000$ G the amplitudes of seven transitions $F_g = 3 \rightarrow F_e = 5$ tend to zero. There is one GT transition $F_g = 4, m_F = +4 \rightarrow F_e = 5, m_F = +5$, which is the strongest among all the 54 Zeeman transitions of Cs D_2 line. The applied theoretical model very well describes the experimental curves.

3. An efficient $\lambda/2$-method ($\lambda = 780$ nm) based on nano-cell filled with Rb is implemented to study the splitting of hyperfine transitions of ^{85}Rb and ^{87}Rb D_2 lines in an external magnetic field in the range of $B = 3$ kG -7 kG. It is experimentally demonstrated that at $B > 3$ kG from 38 (22) Zeeman transitions allowed at low B-field in ^{85}Rb (^{87}Rb) spectra in the case of σ^+ polarized laser radiation there remain only 12 (8) which is caused by decoupling of the momenta J and I (HPB regime). Note that at $B > 4.5$ kG in the absorption spectrum these 20 atomic transitions are regrouped in two completely separate groups of 10 atomic transitions each. Their frequency positions and fixed (within each group) frequency slopes, as well as the probability characteristics are determined. One GT of the ^{85}Rb (for low magnetic field could be presented as a transition $F_g = 3, m_F = +3 \rightarrow F_e = 4, m_F = +4$) and one GT of ^{87}Rb (for low magnetic field could be presented as transition $F_g = 2, m_F = +2 \rightarrow F_e = 3, m_F = +3$) are revealed. The experiment agrees well with the theory. Comparison of the behavior of atomic transitions for D_2 line compared with that of D_1 line is presented. Possible applications are described.

4. Atomic transitions of ^{85}Rb and ^{87}Rb isotopes in a strong transverse magnetic field with magnetic field of up to 7 kG have been studied experimentally. High spectral resolution is achieved owing to the application of a nano-cell with the thickness of $L = \lambda/2 = 390$ nm ($\lambda/2$-method) where $\lambda = 780$ nm is the wavelength of laser resonant with the Rb D_2-line. It has been observed that the number of atomic transitions in the transmission spectrum of linearly polarized (π) radiation decreases from 64 down to 20 transitions as the B-field strength increases above $B > 5$ kG. Four atomic transitions (two of ^{85}Rb and two of ^{87}Rb), which are forbidden at zero magnetic field, acquire significant strength in the strong magnetic field. Experimental results are in a good agreement with theory. Several practical applications of alkali-vapor-filled nano-cells have been proposed.

5. From an application point of view the obtained results can be used as follows:

i) A Frequency Reference based on a K, Cs or Rb filled nano-cells which are placed between two permanent ring magnets could form widely tunable atomic transitions over a range of several gigahertzes by simple displacement of the magnets.

ii) Having a fixed atomic frequency slope value and constant amplitude the "Guiding" Atomic Transitions of the K, Cs and Rb are very convenient for magnetic field measurements in a wide region up to 10 kG, while providing a several hundreds nanometer spatial resolution.

Chapter 4

SATURATED-ABSORPTION SPECTROSCOPY: ATOMIC TRANSITIONS IN STRONG MAGNETIC FIELDS (> 20 MT) WITH A MICROMETER-THIN CELL

The existence of crossover resonances makes saturated-absorption (SA) spectra very complicated when external magnetic field B is applied. It is demonstrated for the first time, to the best of our knowledge, that the use of micrometric-thin cells (MCs, $L \simeq 40$ μm) allows application of SA for quantitative studies of frequency splitting and shifts of the Rb atomic transitions in a wide range of external magnetic fields, from 0.2 *up to* 6 *kG* ($20 - 600$ *mT). We compare the SA spectra obtained with the MC with those obtained with other techniques and present applications for optical magnetometry with micrometer spatial resolution and a broadly tunable optical frequency lock.*

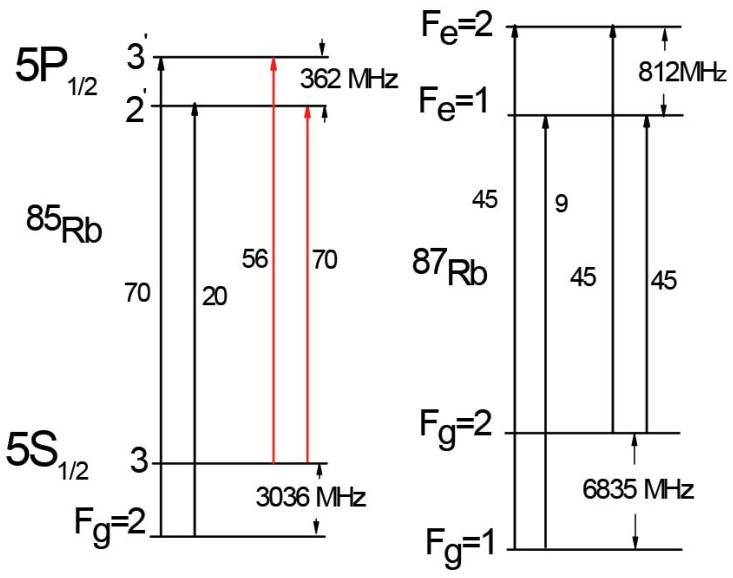

Figure 4.1: The hyperfine energy levels diagram of the D_1 line of ^{85}Rb and ^{87}Rb. Only the levels, which have been used in the experiment are shown .

4.1 Overview of the SA spectroscopy

Saturated absorption (SA) spectroscopy is widely used in the realization of frequency references for atomic transitions [96 - 110]. In this technique, the laser beam is split into a weak probe field and a strong pump field, which are sent to the interaction cell as counter-propagating overlapping beams. Because of opposite Doppler shifts, only the atoms moving perpendicular to the radiation propagation direction resonantly interact with both laser beams. For these atoms, the pump beam saturates the transition, and the absorption spectrum of the probe shows a Doppler-free dip, the so-called velocity selective optical pumping/saturation (VSOP) resonance located at the line center. With properly chosen pump and probe beam intensities, careful adjustment of the geometry, and the elimination of stray magnetic fields, the line width of the resonance (to which we refer to as "VSOP resonance") may be as narrow as the natural width of the transition.

When there are more than one upper hyperfine levels, it leads to more sophisticated spectra due to the overlap of the atomic transitions. The presence of a close-lying atomic transitions results the formation of several additional crossover resonances, which are formed when the laser frequency is exactly in the middle of two atomic levels. The CO resonance formation mechanism is explained in details in [113] in the case of two counter propagating beams.

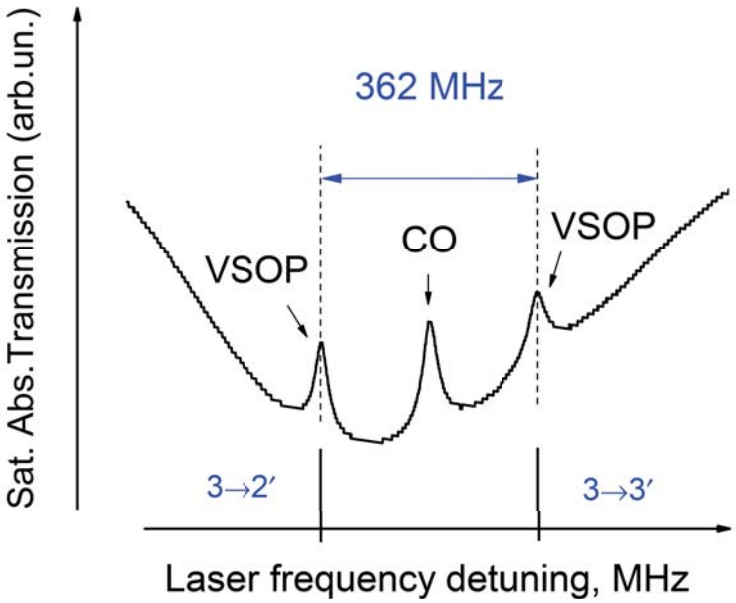

Figure 4.2: The Saturation Absorption spectrum obtained with 3 cm-long cell filled with the Rb. The VSOP resonances are located at the transitions of the ^{85}Rb, D_1 line, $F_g = 3 \rightarrow F_e = 2, 3$. Between these two VSOPs resonances a CO resonance is seen.

Several techniques allow for the elimination of CO resonances in atomic vapors are presented [30, 107]. Similar VSOP resonances without CO lines have been demonstrated in the transmission spectrum of the nano-cells filled with alkali metal, with a thickness $L = \lambda$, where λ is the transition wavelength [40], and in micrometric-thin cells (MCs) [49]. The CO resonances require atoms with a nonzero velocity projection, for which the interaction time is limited by the transit time between cell walls (see below). This results in strong CO suppression with respect to VSOP resonances [49]. In this Chapter, we demonstrate that, for magnetic fields $B > 200$ G, to about 6 kG, SA spectroscopy can be implemented successfully using micro-cells with the thickness $L \sim 30$ μm filled with Rb. The hyperfine energy levels (partial) diagram of the D_1 line of ^{85}Rb and ^{87}Rb is shown in Fig. 4.1. Figure 4.2 shows the Saturation Absorption spectrum obtained with 3 cm-long cell filled with the Rb. The VSOP resonances (at full width half maximum the line-width is ~ 25 MHz) are located at the atomic transitions of the ^{85}Rb, D_1 line, $F_g = 3 \rightarrow F_e = 2, 3$. Between these two VSOPs resonances a crossover resonance is seen. These VSOPs peaks of a decreased absorption are located exactly at the atomic transition frequencies, and arise because the atom in the ground level $F_g = 3$ absorbs a laser photon populating the excited level followed by the spontaneous decay to the ground level $F_g = 2$ or $F_g = 3$, an effect well known as optical pumping (OP) [111, 112, 114]. As a result, a fraction

of the atoms populates the $F_g = 2$ level, and the number of atoms absorbing from the $F_g = 3$ level is reduced. As a consequence, the absorption from this level decreases. The efficiency of OP is determined by the expression,

$$\eta \sim \frac{\Omega^2 \gamma_N t}{(\Delta + \boldsymbol{kv})^2 + \Gamma^2} \tag{4.1}$$

where t is the time of interaction of the laser radiation with an atom, Δ the frequency detuning from resonance, $\boldsymbol{v}$ is the atomic velocity, Γ is the sum of homogeneous and inhomogeneous broadenings, and $k = 2\pi/\lambda$. Equation (4.1) shows how the optical pumping efficiency grows with the interaction time t. For atoms flying perpendicularly to the laser beam, the interaction time is $t_D = D/\boldsymbol{v}$, where D is the laser beam diameter, while atoms flying along the laser beam have an interaction time of $t_L = L/\boldsymbol{v}$, where L is the thickness of the cell. Since usually laser beam diameter is $D \sim 1$ mm , while the thickness of the nano-cell is of order $L \sim 1$ μm , thus t_D exceeds t_L by three orders of magnitude. For atoms flying perpendicular to the laser beam, $\boldsymbol{kv}$ $= 0$ and the efficiency in Eq. (4.1) becomes maximal for $\Delta = 0$. For this reason, the VSOP peak is centered exactly at the atomic transition frequency. It is important to note that atoms with a longitudinal velocity, $\boldsymbol{v}_z = 2\pi\epsilon/k$ ($2\epsilon = 362$ MHz for the ^{85}Rb, D_1 line, $F_g = 3 \rightarrow F_e = 2, 3$) are participating in the CO resonance formation. The interaction time t_L for these atoms along the laser beam is rather small for $L \sim 1$ μm to provide efficient optical pumping, which is needed for the CO resonance formation. That's why in the case of the nano-cell use the CO resonances are absent, while in the case of 3 cm-long cell (Fig. 4.2) the CO with the amplitude which is larger than that of the VSOPs is seen. There are several parameters which influence the CO resonance amplitude, in particular, the frequency separation between the upper levels (2ϵ), the probabilities of the atomic transitions involved in the CO resonance formation, and the thermal atomic velocity of the alkali atom [2,3]. In Fig. 4.3 the upper curve shows the SA spectrum for the micro-cell with thickness $L = 60$ μm. As it is seen, due to the small thickness L (it means small interaction time t_L) the amplitude of the CO is several times smaller than that of 3 cm-long cell (Fig.4.2). The lower curve shows transmission spectrum of the nano-cell filled with Rb with the thickness $L = 795$ nm. Note that the CO resonance is not detectable

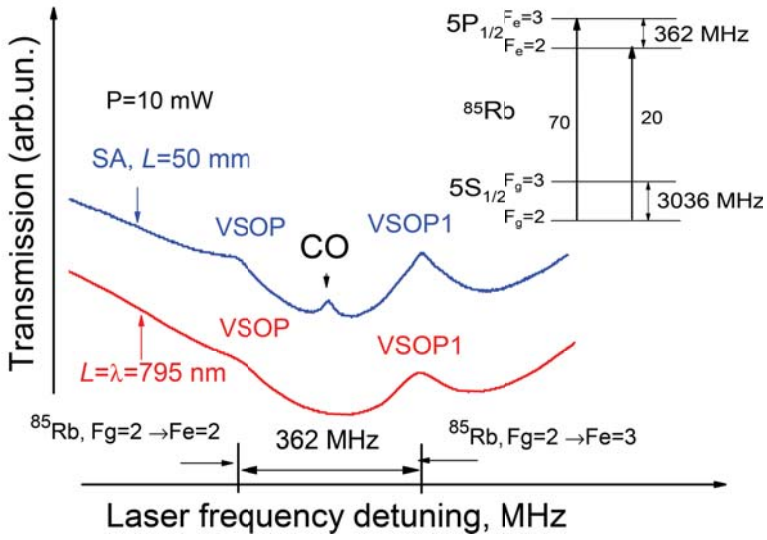

Figure 4.3: The upper curve - SA obtained with a cell with thickness $L = 60$ μm. The CO amplitude is much smaller compare to that presented in 4.2. The lower curve shows transmission spectrum of the nano-cell with $L = 795$ nm, the CO is absent.

for $2\epsilon = 362$ MHz when the cell thickness $L \leq 30$ μm. Meanwhile, for $2\epsilon \simeq 120$ MHz (^{85}Rb, D_2 line, $F_g = 3 \rightarrow F_e = 2, 3, 4$) the CO resonance is not detectable when the cell thickness $L \leq 6$ μm [49]. The explanation is that for smaller 2ϵ the longitudinal velocity $V_z = 2\pi\epsilon/k$ is smaller which causes increasing of the interaction time t_L. The Amplitude ratios of the CO and VSOP (for the transition ^{85}Rb, D_2 line, $F_g = 3 \rightarrow F_e = 3$) $A_{CO}/A_{VSOP(3-3')}$) as a function of the cell thickness L is shown in Fig. 4.4 (from the paper [49]). The dotted line in Fig. 4.4 is shown to guide the eye. As it is expected when the cell thickness L is reducing the amplitude of the CO resonance is also reducing.

As it is demonstrated in Chapter II and Chapter III, in high magnetic fields, the atomic optical transitions may dramatically change their frequencies and probabilities, in the hyperfine Paschen-Back regime [88 - 95]. Even for that large B-field values, the Doppler-broadened ^{85}Rb and ^{87}Rb lines are strongly overlapping. To eliminate the Doppler broadening, the SA (and polarization) spectroscopy in the weak/intermediate magnetic fields (up to < 100 G) was implemented in studies of atomic transitions [126 - 128]. However, the obtained spectra were rather complicated, primarily due to the presence of strong CO resonances also splitting into many components [126 - 128]. Thus, SA spectroscopy in typical vapor cells is practical only for $B < 100$ G. In order to demonstrate the destructive influence of the CO resonance in the SA spectrum in external magnetic field, let's consider the spectra shown in Fig. 4.5 (from the

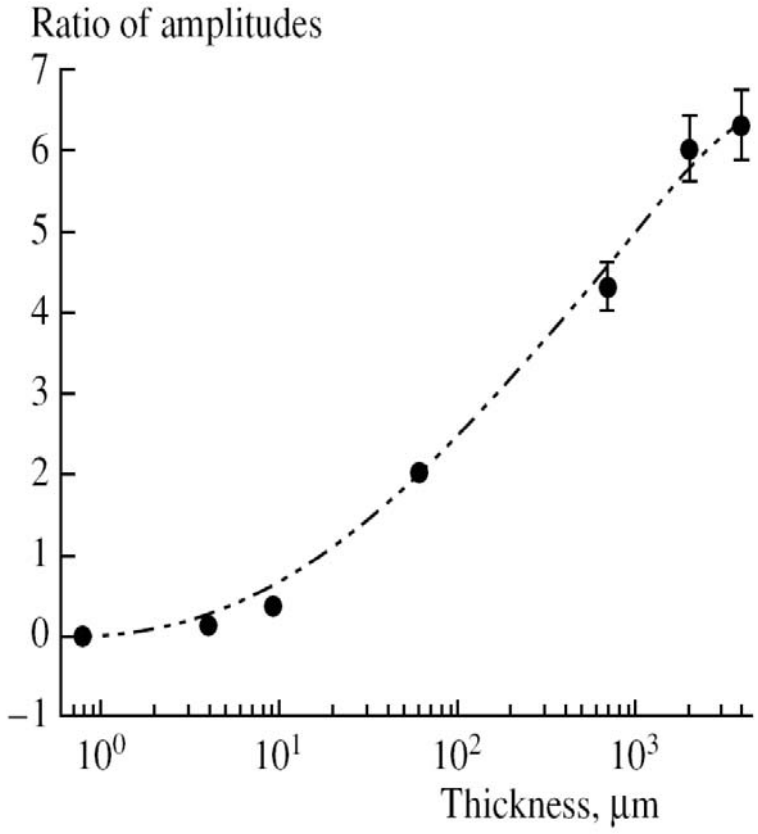

Figure 4.4: Amplitude ratios of the $A_{CO}/A_{VSOP(3-3')}$) as a function of the cell thickness L. The dotted line is shown to guide the eye.

paper [128]) that have been used for calibration of the magnetic field. The lower arrow shows the SA spectrum for zero magnetic field, which coincides with the SA spectrum shown in Fig.2. The upper arrow shows the SA spectrum for magnetic field for $B = 60$ G (the intermediate arrows shows SA spectrum for intermediate magnetic fields). As it is seen the obtained spectra are rather complicated, primarily due to the presence of strong crossover resonances, which are also splitting into many components. Note that for for $B > 60$ G the presented spectra are useless, meanwhile the Saturated Absorption spectra obtained with use of micro-cell with $L \simeq 30$ μm are useful for magnetic field B use up to ~ 6 kG (see below).

The micro-cell is similar in the design to the extremely thin cells presented in [94]. The rectangular 20×30 mm^2, 2.5 mm-thick sapphire window wafers, polished to ~ 1 nm surface roughness, form a vapor cell, wedged by placing spacers (the spacers are Platinum with dimensions of 1 mm $\times$ 30 μm) between the windows prior to gluing. The micro-cell is filled with a natural mixture of rubidium isotopes. The wedged gap allows one to study the SA spectra with a variable column thickness by probing various cell regions (see Chapter I).

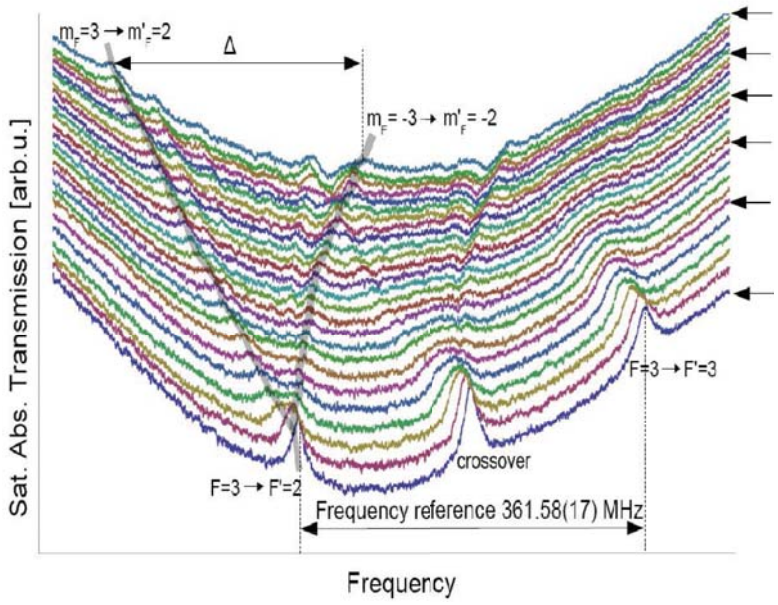

Figure 4.5: Saturated absorption spectra of the Doppler broadened line (^{85}Rb transitions from the $F = 3$ ground state) for different coil currents. Δ is the frequency difference between $F_g = 3, m_F = 3 \rightarrow F_e = 2, m_{F'} = 2$ and $F_g = 3, m_F = -3 \rightarrow F_e = 2, m_{F'} = -2$ transitions, which has been used to measure the magnetic field.

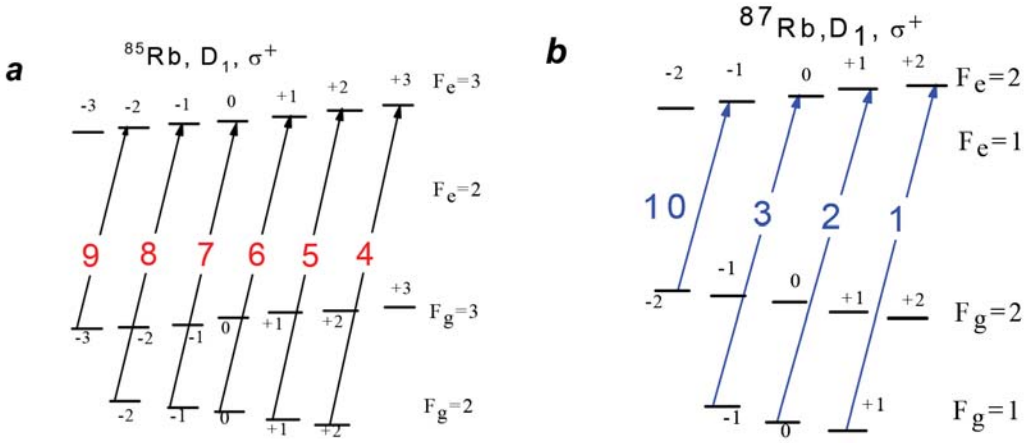

(a) (b)

Figure 4.6: The energy level diagram of the D_1 line of the ^{85}Rb (a) and ^{87}Rb (b) in an external magnetic field with the σ^+ atomic transitions of non-vanishing probability in the HPB regime. Note, that atomic transitions $F_g = 2 \rightarrow F_e = 2, F_g = 3 \rightarrow F_e = 2$ and $F_g = 3 \rightarrow F_e = 3$ (except the atomic transition labeled with number 9) have vanishing probability in the HPB regime.

The 30 μm -thickness of the cell is advantageous for the application of very strong magnetic fields with the use of permanent ring magnets, otherwise not practical for spectroscopy because of strong magnetic field gradients. In the micro-cell, however, the B-field inhomogeneity over the narrow atomic vapor column is lower by several orders of magnitude than the applied B values. The magnets were mounted onto two nonmagnetic stages with the possibility of

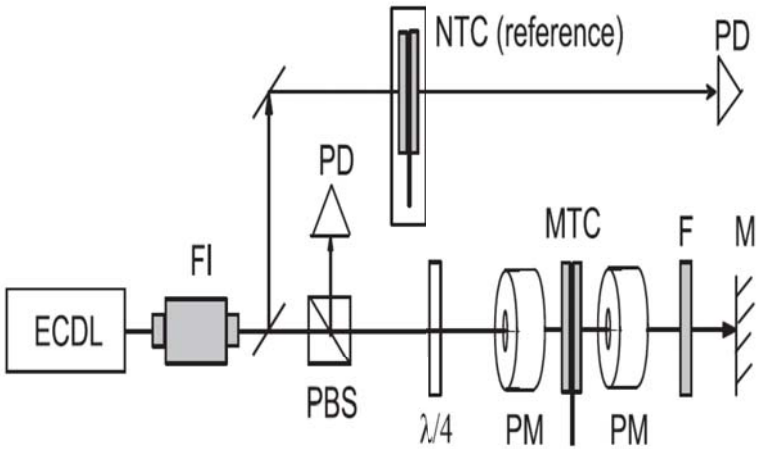

Figure 4.7: Sketch of the experimental setup. ECDL is the diode laser, FI - Faraday isolator, PM - permanent magnet, $\lambda/4$ - quarter waveplate, PBS - polarization beam splitter, PD - photodetectors, F - filter, M - mirror, NC- is the nano-cell to form the reference spectrum.

adjusting their distance. The energy level diagram of the D_1 line of the ^{85}Rb (a) and ^{87}Rb (b) in a magnetic field with the σ^+ atomic transitions of non-vanishing probability in the HPB regime are shown in Fig. 4.6

4.2 Experimental setup

A sketch of the experimental setup is shown in Fig. 4.7. The laser beam from an extended cavity diode laser resonant with the Rb D_1 line ($\lambda = 795$ nm, beam diameter of ~ 1 mm) was directed through the micro-cell with the vapor column thickness of $L \sim 30$ μm. To achieve the σ^+ circular polarization of the laser radiation, we used a polarizing beam splitter followed by a $\lambda/4$ plate. After passing the micro-cell, the beam was retroreflected and the transmission signal was detected by a photodiode and recorded by a digital scope. The micro-cell was heated to ~ 700 °C by a hot air to yield atomic number density of the order of $N = 5 \times 10^{11}$ cm^{-3}. The magnetic field was oriented along the beam propagation direction. A fraction of the laser power was sent to the reference arm with the Rb-filled nano-cell of a thickness $L = \lambda$ or $\lambda/2$ and the transmission spectrum was used as a $B = 0$ frequency reference.

For high magnetic fields $B > 200$ G, the only allowed transitions between magnetic sublevels of the hyperfine states for ^{87}Rb and ^{85}Rb D_1 lines in the case of σ^+ polarized laser excitation are shown in Fig. 4.6. Only four atomic transitions for the ^{87}Rb and six atomic transitions for the ^{85}Rb remain in the transmission spectrum, while there are twelve for the ^{87}Rb and twenty

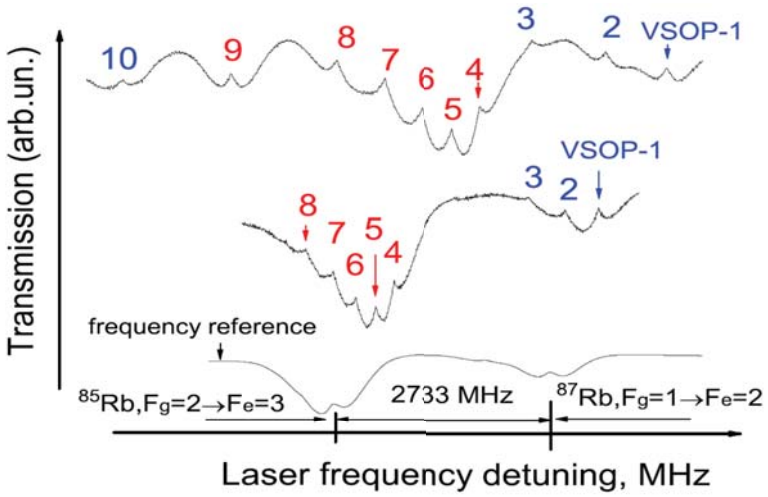

Figure 4.8: Rb D_1 line Saturation Absorption spectrum in the intermediate fields of 1075 G (upper curve) and 500 G (middle curve). Laser power is 5 mW. The lower curve is the reference spectrum recorded with the nano-cell with thickness $L = \lambda$ at zero magnetic field.

for the ^{85}Rb Zeeman transitions allowed at low fields. This strong reduction of the numbers of atomic transitions for large magnetic field is caused by the effect of decoupling of the total electronic momentum J and the nuclear spin momentum I (HPB effect) in the magnetic field $B > B_0$ (see Chapters II and III).

The Saturation Absorption spectra in an external magnetic field recorded with micro-cell in the moderate magnetic fields with the σ^+ polarized laser radiation are shown in Fig. 4.8. Atomic transitions labeled 13 and 10 for ^{87}Rb and 49 for ^{85}Rb (see Fig. 4.6) are clearly resolved and no cross-over resonances are present, thanks to the small thickness of the micro-cell. Our experiment shows that the presented method is applicable for $B \geq 200$ G, which allows the study of the atomic spectra in the intermediate and high fields, i.e., the nonlinear Zeeman and HPB regimes. Examples of high magnetic field Saturation Absorption spectra are shown in Fig. 4.9 together with the spectra obtained in the nano-cells with the thickness $L = \lambda/2$.

Absorption spectra in an external magnetic field are shown in Fig. 4.10 together with the spectra obtained in the nano-cell with the thickness $L = \lambda$ in the case of σ^+ polarized laser excitation. Both techniques based on the use of nano-cells with the thickness $L = \lambda/2$ and $L = \lambda$ allow for observation of the high resolution spectra, and we shortly summarize their advantages. Spectroscopy with the nano-cells (see Chapter III) exploits the strong narrowing in absorption spectrum at $L = \lambda/2$ as compared with the case of an ordinary cm-size vapor cell. Particularly, the absorption linewidth for the Rb D_1 line reduces to $\sim$ 120 MHz (FWHM), as opposed

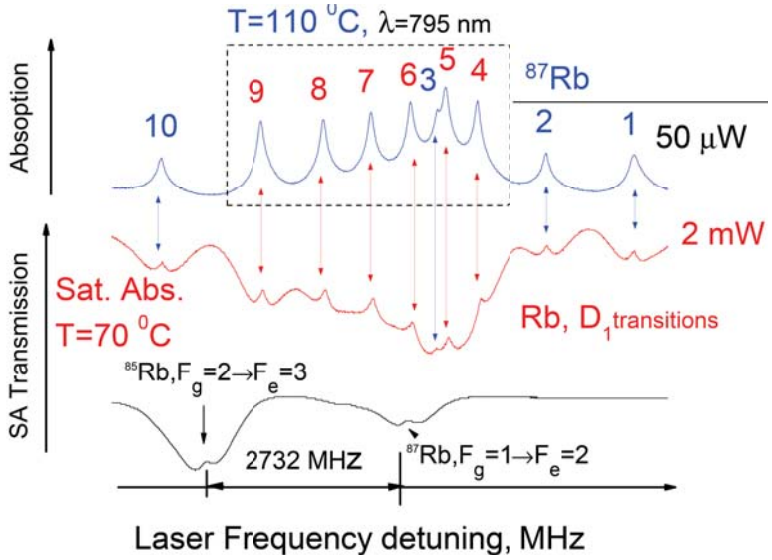

Figure 4.9: Comparison of spectra for $B = 2200$ G obtained with the nano-cell with the thickness $L = \lambda/2$ (upper, blue curve; laser power 50 μW) and Saturation Absorption spectroscopy (middle, red curve) obtained with the micro-meter thin cell (laser power 2 mW). The lower curve is the reference spectrum recorded with the nano-cell with thickness $L = \lambda$ at zero magnetic field.

to $\sim$ 500 MHz Doppler width. Moreover, the relative transition probabilities can be directly extracted from the resonance amplitudes, since the spectrum is essentially background-free. On the other hand, for the nano-cell with $L = \lambda$, the achieved lines are much narrower ($20 - 30$ MHz), which is beneficial for investigation of closely-spaced resonances. The peak amplitudes are again proportional to the transition probability as it was demonstrated in Chapter III, however, the presence of the Doppler background makes them harder to extract.

Fig. 4.11 shows the frequency shift of components 1, 2 and 3 of the ^{87}Rb, D_1 line (the symbols presents the experimental results) obtained with Saturation Absorption spectroscopy with the σ^+ polarized laser radiation as a function of magnetic field B relative to the initial $F_g = 1 \rightarrow F_e = 2$ position at $B = 0$ (see Fig. 4.6 (b)). The solid lines are plotted according the theory presented in Chapter II. For $B \gg B_0$ their frequency slope s (see Eq. (3.2)) asymptotically approaches the same value for the transitions 110, $s \simeq 1.87$ MHz/G. The onset of this value is indicative of the hyperfine Paschen-Back regime. The resonance labelled VSOP-1 is particularly convenient for magnetic field measurements, as it is always located at the high frequency wing of the atomic transition and does not overlap other transitions up to fields of a few Tesla. Its frequency shift can be used to determine the magnetic field strength in the volume defined by the size of the laser beam and the thickness of the micro-cell. This enables

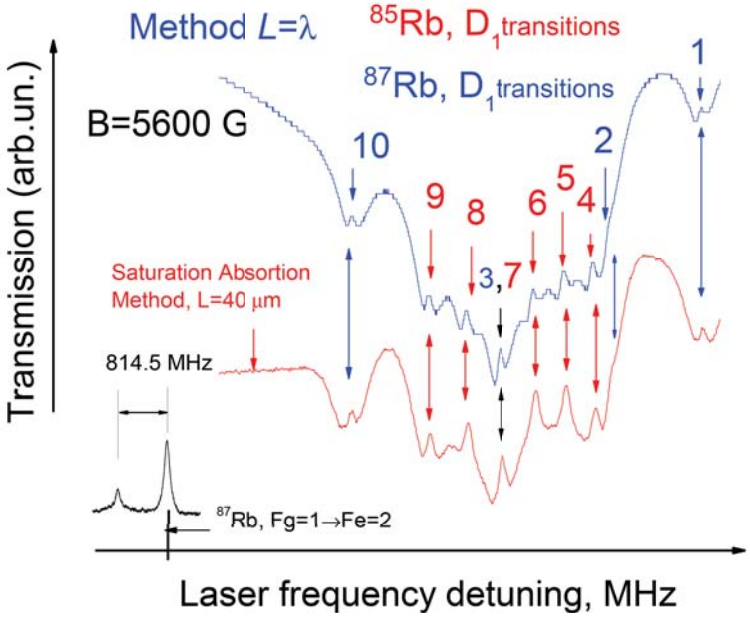

Figure 4.10: Comparison of spectra for $B = 5600$ G obtained with the nano-cell with the thickness $L = \lambda$ (the upper graph) and obtained with Saturation Absorption spectroscopy (middle graph) in the micro-cell with the thickness $L = 40$ μm. Laser power is 5 mW. The lower curve is the zero-field reference shows the fluorescence spectrum of the ^{87}Rb, D_1 line obtained with the nano-cell with the thickness $L = \lambda/2$ at zero magnetic field.

precision field mapping in 1D with a spatial resolution equal to the cell thickness.

It is important to note that the probabilities (i.e. the line intensities) of the atomic transitions labelled 13 and 10 for ^{87}Rb and 49 for ^{85}Rb are increasing with magnetic field increase and tend to the fixed asymptotic values when $B \gg B_0$. Moreover, application of the CCD camera instead of a photodiode in the detection system could simultaneously provide the magnetic-field mapping in the other two dimensions.

In Fig. 4.12 two groups of four curves in the each group plotted by two different models are presented. The four black straight lines labelled (1), (2), (3) and (10) are plotted according to Eq. (3.1) which is valid for $B \gg B_0$ (^{87}Rb). The four red curves labelled $1-3$ and 10 are plotted according to the theoretical model presented in Chapter II.

The values for the fine structure (g_J) and the nuclear (g_I) Landé factors and the hyperfine constants A_{hfs} for ^{87}Rb and ^{85}Rb are given in [141, 142].

As it is seen the largest difference between the two models is achieved for the two curves labelled 2 and (2) (the difference of the frequencies shifts at 10 kG is 2.8%). Such relatively large difference (note, that in the case of ^{39}K the difference between the two models at 1 kG was less than 1%, see Fig. 3.11) is caused by a large value of B_0 (^{87}Rb)$\simeq$ 2.4 kG. That's

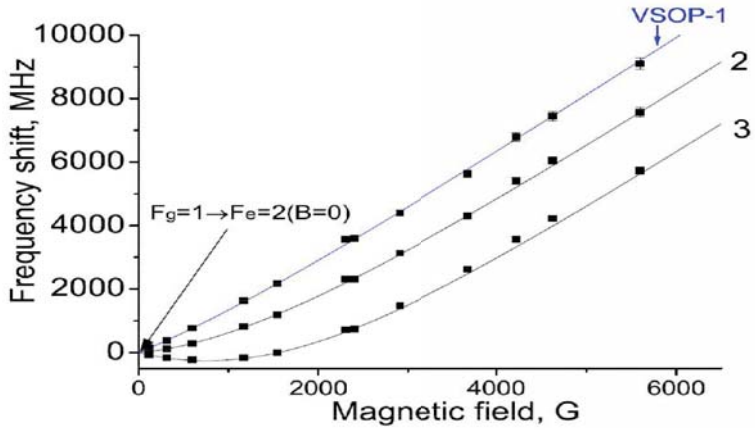

Figure 4.11: Frequency shifts of the resonances labeled 13 [see Fig. 4.6 (b)] in the magnetic field. Solid lines represent the theory presented in Chapter II. The symbols presents the experimental results measured with Saturation Absorption spectroscopy in a 40 μm-long micro-cell with the σ^+ polarized laser radiation.

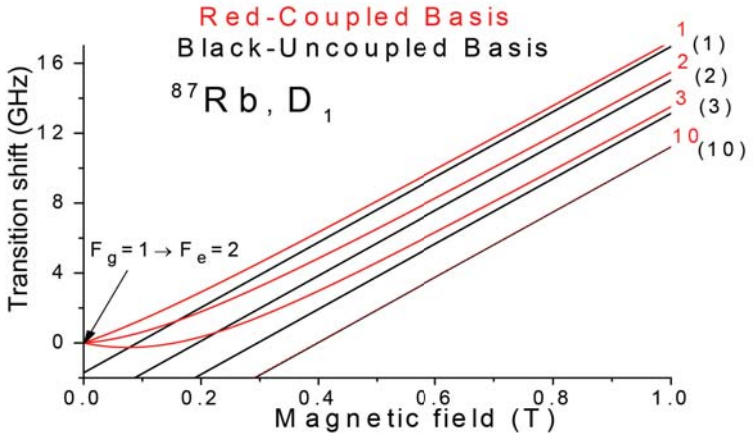

Figure 4.12: Two groups of four curves in the each group for ^{87}Rb, D_1 line plotted by two different models are presented. The four black straight lines labeled (1), (2), (3) and (10) are plotted according the formula (3.1) which is valid for $B \gg B_0$ (^{87}Rb). The four red curves labeled $1-3$ and 10 are plotted according to the theoretical model presented in Chapter II.

why the condition $B \gg B_0$ (^{87}Rb) is fulfilled for $B > 10$ kG. It is worth to note that for the atomic transition labelled 10 (10) the curves coincides, thus the frequency position of transition labelled 10 could be plotted using formula (3.1).

As it was mentioned in the Chapter III , for $B \gg B_0$ the momenta J and I are decoupled (HPB regime), the eigenstates of the Hamiltonian are described in the uncoupled basis of J and I projections $(m_J; m_I)$. Fig. 4.13 shows six atomic transitions of ^{85}Rb labelled $4-9$ and four atomic transitions of ^{87}Rb labeled $1-3$ and 10 for the case of σ^+ polarized laser excitation in the hyperfine Paschen-Back regime.

Long-term stabilization of a laser frequency is routinely achieved by electronic locking of the

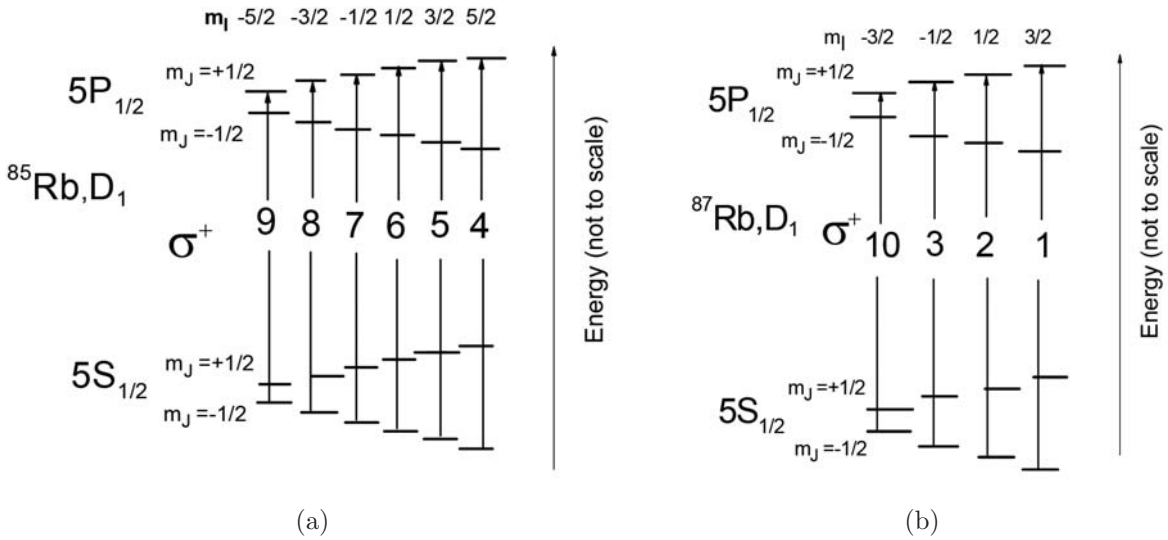

(a) (b)

Figure 4.13: Diagram of ^{85}Rb D_1 line transitions (left one) and diagram of ^{87}Rb D_1 line transitions (right one) in hyperfine Paschen-Back regime for σ^+ polarized laser excitation. The selection rules are $\Delta m_J = 1; \Delta m_I = 0$. As it is seen there are six atomic transitions of ^{85}Rb labeled $4-9$ and four atomic transitions of ^{87}Rb labeled $1-3$ and 10, which coincides with the experimental results presented in Fig. 4.9 and 4.10.

laser to an appropriate spectroscopic reference signal. For many atomic physics experiments, the light frequency has to be detuned from the exact resonance by some GHz, e.g. to avoid absorption and exploit the dispersive properties of the medium or to precisely control the AC-Stark shifts introduced by the detuned beam [143]. In some cases the other isotope lines can be used to stabilize the laser frequency or the beat-note signal of the two lasers can be used for offset lock. The latter, however, requires two lasers, and is practically limited to around 10 GHz detunings. Here we propose a simple atomic frequency reference system which consists of MC with $L = 40$ μm and two permanent ring magnets separated by a plastic spacer. The heating of the micro-cell is provided by a simple hot air blower. For the 15 mm spacer, the achieved field value is $B = 5.6$ kG and the VSOP-1 resonance for σ^+ excitation is shifted by 9.2 GHz with respect to its $B = 0$ position (Fig. 4.14). For σ excitation a similar resonance can be used in the low frequency wing of the spectrum. Thus, by changing the spacer thickness and light polarization it is possible to form the frequency reference in a wide frequency range, limited by the strength of available magnets. Thanks to the narrowness of the MC the accuracy of such a reference does not suffer from field inhomogeneities. We have verified that although for $B > 2$ kG there are twenty transitions in the Rb D_2 line (for either σ^+ or π polarization), the method could be implemented successfully also for that line. Figure 4.14 illustrates the stabilization

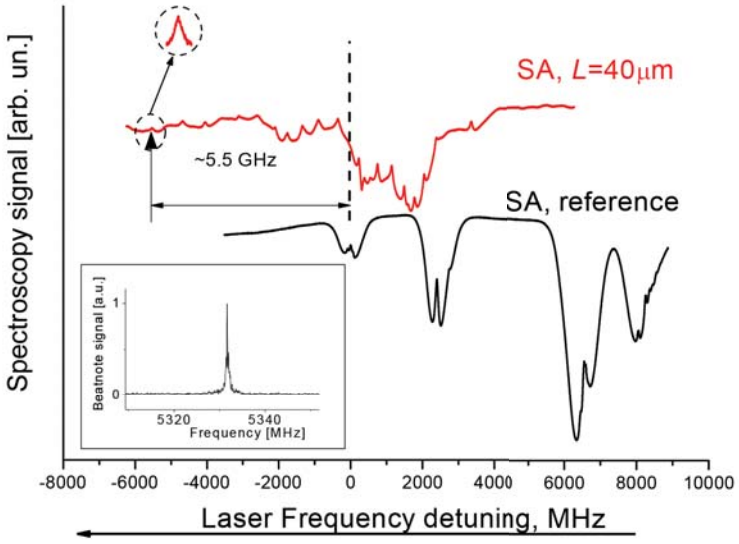

Figure 4.14: SA spectrum of the rubidium D_2 line in the MC in $B = 2.2$ kG (upper red curve). Bottom (black) trace is the reference cell spectroscopy in $B = 0$. The resonance indicated by the dashed line was used for frequency stabilization of the diode laser. The inset graph shows the beat-note signal against a second, frequency-locked (dotted line) laser.

of a tunable laser frequency to the magnetically shifted resonance.The beatnote signal against the reference laser, frequency locked 196 MHz below the ^{87}Rb $F_g = 2 \rightarrow F_e = 3$ transition, demonstrates the feasibility of over 5 GHz laser detuning to the frequency where no resonance is present at $B = 0$.

4.3 Comparison of the benefits of using nano- or micro-cells filled with alkali metal

In Chapter III it has been demonstrated that the use of the nano-cells with the thickness of $L = \lambda/2$ and $L = \lambda$ is very convenient for the study of the atomic transitions parameters (i.e. the frequencies shifts and probabilities) in a strong magnetic fields. In Chapter IV we have demonstrated that use of micro-cells with the thickness $L = 30 - 40$ μm is also very convenient for this purpose. Let us compare the advantages and drawbacks of micro-cells and nano-cells. First, it should be noted that the manufacture of the nano-cells is a much more technically complicated task, since it is necessary to provide broad regions between inner walls of windows with gap thicknesses of one wavelength and/or half-wavelength (see Chapter I). In contrast,

for micro-cells it is sufficient to arrange thin platinum strips (gaskets) with dimensions of 0.5 mm $\times$ 2 mm and calibrated thickness ($10 - 50$ μm) between the inner walls of windows). The advantages of micro-cells include a relatively low working temperature ($60 - 70$ °C), which allows an experimental setup of glass parts chemically resistant to hot alkali metal vapors below 100 °C. In order to realize Saturation Absorption technique one needs to form two propagating laser beans (a pump beam and a probe beams), while in the case of nano-cell use one single beam transmission is enough, thus the setup is more simple and a needed laser power is lower.

4.4 Assembled single unit Frequency Reference

For applications it is more convenient to combine the permanent magnets, mirror and micrometer cell filled with the alkali metal in a single unit that can be easily moved, adjusted, and employed. This assembly is shown in Fig. 4.15. The Rb mico-cell is placed between permanent magnets and is heated with hot air from above. In this case the temperature of the micro-cell windows must be higher than the temperature at the side-arm (in order to prevent the Rb vapor condensation on the windows). By changing the spacer thickness (for which a convenient nonmagnetic, thermostable, hard but quite readily processed material is "caprolon"), it is possible to construct a convenient frequency reference with narrow VSOPs shifted relative to the initial atomic levels (in zero field) up to $15 - 20$ GHz. This reference may be convenient, particularly, for determining the frequencies of molecular transitions in the complex spectra of dimers such as K_2, Rb_2 and Cs_2. For a spacer thickness of about 10 mm, the spectrum appears as in Fig. 4.10. Note that the magnetic field at a distance of $40 - 50$ cm from the unit shown in Fig. 4.15 drops to almost zero and does not influence operation of the other parts of the experimental setup.

4.5 Summary

In this Chapter we have demonstrated successful implementation of Saturation Absorption spectroscopy based on micro-cells with the thickness $L = 30 - 40$ μm for Doppler-free studies of atomic transitions in a wide region of magnetic fields, from 0.2 up to 6 kG. This is mainly

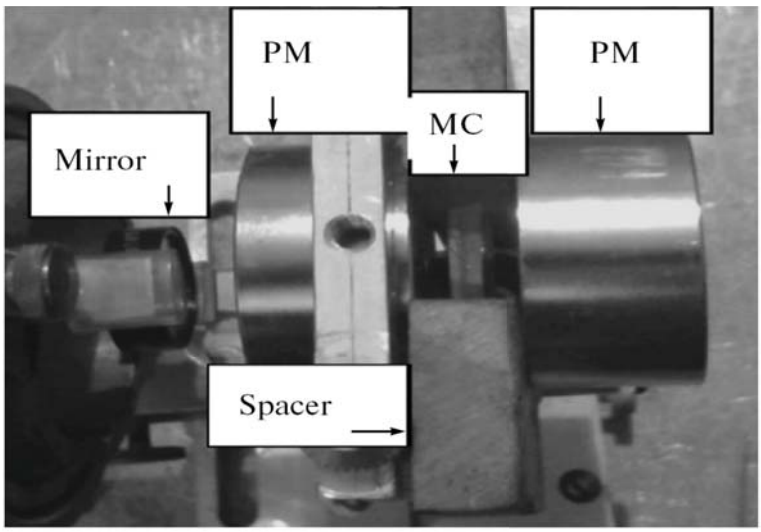

Figure 4.15: Assembled unit containing Rb micro-cell with thickness $L = 40$ μm (MC), permanent ring magnets (PM) with a small hole of $\sim$ 2 mm in diameter for the laser beam transmission, hard-spacer (the thickness could be varying in the range of 1-4 cm), and mirror for Saturation Absorption technique realization.

due to elimination of crossovers in the thin cell and the resulting simplification of the atomic spectra. By using circularly polarized light, the number of atomic transitions that are spectrally resolved is lowered to four D_1 line atomic transitions of ^{87}Rb and six atomic transitions of ^{85}Rb. The system based on a micro-cell and two permanent magnets is proposed as a tunable atomic frequency reference with a tuning range of the order of $10 - 15$ GHz around the zero-magnetic-field optical transition frequencies, limited by the currently available magnets. Relatively simple manufacturing of the micro-cells filled with alkali metal (as compared with nano-cells) is advantageous for practical implementation of the proposed method. The micro-cells are universal and can be used for large field spectroscopy or the optical magnetometry with a micrometric spatial resolution, important for mapping strongly inhomogeneous magnetic fields.

Conclusion

We proposed a robust, compact permanent magnet based device, which allows the investigation of saturation absorption (SA) in strong (> 100 G) magnetic fields. The use of micro-cell in this device prevents the appearance of the crossovers, which destruct the SA signal in strong magnetic fields. Therefore, it permits the observation of only the real transitions.

It has been shown the existence of so-called Guiding Transitions (GT) in magnetic fields for alkali metals. The GT in magnetic fields maintains its probability and frequency slope. All other transitions' probabilities and slopes in its groups tend to the GT's probability and slope. Knowledge of the GT's properties allows to predict all other transitions' behavior in magnetic fields.

Using a half-wave-thick cell (the thickness along the beam propagation axis $L = 426$ nm for ^{133}Cs) we observed experimentally magnetic field-induced giant modification of the probabilities of $6S_{1/2},\ F_g = 3 \rightarrow 6P_{3/2},\ F_e = 5$ transitions (these transitions are forbidden in zero magnetic field) of the Cs D_2 line. In the case of circularly σ^+ polarized laser radiation, the probabilities of seven transitions $F_g = 3,\ m_F = -3, -2, -1, 0, +1, +2, +3 \rightarrow F_e = 5,$ $m_F = -2, -1, 0, +1, +2, +3, +4$ (the selection rule is $\Delta m_F = +1$) increase dramatically and the probabilities of two transitions (out of this seven) become the largest among all other in a wide-range of magnetic fields $200 - 3200$ G. Hence, 7 new transitions in external magnetic fields have been studied.

It has been also shown that the use of a nano-cell in the studies of the behavior of the alkali atoms in external strong (up to 8000 G) magnetic fields allows the direct measurements of the transitions' probabilities and slopes.

Bibliography

Papers included in the thesis

[1] A. Sargsyan, A. Tonoyan, G. Hakhumyan, A. Papoyan, E. Mariotti, D. Sarkisyan "Giant modification of atomic transitions probabilities induced by magnetic field: forbidden transitions become predominant" Laser Phys. Lett., 11, 055701 (2014).

[2] A. Sargsyan, A. Tonoyan, R. Mirzoyan, D. Sarkisyan, A. Wojciechowski, W. Gawlik "Saturated-absorption spectroscopy revisited: atomic transitions in strong magnetic fields ($>$ 20 mT) with a micrometer-thin cell" Opt. Lett., 39, 2270 (2014).

[3] A. Sargsyan, A. Tonoyan, H. Hakhumyan, Y. Pashayan- Leroy, C. Leroy, D. Sarkisyan "Atomic transitions of Rb, D_2 line in strong magnetic fields: hyperfine Paschen-Back regime" Opt. Comm., 334, 208 (2015).

[4] A. Sargsyan, A. Tonoyan, G. Hakhumyan, C. Leroy, Y. Pashayan-Leroy and D. Sarkisyan "Complete hyperfine Paschen-Back regime at relatively small magnetic fields realized in potassium nano-cell" Europhys. Lett., 110, 23001 (2015).

[5] A. Sargsyan, G. Hakhumyan, A. Tonoyan, P. A. Petrov, and T. A. Vartanyan "Study of the Rb D_2 Line Splitting in a Strong Transverse Magnetic Field with Doppler-Free Spectroscopy in a Nanocell" Opt. and Spectr., 119, 202 (2015).

[6] A.Y. Tonoyan "Theoretical Investigation of ^{41}K States Behavior under Strong Magnetic Field and π Polarized Laser Field" Reports NAS RA, 116, 48 (2016).

Conference theses and abstracts

[7] A. Tonoyan, A. Sargsyan, G. Hakhumyan, Y. Pashayan-Leroy, C. Leroy, D. Sarkisyan "Behaviour of atomic transitions of Rb, D_2 line in strong magnetic fields" EGAS 46, LILLE, FRANCE, July 1-4, 2014 Book of Abstracts, P-26, page 84.

[8] A. Tonoyan, A. Sargsyan, G. Hakhumyan, C. Leroy, Y. Pashayan-Leroy, and D. Sarkisyan "Study of atomic transitions of ^{39}K isotope on D_1 line in strong magnetic fields" EGAS 47, RIGA, LATVIA, July 14-17, 2015 Book of Abstracts, P-40, page 106.

[9] A. Amiryan, A. Sargsyan, A. Tonoyan, Y. Pashayan-Leroy, C. Leroy, and D. Sarkisyan "Study of Atomic Transitions of Rb D_2 line in Strong Transverse Magnetic Fields by an Optical Half-Wavelength Cell" EGAS 47, RIGA, LATVIA, July 14-17, 2015 Book of Abstracts, P-41, page 107.

[10] A.Sargsyan, G. Hakhumyan, A.Tonoyan, D. Sarkisyan "Behavior of ^{39}K atoms transitions on D_1 line in external magnetic field" QuantArm2014 International Conference and Workshop, Yerevan-Tsaghkadzor, Armenia, September 22-26, Book of Abstracts, page 38.

[11] A. Tonoyan, A. Sargsyan, G. Hakhumyan, D. Sarkisyan,"Study of Cs D_2 Line, $F_g = 3 \rightarrow F_e = 5$ atomic transitions in a strong external magnetic field" QuantArm 2014 International Conference and Workshop, Yerevan-Tsaghkadzor, Armenia, September 22-26, Book of Abstracts, page 60.

[12] R. Mirzoyan, A. Tonoyan, A. Sargsyan, D. Sarkisyan "Saturated-absorption spectroscopy in Rb filled micrometer-thin cell: Applications in strong magnetic fields" QuantArm 2014 International Conference and Workshop, Yerevan-Tsaghkadzor, Armenia, September 22-26, Book of Abstracts, page 53.

[13] C. Leroy, Y. Pashayan-Leroy, A. Sargsyan, A. Tonoyan, G. Hakhumyan, D. Sarkisyan, "On decoupling of total electronic angular momentum and nuclear spin for ^{39}K atom" High Resolution Molecular Spectroscopy (HRMS), DIJON, FRANCE, August 24-28, Book of Abstracts, page 103.

Cited literature

[14] E. Arimondo "Coherent population trapping in laser spectroscopy" in Progress in optics, ed. by E. Wolf (Elsevier Science, Amsterdam 1996), 35, 257 (1996).

[15] R.Wynands, A.Nagel "Precision spectroscopy with coherent dark states" Appl. Phys. B, 68, 1 (1999).

[16] D. Budker, W. Gawlik, D. Kimball, S. R. Rochester,V. V. Yaschuk, and A. Weis "Resonant nonlinear magneto-optical effects in atoms" Rev. Mod. Phys. 74, 1153 (2002).

[17] V.V. Yashchuk, D. Budker, W. Gawlik, D.F. Kimball, Yu.P. Malakyan, and S.M. Rochester "Selective Addressing of High-Rank Atomic Polarization Moments" Phys. Rev. Lett., 90, 253001 (2003).

[18] D. Budker, D. F. Kimball, and D. P. DeMille "Atomic Physics: An Exploration through Problems and Solutions" Oxford Univ. Press (2004).

[19] D. Meschede "Optics, Light and Lasers: The practical Approach to Modern Aspects of Photonics and Laser Physics" WILEY-VCH Verlag GmbH&Co. KGaA, Weinheim, 2nd ed. (2004).

[20] J. Vanier "Atomic clocks based on coherent population trapping: a review" Appl. Phys. 81, 421 (2005).

[21] M. Fleischhauer, A. Imamoglu, J. P. Marangos "Electromagnetically induced transparency: Optics in Coherent Media" Rev. Mod. Phys., 77, 633 (2005).

[22] D. Budker and M. Romalis "Optical magnetometry" Nat. Phys., 3, 227 (2007).

[23] R. W. Boyd and P. Narum "Slow - and fast - light: fundamental limitations" J. Mod. Opt. 54, 2403 (2007).

[24] M. Auzinsh, D. Budker, and S.M. Rochester "Optically Polarized Atoms: Understanding Light - Atom Interactions" Oxford Univ. Press, Oxford (2010).

[25] A.Ch. Izmailov "On the possibility of detecting the sub - Doppler structure of spectral lines of gas particles by a single traveling monochromatic wave" Las. Phys., 2, 762 (1992).

[26] T.A. Vartanyan, D. Lin "Enhanced selective reflection from a thin layer of a dilute gaseous medium" Phys. Rev. A, 51, 1959 (1995).

[27] S. Briaudeau, D. Bloch, M. Ducloy "Detection of slow atoms in laser spectroscopy of a thin vapor film" Europhys. Lett., 35, 337 (1996).

[28] B. Zambon, G. Nienhuis "Reflection and transmission of light by thin vapor layers", Opt. Comm., 143, 308 (1997).

[29] S. Briaudeau, S. Saltiel, G. Nienhuis, D. Bloch, M. Ducloy "Coherent Doppler narrowing in a thin cell: observation of the Dicke regime in the optical domain" Phys. Rev. A, 57, R3169 (1998).

[30] S. Briaudeau, D. Bloch, M. Ducloy "Sub - Doppler spectroscopy in a thin film of resonant vapor" Phys. Rev. A 59, 3723 (1999).

[31] S. Briaudeau, S. Saltiel, M. Oria, A.Weis, D. Bloch, M. Ducloy "Recent developments in sub - Doppler spectroscopy in a thin cell" J. Phys. IV 10, Pr8-145 (2000).

[32] B. Ai, D. S. Glassner, R. J. Knize, J. P. Partanen "A thin atomic vapor as a nonlinear optical medium" Appl. Phys. Lett. 64, 951 (1994).

[33] D.S. Glassner, B. Ai , R.J. Knize "Low - intensity degenerate four - wave mixing at the cesium D_1 resonance in thin cells" Opt. Lett., 19, 2071 (1994).

[34] B. Ai, D.S. Glassner, R.J. Knize "Enhancement of degenerate four - wave mixing by atom - wall collisions in atomic vapors" Phys. Rev. A, 50, 3345 (1994).

[35] S. Knappe, L. Hollberg, J. Kitching "Dark Line Resonances in Sub - Millimeter Structures" Opt. Lett., 29, 388 (2004).

[36] L.A. Liew, S. Knappe, J. Moreland, H.G. Robinson, H. Hollberg, J. Kitching "Microfabricated alkali atom vapor cells" Appl. Phys. Lett., 84, 2694 (2004).

[37] S. Knappe, P. Schwindt, V. Shah, L. Hollberg, J. Kitching, L. Liew, J. Moreland "A chip - scale atomic clock based on ^{87}Rb with improved frequency stability" Opt. Express, 13, 1249 (2005).

[38] S. Knappe, H. G. Robinson, and L. Hollberg "Microfabricated saturated absorption laser spectrometer" Optics Express, 15, 6293 (2007).

[39] T. Baluktsian, C. Urban, T. Bublat, H. Giessen, R. Low, T. Pfau "Fabrication method for microscopic vapor cells for alkali atoms" Opt. Lett. 35, 1950 (2010).

[40] D. Sarkisyan, D. Bloch, A. Papoyan, M. Ducloy "Sub - Doppler spectroscopy by sub - micron thin Cs vapour layer" Opt. Comm., 200, 201 (2001).

[41] G. Dutier, S. Saltiel, D. Bloch, M. Ducloy "Revisiting optical spectroscopy in a thin vapor cell: mixing of reflection and transmission as a Fabry-Perot microcavity effect" J. Opt. Soc. Am. B, 20, 793 (2003).

[42] D. Sarkisyan, T. Becker, A. Papoyan, P. Thoumany, H. Walther "Sub - Doppler fluorescence on the atomic D_2 line of a submicron rubidium - vapor layer" Appl. Phys. B, 76, 625 (2003).

[43] G. Dutier, A. Yarovitski, S. Saltiel, A. Papoyan, D. Sarkisyan, D. Bloch, M. Ducloy "Collapse and revival of a Dicke - type coherent narrowing in a sub - micron thick vapor cell transmission spectroscopy" Europhys. Lett., 63, 35 (2003).

[44] D. Sarkisyan, T. Varzhapetyan, A. Sarkisyan, Y. Malakyan, A. Papoyan, A. Lezama, D. Bloch, M. Ducloy "Spectroscopy in an extremely thin vapor cell: Comparing the cell - length dependence in fluorescence and in absorption techniques" Phys. Rev. A, 69, 065802 (2004).

[45] G. V. Nikogosyan, D. G. Sarkisyan, Yu. P. Malakyan "Absorption of resonance radiation and fluorescence of a layer of an atomic gas with thickness of the order of a wavelength" J. of opt. tech., 71, 602 (2004).

[46] T. Varzhapetyan, D. Sarkisyan, L. Petrov, C. Andreeva, D. Slavov, S. Saltiel, A. Markovski, G. Todorov, S. Cartaleva "Sub - Doppler spectroscopy and coherence resonances in submicron Cs vapour layer" 13th International School on Quantum Electronics: Las. Phys. and Applic., 196 (2005).

[47] D. Sarkisyan, T. Varzhapetyan, A. Papoyan, D. Bloch, M. Ducloy "Absorption and fluorescence in atomic submicron cell: high laser intensity case" ICONO 2005: Nonlinear Laser Spectroscopy, High Precision Measurements, and Laser Biomedicine and Chemistry, 625701-625701-5 (2006).

[48] C. Andreeva, S. Cartaleva, L. Petrov, S. Saltiel, D. Sarkisyan, T. Varzhapetyan, D. Bloch, M. Ducloy "Saturation effects in the sub - Doppler spectroscopy of cesium vapor confined in an extremely thin cell" Phys. Rev. A, 76, 013837 (2007).

[49] A. Sargsyan, D. Sarkisyan, A. Papoyan, Y. Pashayan-Leroy, P. Moroshkin, A. Weis, A. Khanbekyan, E. Mariotti, L. Moi "Saturated absorption spectroscopy: Elimination of crossover resonances with the use of a nanocell" Las. Phys., 18, 749 (2008).

[50] T. Varzhapetyan, A. Nersisyan, V. Babushkin, D. Sarkisyan, S. Vdovi, G. Pichler "Study of atomic transition self - broadening and shift with the help of a nano-cell" J. of Phys. B: Atomic, Mol. and Opt. Phys., 41, 185004 (2008).

[51] V. Biancalana, S. Cartaleva, Y. Dancheva, P. Gosh, E. Mariotti, S. Mitra, L. Moi, N. Petrov, B. Ray, D. Sarkisyan, D. Slavov "Population loss in closed optical transitions of Rb and Cs atoms confined in micrometric thin cells" Acta Physica Polonica-Series A Gen. Phys., 19, 495 (2009).

[52] S. Cartaleva, S. Saltiel, A. Sargsyan, D. Sarkisyan, D. Slavov, P. Todorov, K. Vaseva "Sub - Doppler spectroscopy of cesium vapor layers with nanometric and micrometric thickness" JOSA B, 26, 1999 (2009).

[53] G. Hakhumyan, A. Sargsyan, C. Leroy, Y. Pashayan-Leroy, A. Papoyan, D. Sarkisyan "Essential Features of Optical Processes in Rb submicron Thin Cell Filled with Neon Gas" Opt. Express, 18, 14577 (2010).

[54] D. Sarkisyan, A. Papoyan "Formation of Narrow Optical Resonances using submicron - thin atomic vapor layer" Modern Optics and Photonics. Atoms and Structured Media, 257 (2010).

[55] S.Cartaleva, A. Sargsyan, D. Sarkisyan, D. Slavov, K. Vaseva "New narrow resonance in the fluorescence of closed optical transition observed in nanometric Cs - vapor layers" XVI International School on Quantum Electronics: Laser Physics and Applications, 77470H-77470H-8 (2010).

[56] L. Kalvans, M. Auzinsh, R. Ferber, F. Gahbauer, A. Jarmola, A. Papoyan, D. Sarkisyan "Modelling magneto - optical resonances in atomic rubidium at D_1 excitation in extremely thin cells while maintaining a self - consistent set of theoretical parameters" Modern Optics and Photonics. Atoms and Structured Media, 289 (2010).

[57] D. Sarkisyan, G. Hakhumyan, A. Sargsyan, R. Mirzoyan, C. Leroy, Y. Pashayan-Leroy "Laser spectroscopy with nanometric cells containing atomic vapor of metal: influence of buffer gas" XVI International School on Quantum Electronics: Laser Physics and Applications, 77470C-77470C-15 (2010).

[58] S. Cartaleva, A. Krasteva, A. Sargsyan, D. Sarkisyan, D. Slavov, T. Vartanyan "High resolution spectroscopy of Cs vapor confined in optical cells of few - micron thicknesses" J. of Phys.: Conference Series, 397, 012062 (2010).

[59] S. Cartaleva, A. Krasteva, A. Sargsyan, D. Sarkisyan, D. Slavov, K. Vaseva, P. Todorov "High resolution laser spectroscopy of cesium vapor layers with nanometric thickness" INTECH Open Access Publisher (2012).

[60] J. Keaveney, I. Hughes, A. Sargsyan, D. Sarkisyan, C. Adams "Maximal refraction and superluminal propagation in a gaseous nanolayer" Phys. Rev. Lett., 109, 233001 (2012).

[61] S. Cartaleva, A. Krasteva, L. Moi, A. Sargsyan, D. Sarkisyan, D. Slavov, P. Todorov, K. Vaseva "Laser spectroscopy of sub - micrometre - and micrometre - thick caesium - vapour layers" Quantum Electronics, 43, 875 (2013).

[62] K. Whittaker, J. Keaveney, I. Hughes, A. Sargysyan, D. Sarkisyan, B. Gmeiner, V. Sandoghdar, C. Adams "Interrogation and fabrication of nm scale hot alkali vapour cells" Journal of Physics: Conference Series 635, 122006 (2015).

[63] K. Whittaker, J. Keaveney, I. Hughes, A. Sargsyan, D. Sarkisyan, C. Adams "Spectroscopic detection of atom-surface interactions in an atomic - vapor layer with nanoscale thickness" Phys. Rev. A, 92, 052706 (2015).

[64] A. Sargsyan, Y. Pashayan-Leroy, C. Leroy, D. Sarkisyan "Collapse and revival of a Dicke - type coherent narrowing in potassium vapor confined in a nanometric thin cell" Journal of Physics B: Atomic, Mol. and Opt. Phys., 49, 075001 (2016).

[65] D. Bloch, M. Ducloy, N. Senkov, V. Velichansky, and V. Yudin "Doppler-Free Spectroscopy of the D1 Line of Potassium" Las. Phys., 6, 670 (1996).

[66] G. Dutier, S. Saltiel, D. Bloch, M. Ducloy, A. Papoyan, D. Sarkisyan "Observation of atom - surface interaction in a submicrometric vapor cell" J. de Phis. IV, 12, 155 (2002).

[67] G. Dutier, A. Yarovitski, S. Saltiel, D. Sarkisyan, A. Papoyan, T. Varzhapetyan, D. Bloch, M. Ducloy "Spectroscopy in a sub - micrometer thick cell or how to probe the atom - surface interaction with a nanometric spatial resolution" J. de Phys. IV (Proceedings), 119, 179 (2004).

[68] G. Dutier, I. Hamdi, P. Segundo, A. Yarovitski, S. Saltiel, M-P Gorza, M. Fichet, D. Bloch, M. Ducloy, D. Sarkisyan, A. Papoyan, T. Varzhapetyan "Coupling of atoms, surfaces and fields in dielectric nanocavities" Las. Spectr., 1, 277 (2004).

[69] I. Maurin, P. Todorov, I. Hamdi, A. Yarovitski, G. Dutier, D. Sarkisyan, S. Saltiel, M-P Gorza, M. Fichet, D. Bloch, M. Ducloy "Probing an atomic gas confined in a nanocell" J. of Phys.: Conference Series, 19, 20 (2005).

[70] M. Fichet, G. Dutier, A. Yarovitsky, P. Todorov, I. Hamdi, I. Maurin, S. Saltiel, D. Sarkisyan, M-P Gorza, D.Bloch, M. Ducloy "Exploring the van der Waals atom - surface attraction in the nanometric range" Europhys. Lett., 77, 54001 (2007).

[71] V. Khromov, A. Logunov, A. Pazgalev, S. Przhibel'skii, D. Sarkisyan, T. Vartanyan "Spectroscopy of the atom-wall interactions in a nanocell" J. of Phys.: Conference Series, 397, 012063 (2012).

[72] J. Keaveney, A. Sargsyan, U. Krohn, I. Hughes, D. Sarkisyan, C. Adams "Cooperative lamb shift in an atomic vapor layer of nanometer thickness" Phys. Rev. Lett., 108, 173601 (2012).

[73] T. Vartanyan, A. Logunov, A. Pazgalev, S. Przhibelskii, D. Sarkisyan, V. Khromov "Change in the states of optically excited Rb atoms near sapphire surface" Opt. and Spectr., 115, 60 (2013).

[74] A. Pazgalev, D. Sarkisyan, S. Cartaleva, S. Przhibel'skii, T. Vartanyan "Ultra - narrow spectroscopic cells in atomic spectroscopy: reflection, transmission, fluorescence, and nonadiabatic transitions at the walls" J. of Phys.: Conference Series, 548 , 012063 (2014).

[75] K. Whittaker, J. Keaveney, I. Hughes, A. Sargsyan, D. Sarkisyan, C. Adams "Optical response of gas - phase atoms at less than $\lambda/80$ from a dielectric surface" Phys. Rev. lett., 112, 253201 (2014).

[76] J-M Hartmann, X. Landsheere, C. Boulet, D. Sarkisyan, A. S. Sarkisyan, C. Leroy, E. Pangui "Infrared look at the spectral effects of submicron confinements of CO_2 gas" Phys. Rev. A, 93, 012516 (2016).

[77] D. Sarkisyan, A. Papoyan, T. Varzhapetyan, J. Alnis, K. Blush, M. Auzinsh "Sub - Doppler spectroscopy of Rb atoms in a sub - micron vapour cell in the presence of a magnetic field" J. of Opt. A: Pure and Appl. Opt. 6, S142 (2004).

[78] D. Sarkisyan, A. Papoyan, T. Varzhapetyan, K. Blush, M. Auzinsh "Zeeman effect on the hyperfine structure of the D_1 line of a submicron layer of ^{87}Rb vapor" Opt. and Spectr., 96, 328 (2004).

[79] D. Sarkisyan, A. Papoyan, T. Varzhapetyan, K. Blushs, M. Auzinsh "Fluorescence of rubidium in a submicrometer vapor cell: spectral resolution of atomic transitions between Zeeman sublevels in a moderate magnetic field" JOSA B, 22, 88 (2005).

[80] E. Gazazyan, A. Papoyan, D. Sarkisyan, A. Weis "Laser frequency stabilization using selective reflection from a vapor cell with a half - wavelength thickness" Las. Phys. Lett., 4, 801 (2007).

[81] A. Sargsyan, G. Hakhumyan, A. Papoyan, D. Sarkisyan, A. Atvars,and M. Auzinsh "A novel approach to quantitative spectroscopy of atoms in a magnetic field and applications based on an atomic vapor cell with $L = \lambda$" Appl. Phys. Lett. 93, 021119 (2008).

[82] M. Auzinsh, R. Ferber, F. Gahbauer, A. Jarmola, L. Kalvans, A. Papoyan, D. Sarkisyan "Nonlinear magneto - optical resonances at D_1 excitation of ^{85}Rb and ^{87}Rb in an extremely thin cell" Phys. Rev. A, 81, 033408 (2010).

[83] G. Hakhumyan, D. Sarkisyan, A. Sargsyan, A. Atvars, M. Auzinsh "Investigation of Rb D_1 atomic lines in strong magnetic fields by fluorescence from a half - wave - thick cell" Opt. and Spectr. 108, 685 (2010).

[84] G. Hakhumyan, A. Sargsyan, C. Leroy, Y. Pashayan-Leroy, D. Sarkisyan "Study of Rb atomic transitions $D_{1,2}$ lines in strong magnetic field based on fluorescence spectra of sub - micron thin cell" International Conference on Laser Physics 2010, 79980V-79980V-8 (2010).

[85] G. Hakhumyan, C. Leroy, Y. Pashayan-Leroy, D. Sarkisyan, M. Auzinsh "High - spatial - resolution monitoring of strong magnetic field using Rb vapor nanometric - thin cell" Opt. Comm., 284, 4007 (2011).

[86] A. Sargsyan, G. Hakhumyan, D. Sarkisyan "Use of sub - Doppler optical resonances for measurement of weak magnetic fields by means of extremely thin rubidium vapor cell" J. of Contemp. Phys. (Arm. Acad. of Sci.) 47, 64 (2012).

[87] G. Hakhumyan, C. Leroy, R. Mirzoyan, Y. Pashayan-Leroy, D. Sarkisyan "Study of "forbidden" atomic transitions on D_2 line using Rb nano - cell placed in external magnetic field" The Eur. Phys. J. D, 66, 1 (2012).

[88] A. Sargsyan, G. Hakhumyan, C. Leroy, Y. Pashayan-Leroy, A. Papoyan, D. Sarkisyan "Hyperfine Paschen-Back regime realized in Rb nanocell" Opt. lett., 37, 1379 (2012).

[89] A. Sargsyan, R. Mirzoyan, D. Sarkisyan "Splitting of the electromagnetically induced transparency resonance on ^{85}Rb atoms in strong magnetic fields up to the Paschen - Back regime, JETP lett. 96, 303 (2012).

[90] G. Hakhumyan, A. Sargsyan, C. Leroy, Y. Pashayan-Leroy, D. Sarkisyan "Study of Rb atomic transitions $D_{1,2}$ lines in strong magnetic field based on fluorescence spectra of sub - micron thin cell" International Conference on Laser Physics 2010, 79980V-79980V-8 (2010).

[91] A. Sargsyan, G. Hakhumyan, R. Mirzoyan, D. Sarkisyan "Investigation of atomic transitions of cesium in strong magnetic fields by an optical half - wavelength cell" JETP lett., 98, 441 (2013).

[92] A. Sargsyan, G. Hakhumyan, C. Leroy, Y. Pashayan-Leroy, A. Papoyan, D. Sarkisyan, M. Auzinsh "Hyperfine PaschenBack regime in alkali metal atoms: consistency of two theoretical considerations and experiment" JOSA B, 31, 1046 (2014).

[93] A. Sargsyan, G. Hakhumyan, A. Papoyan, D. Sarkisyan "Alkali metal atoms in strong magnetic fields: "Guiding" atomic transitions foretell the characteristics of all transitions of the D_1 line" JETP Lett., 101, 303 (2015).

[94] A. Sargsyan, B. Glushko, D. Sarkisyan "Micron - thick spectroscopic cells for studying the Paschen - Back regime on the hyperfine structure of cesium atoms" JETP 120, 579 (2015).

[95] A. Sargsyan, A. Tonoyan, G. Hakhumyan, C. Leroy,Y. Pashayan-Leroy and D. Sarkisyan "Complete hyperfine Paschen - Back regime at relatively small magnetic fields realized in potassium nano - cell" Europhys. Lett., 110, 23001 (2015).

[96] T.W. Hansch, I.S. Shahin, A.L. Schawlow "High - Resolution Saturation Spectroscopy of the Sodium D lines with a Pulsed tunable Dye Laser" Phys. Rev. Lett., 27, 707 (1971).

[97] C.Wieman and T.Hansch "Doppler - Free Laser Polarization spectroscopy" Phys. Rev. Lett., 36, 1170 (1976).

[98] M. Ducloy, J. R. R. Leite, and M. S. Feld "Laser saturation spectroscopy in the time-delayed mode. Theory of optical free induction decay in coupled Doppler - broadened systems" Phys. Rev. A, 17, 623 (1978).

[99] M. Pinard, C.G. Aminoff, F. Laloe "Velocity - selective optical pumping and Doppler - free spectroscopy" Phys. Rev. A, 19, 2366 (1979).

[100] S. Le Boiteux, P. Simoneau, D. Bloch, M. Ducloy "Doppler - free spectroscopy at a glass - vapour interface by saturated selective reflection at near normal incidence" J. Phys. B: At. Mol. Phys., 20, L149 (1987).

[101] R. Grimm, J. Mlynek "The effect of resonant light pressure in saturation spectroscopy" Appl. Phys. B, 49, 179 (1989)

[102] O. Schmidt, K.-M. Knaak, R. Wynands, D. Meschede "Cesium saturation spectroscopy revisited: How to reverse peak and observe narrow resonances" Appl. Phys. B, 59, 167 (1994)

[103] A. M. Akulshin, A. A. Celikov, V. L. Velichansky "Nonlinear Doppler - free spectroscopy of the $6^1S_0 - 6^3P_1$ intercombination transition in barium" Opt. Comm. 93, 54 (1992).

[104] J. Bowie, J. Boyce, R. Chiao "Saturated-absorption spectroscopy of weak - field Zeeman splittings in rubidium" JOSA B, 12, 1839 (1995).

[105] K. L. Corwin, Z. T. Lu, C. F. Hand, R. J. Epstein, and C. E. Wieman "Frequency - stabilized diode laser with the Zeeman shift in an atomic vapor" Appl. Opt., 37, 3295 (1998).

[106] D. Smith , I. Hughes "The role of hyperfine pumping in multilevel systems exhibiting saturation absorption" Am. J.of Phys., 72, 631, (2004).

[107] A. Banerjee , V. Natarajan "Saturated - absorption spectroscopy: eliminating crossover resonances by use of copropagating beams" Opt. Lett. 28, 1912 (2003)

[108] R. Drampyan, A. Greentree, A. Durrant "Two field nonlinear Faraday rotation in rubidium vapor in a Doppler - free geometry" Opt. Comm., 276, 251 (2007).

[109] S. A. Knappe, H. G. Robinson, L. Hollberg "Microfabricated saturated absorption laser spectrometer" Opt. Express., 15, 6293 (2007).

[110] G. Moon, H.-R. Noh "Analytic solutions for the saturated absorption spectra" JOSA B, 25, 701 (2008).

[111] C. Cohen-Tannoudji and A. Kastler "Optical pumping" Prog. Opt., 5, 1 (1966).

[112] W. Happer "Optical Pumping" Rev. Mod. Phys., 44, 169 (1972).

[113] W. Demtroder "Laser Spectroscopy: Basic Concepts and Instrumentation" (Springer-Verlag, Berlin, 2004).

[114] B. A. Olsen, B. Patton, Y.-Y. Jau, W. Happer "Optical pumping and spectroscopy of Cs vapor at high magnetic field" Phys. Rev. A, 84, 063410 (2011).

[115] T. Vartanyan, D. Lin "Enhanced selective reflection from a thin layer of a dilute gaseous medium" Phys. Rev. A, 51, 1959 (1995).

[116] G. Nienhuis, F.Schuller, M.Ducloy "Nonlinear selective reflection from an atomic vapor at arbitrary incidence angle" Phys. Rev. A, 38, 5197 (1998).

[117] V.Vuletic, V. Sautenkov, C. Zimmermann, T. Hansch "Measurement of cesium resonance line self - broadening and shift with doppler - free selective reflection spectroscopy" Opt. Comm., 99, 185 (1993).

[118] V. A. Sautenkov, H. van Kampen, E. R. Eliel, J. P. Woerdman "Dipole - dipole broadened line shape in a partially excited dense atomic gas" Phys. Rev. Lett., 77, 3327 (1996).

[119] S. Le Boiteux, P. Simoneau, D. Bloch, M. Ducloy "Doppler-free spectroscopy at a glass - vapour interface by saturated selective reflection at near normal incidence" J. Phys. B: At. Mol. Phys., 20, L149 (1987).

[120] P. Wang, A. Gallagher, J. Cooper "Selective reflection by Rb" Phys. Rev. A, 56, 1598 (1997).

[121] M. Chevrollier, M. Oria, J.G. de Souza, D. Bloch, M. Fichet, M. Ducloy "Selective reflection spectroscopy of a resonant vapor at the interface with a metallic layer" Phys. Rev. E, 63, 046610 (2001).

[122] A. Badalyan, V. Chaltykyan, G. Grigoryan, A. Papoyan, S. Shmavonyan, and M. Movsessian "Selective reflection by atomic vapor: experiments and self-consistent theory" Euro. Phys. J. D, 37, 157 (2006).

[123] H. van Kampen, A.V. Papoyan, V.A. Sautenkov, P.H.A.M. Castermans, E.R. Eliel, J.P. Woerdman "Observation of collisional modification of the Zeeman effect in a high - density atomic vapor" Phys. Rev. A, 56, 310 (1997).

[124] Failache H., Saltiel S., Fichet M., Bloch D., and Ducloy M. "Resonant van der Waals Repulsion between Excited Cs Atoms and Sapphire Surface" Phys. Rev. Lett., 83, 5467 (1999).

[125] A. V. Papoyan, G. G. Grigoryan, S. V. Shmavonyan, D. Sarkisyan, J. Guena, M. Lintz and M. A. Bouchiat "Selective reflection spectroscopy with a highly parallel window: phase tunable homodyne detection of the radiated atomic field" Eur. Phys. J. D., 30, 265 (2004).

[126] M. Momeen, G. Rangarajan, P. Deshmukh "Variations of intensity in Rb D_2 line at weak/intermediate fields" J. Phys. B: At. Mol. Opt. Phys., 40, 3163 (2007).

[127] G. Skolnik, N. Vujicic, T. Ban "Optical pumping of the Zeeman components in the rubidium vapor" Opt. Comm., 282, 1326 (2009)

[128] Joanna A. Zielinska, Federica A. Beduini, Nicolas Godbout and Morgan W. Mitchell "Ultra - Narrow Faraday Rotation Filter at the Rb D_1 Line" Opt. Lett., 37, 524 (2012).

[129] L. Weller, K. Kleinbach, M. Zentile, S. Knappe, I. Hughes, C. Adams "Optical isolator using an atomic vapor in the hyperfine Paschen - Back regime" Opt. Lett., 37, 3405 (2012).

[130] L. Weller, K. Kleinbach, M. Zentile, S. Knappe, C. Adams, I. Hughes "Absolute absorption and dispersion of a rubidium vapour in the hyperfine Paschen - Back regime" Journal of Physics B: Atomic, Mol. and Opt. Phys., 45, 215005 (2012).

[131] M. Zentile, R. Andrews, L. Weller, S. Knappe, C. Adams, I. Hughes "The hyperfine paschenback faraday effect" J. of Phys. B: Atomic, Mol. and Opt. Phys., 47, 075005 (2014).

[132] M. Zentile, J. Keaveney, L. Weller, D. Whiting, C. Adams, I. Hughes "ElecSus: A program to calculate the electric susceptibility of an atomic ensemble" Comp. Phys. Comm., 189, 162 (2015).

[133] M. Zentile, D. Whiting, J. Keaveney, C. Adams, I. Hughes "Atomic Faraday filter with equivalent noise bandwidth less than 1 GHz" Opt. Lett., 40, 2000 (2015).

[134] D. Whiting, E. Bimbard, J. Keaveney, M. Zentile, C. Adams, I. Hughes "Electromagnetically induced absorption in a nondegenerate three - level ladder system" Opt. lett., 40, 4289 (2015).

[135] D. Whiting, J. Keaveney, C. Adams, I. Hughes "Direct measurement of excited - state dipole matrix elements using electromagnetically induced transparency in the hyperfine Paschen - Back regime" Phys. Rev. A, 93, 043854 (2016)

[136] B.W. Shore "The Theory of Coherent Atomic Excitation" (New York: Wiley) (1990)

[137] P. Tremblay, A. Michaud, M. Levesque, S. Thériault, M. Breton, J. Beaubien, and N. Cyr "Absorption profiles of alkali - metal D lines in the presence of a static magnetic field, Phys. Rev. A, 42, 2766 (1990).

[138] E.B. Aleksandrov, M.P. Chaika, G.I. Khvostenko "Interference of Atomic States" Springer-Verlag, New York (1993).

[139] Dong Lai "Matter in strong magnetic fields" Rev. Mod. Phys., 73, 629 (2001).

[140] A. Sargsyan, G. Hakhumyan, C. Leroy, Y. Pashayan-Leroy, A. Papoyan, D. Sarkisyan, M. Auzinsh "Hyperfine Paschen - Back regime in alkali metal atoms: consistency of two theoretical considerations and experiment" JOSA, 31, 1046 (2014).

[141] http://steck.us/alkalidata/rubidium85numbers.pdf

[142] D. A. Steck ^{87}Rb D line data, http://steck.us/alkalidata/ rubidium87numbers.pdf.

[143] W.Chalupszak, A.Wojciechowski, S.Pustelny, and W. Gawlik "Nonlinear Faraday rotation and detection of superposition states in cold atoms" Phys. Rev. A, 82, 023417 (2010).

Title: Study of optical and magneto-optical processes in cesium, rubidium and potassium micro- and nano-metric thin atomic layers.

Abstract: It has been investigated the D_1 line transitions of ^{39}K atoms in external magnetic fields using nanocells for the cases of σ^+ and π polarizations of laser radiation. For the first time it is demonstrated the decoupling of electronic total angular momentum J and nuclear momentum I (complete hyperfine Paschen-Back regime) in external magnetic field. For ^{39}K the decoupling takes place at $B \gg 165$ G. In the case of linear polarization it is shown that for $B > 400$ G the transmission spectrum consists of 2 groups of transitions and each group contains of one so-called "Guiding transition" (GT). The GT indicates the asymptotic value of all transitions probabilities in the group and the frequency shifts derivatives value (frequency slopes) in magnetic field.
For the first time it is demonstrated the absence of cross-over resonances in the spectrum of saturated absorption. For that Rb filled micro-cell has been used with atomic vapor thickness $30 - 40$ μm. The use of micro cell allowed the investigation of individual atomic transitions in strong external magnetic fields ($30 - 6000$ G) using the saturated absorption technique. It is experimentally and theoretically manifested that at certain values of the external magnetic fields ($300 - 2000$ G) the probabilities of the Cs D_2 line $Fg = 3 \rightarrow F_e = 5$ atomic transitions experience huge increase. These probabilities, which are forbidden at zero magnetic field, exceed the probabilities of allowed atomic transitions.
Key words: Rb micro and nano-metric cell; K and Cs nano-cell; Zeeman effect; Hyperfine Paschen-Back regime; VSOP resonances; high resolution spectroscopy; "guiding transition"; "initially forbidden further allowed transition"; saturated absorption spectroscopy; σ^+, π and σ^- polarizations of the laser radiation.

Titre: Etude des processus optiques et magnéto-optiques dans des couches atomiques d'épaisseur micro- et nano-métrique de césium, rubidium et de potassium.

Résumé: Les transitions D_1 d'atomes ^{39}K confinées en nano-cellule, soumis à des champs magnétiques externes ont été étudiées dans les cas de polarisation σ^+ et π de la radiation laser. Il est montré, pour la première fois, le découplage du moment angulaire total J et du moment nucléaire I (régime Paschen-Back hyperfin complet) sous champ magnétique externe. Le découplage se produit pour un champ $B \gg 165$ G. Dans le cas d'une polarisation linéaire du laser, nous montrons que pour $B > 400$ G, le spectre de transmission consiste en 2 groupes de transitions et chaque groupe contient une transition appelée transition guide (GT). La GT indique la valeur asymptotique des probabilités des transitions dans un groupe et la valeur des dérivées des décalages en fréquence (pentes de fréquence) dans un champ magnétique. Pour la première fois, il est montré l'absence de résonances cross-over dans le spectre d'absorption saturée. Nous avons utilisé des micro cellules remplies de rubidium. L'épaisseur de la colonne de vapeur atomique était de $30 - 40$ μm. L'utilisation d'une micro cellule a permis l'investigation des transitions atomiques individuelles dans des champs magnétiques intenses ($30 - 6000$ G) en utilisant la technique d'absorption saturée. Nous avons aussi déterminé expérimentalement et théoriquement que pour certaines valeurs du champ magnétique externe ($300 - 2000$ G), on observait un très grand accroissement des probabilités des transitions atomiques $Fg = 3 \rightarrow F_e = 5$ de la raie D_2 du Cs. Sous champ magnétique, les probabilités de ces transitions (qui sont interdites en l'absence de champ magnétique) augmentent brutalement et excédent les probabilités des transitions atomiques permises.
Mots clefs: micro et nano-cellule de rubidium; effet Zeeman; régime Paschen-Back hyperfin; résonances VSOP; spectroscopie à haute résolution; "transition guide"; "transition initialement interdite puis permise"; spectroscopie d'absorption saturée; polarisation σ^+, π et σ^- de la radiation laser.